NATIONAL AERONAUTICS AND SPACE ADMINISTRATION

Technical Report 32-1499

Tracking System Analytic Calibration Activities for the Mariner Mars 1969 Mission

B. D. Mulhall, C. C. Chao, N. A. Mottinger, P. M. Muller, V. J. Ondrasik, W. L. Sjogren, K. L. Thuleen, and D. W. Trask

JET PROPULSION LABORATORY
CALIFORNIA INSTITUTE OF TECHNOLOGY
PASADENA, CALIFORNIA

November 15, 1970

NATIONAL AERONAUTICS AND SPACE ADMINISTRATION

Technical Report 32-1499

Tracking System Analytic Calibration Activities for the Mariner Mars 1969 Mission

B. D. Mulhall, C. C. Chao, N. A. Mottinger, P. M. Muller,
V. J. Ondrasik, W. L. Sjogren, K. L. Thuleen,
and D. W. Trask

JET PROPULSION LABORATORY
CALIFORNIA INSTITUTE OF TECHNOLOGY
PASADENA, CALIFORNIA

November 15, 1970

Prepared Under Contract No. NAS 7-100
National Aeronautics and Space Administration

Preface

The work described in this report was performed by the Mission Analysis Division of the Jet Propulsion Laboratory.

Acknowledgment

The authors wish to express their thanks to Prof. Hibberd of The University of New England, Armidale, New South Wales, Australia; the staffs of the ionospheric observatories of Mount Stromlo and Woomera, Australia; Rev. E. Galdon, and his staff, Observatorio de Ebro, Tortosa, Spain; and R. M. Vice, and his staff, National Institute for Telecommunications Research, Johannesburg, South Africa, for recording and reducing ionospheric measurements; and to G. Levy, C. Stelzried, B. Seidel, and B. Parham of JPL and E. Jackson and his staff at DSS 13 for their support in obtaining Faraday rotation measurements.

Contents

Abstract

This report describes the functions of the Tracking System Analytical Calibration activity of the Deep Space Network in support of an entire mission and, in particular, the Mars encounter phase of the *Mariner* Mars 1969 mission. The support functions encompass calibration of tracking data by estimating physical parameters whose uncertainties represent limitations to navigational accuracy; validation of the calibration data and utilization of these data during a mission; and detailed postflight analysis of tracking data to uncover and resolve any anomalies. Separate articles treat tracking system improvements presently under consideration and error source reductions that may be realizable for future missions; solutions for Deep Space Stations locations; timing errors and polar motion; methods of correcting the tracking data for charged-particle effects (ionospheric corrections); and a model of tropospheric refraction.

Tracking System Analytic Calibration Description

D. W. Trask and B. D. Mulhall

I. Introduction

The Tracking System Analytical Calibration (TSAC) activity is a function of the Deep Space Network (DSN), the global tracking network established by the NASA Office of Tracking and Data Acquisition for two-way communications with unmanned spacecraft traveling from earth to interplanetary distances. The DSN, which operates under the system management and technical direction of the Jet Propulsion Laboratory (JPL), comprises three main elements: the Deep Space Instrumentation Facility (DSIF), the Ground Communications Facility (GCF), and the Space Flight Operations Facility (SFOF). The tracking and data acquisition stations of the DSIF, identified as Deep Space Stations (DSS), are situated so that three stations may be selected approximately 120 deg apart in longitude to provide continuous coverage of distant spacecraft. The DSS serial designations and locations are listed in Table 1.

Ground communications among the elements of the DSN are provided by GCF links consisting of voice, teletype, and high-speed-data circuits.

The SFOF is the control center for DSN operations during the flight of a deep space probe. SFOF functions include controlling the spacecraft by generating and transmitting commands, computing trajectories, determining the spacecraft orbit during the flight from range and doppler data obtained from the tracking and data acquisition stations, and processing the spacecraft telemetry data and data from space science experiments.

The TSAC functions include the calibration of tracking data by estimating physical parameters whose uncertainties represent limitations to navigational accuracy; validation of the calibration data and utilization of these data during a mission; and detailed postflight analysis

Table 1. Deep Space Station locations

Deep Space Communications Complex (DSCC)	Location	Deep Space Station (DSS)	Serial designation
Goldstone	California	Pioneer	DSS 11
		Echo	DSS 12
		Venus	DSS 13
		Mars	DSS 14
Canberra	Australia	Woomera	DSS 41
		Tidbinbilla	DSS 42
—	South Africa	Johannesburg	DSS 51
Madrid	Spain	Robledo	DSS 61
		Cebreros	DSS 62

of tracking data to uncover and resolve any anomalies that may exist.

This report describes the TSAC activities in support of the entire mission and in particular the Mars encounter phase of the *Mariner* Mars 1969 mission. This article summarizes the TSAC efforts and discusses tracking system improvements presently under consideration and error source reductions that may be realizable for future missions. Subsequent articles discuss in more detail the DSS locations solutions, timing errors and polar motion, methods of correcting the tracking data for charged-particle effects (ionospheric corrections), and the tropospheric refraction model.

II. The DSN as a Navigation Instrument

The determination of a deep space probe orbit and the consequent navigation of the probe depend primarily on the use of doppler data obtained from transmitting a radio signal to the spacecraft which is transponded by the spacecraft and returned to the tracking station. This permits the direct measurement of doppler, which represents the velocity of the probe with respect to the tracking station.

J. Light (Ref. 1) shows that for a relatively short span of tracking data, the ability to determine the velocity of a spacecraft after the burning of its orbit trim motor is unaffected by the position parallax or by gravity bending of the orbit. Light named the remaining effect the "velocity parallax."

Hamilton and Melbourne (Ref. 2) showed that the information contained in a single pass of doppler data, the velocity parallax, can be characterized by

$$\dot{\rho} = \dot{r} + \omega r_{s\oplus} \cos \delta \sin (\omega t_{\oplus} - \Delta\theta), \tag{1}$$

where

$\dot{\rho}$ = tracking station spacecraft range rate,

$\dot{r}$ = geocentric spacecraft range rate,

ω = mean rotation rate of the earth of date,

r_s = spin radius of the tracking station,

δ = instantaneous declination of the spacecraft,

t = time past meridian transit,

and

$$\omega t = \omega t_u^* + \alpha_{\odot} + \lambda^* - \alpha^*,$$

where

t_u^* = UT1,[1]

$\alpha_{\odot}$ = instantaneous right ascension of the mean sun,

λ^* = *a priori* value of station longitude,

α^* = *a priori* value of right ascension of the spacecraft,

and

$$\Delta\theta = \epsilon_a - \epsilon_\lambda - \omega\xi,$$

where

$\epsilon_a = \alpha - \alpha^*$, the error in the *a priori* value of spacecraft right ascension,

$\epsilon_\lambda = \lambda - \lambda^*$, the error in the *a priori* value of station longitude,

$\omega_{\oplus}\xi = t_u - t_u^*$, the error in UT1.

Figure 1 shows how this expression arises. The geocentric range rate appears as a slowly varying function on which a sinusoidal-like pattern is superimposed due

[1]Universal Time 1. See explanation of the three types of time used in computing an orbit in the article by P. M. Muller and C. C. Chao, "Timing Errors and Polar Motion."

to the rotation of the station about the earth axis. The amplitude b of the quasi-sinusoid is composed of

$$b = r_s\omega_\oplus \cos \delta.$$

For a constant spacecraft right ascension, the errors in timing, in spacecraft right ascension, and in station longitude appear as a change in phase, $\Delta\theta$, of the quasi-sinusoid.

The station–spacecraft range rate $\dot{\rho}$ can be written

$$\dot{\rho} = a + b \sin \omega_\oplus t + c \cos \omega_\oplus t, \qquad (2)$$

where

$$a = \dot{r},$$

$$b = r_s\omega_\oplus \cos \delta \cos \Delta\theta \sim r_s\omega_\oplus \cos \delta,$$

$$c = r_s\omega_\oplus \cos \delta \sin \Delta\theta \sim r_s\omega_\oplus \cos \delta\Delta\theta,$$

since $\Delta\theta$ is small.

By solving for the parameters a, b, and c, the spin radius of the station can be determined from b. If the errors in UT1 and the spacecraft right ascension can be determined, then the station longitude error can also be determined from c:

$$r_s = \frac{b}{\omega \cos \delta},$$

$$\Delta\theta = \frac{c}{r_s\omega \cos \delta},$$

$$\epsilon\lambda = -\Delta\theta + \epsilon_a - \omega_\oplus\xi.$$

Notice that b represents the amplitude of $\dot{\rho}$, while c is related to the time of meridian transit; that is, c is proportional to the difference between the actual and the nominal time of meridian passage. The doppler tracking data are primarily sensitive to the r_s and λ coordinates of the DSS. Changes in the station location parallel to the earth's spin axis have little effect on the doppler data.

Equation (2), which is the Hamilton–Melbourne parameterization derived in Ref. 2, is an extremely useful tool in predicting the effect of certain error sources on navigation accuracy. For example, during the cruise and encounter support phases of a planetary mission, in which the model tends to match the real world, the navigation accuracy is particularly sensitive to errors that have a diurnal period. In particular, those error sources that impose a signature of a sine wave centered about meridian transit on the doppler[2] affect the estimate of the declination of the spacecraft, while those that put a cosine wave on the doppler change the phase and affect the estimate of the right ascension.

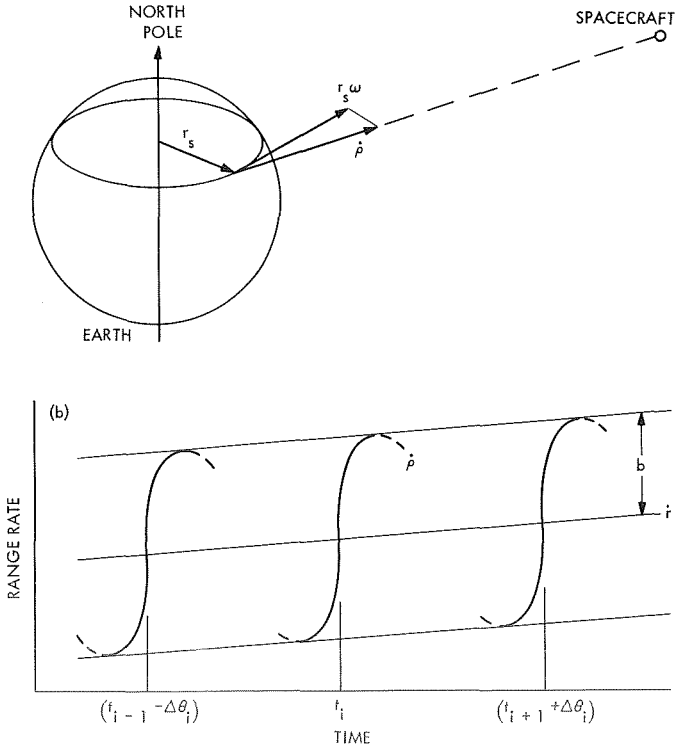

Fig. 1. Information content of doppler data: (a) earth–spacecraft geometry; (b) doppler signature

III. Navigation Error Sources

The maintenance of a balanced system of error sources is the major guideline for TSAC in the formulation of an error budget. The system is balanced such that a given expenditure of resources is budgeted to minimize the root sum squared (rss) of the resultant navigational errors. In general, this necessitates advancing the state of the art for the most critical error sources and, within the above constraints, reducing the effects of other error sources to a negligible level when compared to the most critical error source.

[2]We are actually concerned with the effect on the doppler residual; that is, the doppler observable minus the computed value of what the doppler observable should have been, based on the best estimate of the parameters that affect this computation.

For a mission such as *Mariner* Mars 1969, the tightest bounds on the allowable errors arise from the navigational accuracy requirements during the encounter phase. Primarily, this phase of the mission required a precise knowledge of the probe's trajectory with respect to Mars so that the scientific instruments could be accurately pointed. Such a determination can be derived from the radio tracking data if the spacecraft trajectory has been sufficiently influenced by the gravitational field of the target planet. However, for *Mariner* Mars 1969, operational considerations precluded waiting until this late in the encounter phase. Consequently, the Mars–spacecraft position was inferred from a knowledge of the Mars–earth position (planetary ephemerides) and the spacecraft–earth position (the estimates of the probe's right ascension and declination from the radio tracking data).

The useful length of tracking data spans was also affected by two limitations that could not be modeled: (1) not being able to take advantage of the gravitational attraction of Mars and (2) the restriction to a relatively short data arc. The effects of these limitations are discussed later in this report[3] and are also considered in Ref. 3.

The principal error sources that corrupt radio doppler data are listed in Table 2. These error sources can be grouped into four categories. The first group has been called platform error sources. These include uncertainty in time and the location of the earth's pole[4] and the uncertainty of the tracking station's location with respect to the earth's rotational axis.[3]

A second group of error sources is categorized as the transmission media, the media through which the radio signal passes. These media include the charged particles in the earth's ionosphere, in the solar wind, and in the ionospheres of other planets.[5] The neutral medium of the lower atmosphere—the troposphere—also is an error source in this category.[6]

A third group of error sources, which is not discussed in this report, concerns those related to spacecraft and ground equipment. Included in this category are variations of the effective path through the microwave equipment in the spacecraft and at the tracking station, and drift in the frequency system that controls the frequency of the S-band signal.

[3]See "Station Locations," by N. A. Mottinger and W. L. Sjogren.

[4]See "Timing Errors and Polar Motion," by P. M. Muller and C. C. Chao.

[5]See "The Ionosphere," by B. D. Mulhall, V. J. Ondrasik, and K. L. Thuleen.

[6]See "The Troposphere," by V. J. Ondrasik.

Table 2. Error sources that limit doppler navigation accuracy

Tracking data error sources	Critical region for the error source	Area of improvement		Possible action/improvement	References[c]
		Hardware[a]	Software[b]		
Oscillator instability	Effect of medium-term instability [~24-h period] in α, δ is proportional to the DSS–probe distance, ρ	√		Cesium standards or better, plus appropriate cleanup loops to replace rubidium standards	Trask and Hamilton, 37-38, pp. 8–13; Curkendall, 37-41, pp. 42–47, and 37-46, pp. 4–8; Motsch and Curkendall, 37-43, pp. 37–39
Phase jitter		√		Constant design improvements improve SNR[d]	Motsch and Curkendall, 37-43, pp. 37–39
Electrical path-length variation through:					
DSS	Primarily proportional to temperature variation on external cabling between control room and antenna	√	√	Strict temperature control at equipment and active cable delay compensation	
Spacecraft	Important for target orbiter subjected to temperature fluctuations (i.e., passes through shadow)	√	√	Improved spacecraft transponder delay and preflight calibration, or active compensation	

Table 2 (contd)

Tracking data error sources	Critical region for the error source	Area of improvement		Possible action/improvement	References[c]
		Hardware[a]	Software[b]		
Antenna motion:					
DSS		√	√	Basic design (structure, painting for temperature compensation) and software model of motion during a tracking pass	Motsch, 37-39, pp. 16–18
Spacecraft		√	√	Placement with respect to spacecraft CG, and control of limit cycle motion; utilize telemetry information of motion (or reject data)	
Timing:					
DSS sync to common time standard	Generally critical in support of target orbiters	√		Utilize: 1. X-band lunar bounce 2. Traveling clocks 3. Three-way ranging 4. Local "standards lab" 5. "Loran C"-type implementation	Trask and Muller, 37-39, pp. 7–16
A.1—UT1	Affects only right ascension		√	1. Improve data reduction technique (for post as well as future PZT observations) 2. New method for determining A.1—UT1, such as use of interferometric tracking of distant radio sources	Muller, 37-41, pp. 18–24
Precession, nutation (spin axis with respect to inertial space)			√	Further reduction of available data and use of interferometric tracking of distant radio sources	
Pole motion (earth's crust with respect to spin axis)			√	1. Improve predictions a. "Hattori" model b. Sequential estimation technique 2. Reduce time interval over which predictions must be extrapolated (reduce lag between observations and availability of results) 3. New method for determining polar motion, such as use of interferometric tracking of distant radio sources	Muller, 37-45, pp. 10–14; Chao and Muller, 37-56, pp. 69–74

Table 2 (contd)

Tracking data error sources	Critical region for the error source	Area of improvement		Possible action/improvement	References[c]
		Hardware[a]	Software[b]		
Charged particles:					
Ionosphere	Worst effect at sun–earth probe angle SEP = 90°		√	Utilize ionosonde data, Faraday rotation data from spacecraft or earth satellites, dual frequency, group vs phase velocity technique (DRVID), empirical model, etc.	Trask and Efron, 37-41, pp. 3–12; Liu, 37-41, pp. 38–41; Winn, 37-53, pp. 20–25; Webb and Mulhall, 37-55, pp. 13–15; Mulhall and Thuleen, 37-55, pp. 15–19; Mulhall and Wimberly, 37-55, pp. 19–23; Mulhall and Wimberly, 37-56, pp. 58–61; Ondrasik and Mulhall, 37-57, pp. 29–42; Mulhall, 37-57, pp. 24–29; Mulhall, 37-58, pp. 66–73; Ondrasik, 37-59, pp. 97–110; Ondrasik, Mulhall, and Mottinger, 37-60, pp. 89–95; Madrid, 37-60, pp. 95–97.
Space plasma	Worst at SEP = 0 and effect increases with ρ. Little increase above ρ = 5 AU and most of the effect by ρ = 3 AU		√	Dual frequency and DRVID techniques	Mulhall and Wimberly, 37-56, pp. 58–61; Efron and Lisowski, 37-56, pp. 61–69; Anderson, 37-58, pp. 77–81; Ondrasik, Mulhall, and Mottinger, 37-60, pp. 89–95
Tropospheric refraction	Worst at low elevation angles γ, but deletion of data at low γ degrades ability to determine α, δ		√	Model based on: 1. Average local conditions at DSS 2. Local atmospheric measurements near DSS	Liu, 37-50, pp. 93–97; Mottinger, 37-50, pp. 97–104; Winn, 37-51, pp. 42–50.
Software			√	Replace SPODP[e] with DPODP[f], incorporating above model improvements	Moyer, issues 37-38, -39, and -41 through -46; Warner, 37-47, pp. 35–41
DSS locations			√	Statistically combine results of several missions, utilizing above improvements	Vegos and Trask, 37-43, pp. 18–24; Mottinger and Trask, 37-48, pp. 12–22; Mottinger, 37-49, pp. 10–23, and 37-56, pp. 45–58.

[a]Data user realizes benefit automatically.

[b]Data user "responsible" for incorporating improvement.

[c]References given here list the authors, issue numbers, and page numbers of articles that appeared in the Tracking and Navigation Accuracy Analysis Section of *The Deep Space Network*, a periodical publication of the JPL Space Programs Summary series.

[d]Signal-to-noise ratio.

[e]Single Precision Orbit Determination Program

[f]Double Precision Orbit Determination Program

A fourth category consists of errors in the ephemerides of the earth, moon, and target planet.

Notice that the errors in the foregoing categories are concerned with obtaining the proper angular position in right ascension (α) and declination (δ) of the spacecraft in inertial space, which was an important consideration in support of the *Mariner* Mars 1969 encounter phase. The error sources[7] that affect navigational accuracy during this and other phases of the mission are listed in Table 2, which also calls out the conditions under which each error source is most critical, whether future areas of improvement are likely within the hardware or software, and possible action to effect an improvement.

A comparison is made in Table 3 of the effect of the limitations to navigation accuracy on the DSN doppler system as it existed in July 1967 and the system that supported the *Mariner* Mars 1969 encounter in July 1969. The changes that took place over this two-year span are also summarized. The relative limitations to navigation capability caused by errors that the TSAC activity attempts to control are illustrated in the circular variance diagrams presented in Figs. 2 and 3. These diagrams are scaled so that the area of the circle allocated to each error source is proportional to the variance contribution of that error source. In the *Mariner* Mars 1969 system, the DSS locations are the primary limitations, along with polar motion in the declination direction and UT1 in the right ascension direction.

The primary improvement of the 1969 over the 1967 system occurred in the area of DSS locations. The DSS location solutions are obtained from post-flight analysis of tracking data. The velocity parallax effect (which is the dominant source of information in the doppler tracking data for a distant spacecraft not significantly accelerated by gravitational forces) does not separate the probe position and the DSS locations. That is, the velocity parallax effect directly determines the parameter b, which is a combination of r_s and δ, and also determines the parameter c, which is a combination of α and λ, as represented by Eq. (1).[8]

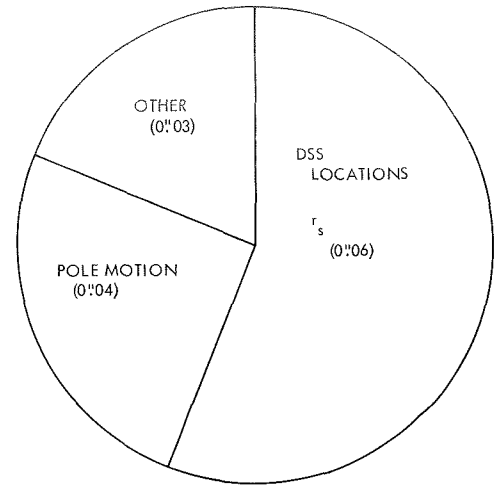

TOTAL tan δ σ_δ = 0".08
1 m = 0".04 CONVERSION USED FOR LOCATION OF TYPICAL DSS

Fig. 2. Variance circle of errors in declination direction: *Mariner* Mars 1969 encounter support

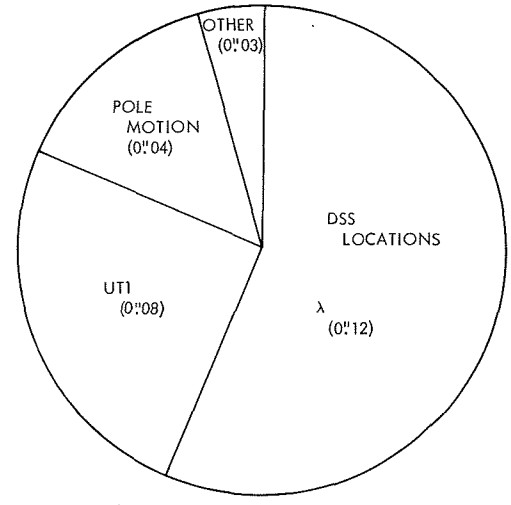

TOTAL σ_α = 0".16
1 m = 0".04 CONVERSION USED FOR LOCATION OF TYPICAL DSS

Fig. 3. Variance circle of errors in right ascension direction: *Mariner* Mars 1969 encounter support

However, the r_s (but not the λ) component can be determined if a short span of tracking data is processed that includes a period when the probe declination passes through zero. Since $b = \omega_\oplus r_s \cos \delta$, relatively large errors in the declination of the probe can be tolerated without significantly degrading the r_s solution when δ approaches 0.

Both r_s and λ can be determined when the probe position can be independently inferred from other effects

[7]Articles on these error sources are regularly published in the Tracking and Navigation Accuracy Analysis Section of *The Deep Space Network*, a periodical publication of the JPL Space Programs Summary series. References to SPS articles are listed in Table 2.

[8]The b and c determinations are also corrupted by error sources such as uncertainties in polar motion, UT1, and the effects of the transmission media.

Table 3. DSN doppler navigation system: equivalent DSS location errors (for Mars encounter support)

System as of July 1967 (assumes *Mariner* Mars 1969 conditions)			Goals for *Mariner* Mars 1969: ρ = 2/3 AU; $\delta = -24.5°$		
Basic system[a]	Equivalent location error, m		Changes over basic system[a]	Equivalent location error, m	
	σ_{r_s}	σ_λ		σ_{r_s}	σ_λ
DSS locations	8	12	Statistical combination of results from *Mariner IV, V,* plus improvements listed below	1.5	3
Pole motion	2	2	Switched from IPMS[b] to BIH[c] and improved the prediction techniques	1	1
Timing (A.1–UT1)	—	3	Constrained least squares polynomial fit to 1955 through present data span	—	2
Tropospheric refraction	3	1	Used average local conditions at each DSS	0.5	0.2
Charged particles:					
Ionosphere	5	5	Used ionosonde and Faraday rotation data	0.5	1
Space plasma	4	4	No actual calibration performed; DRVID employed where available	—	—
Ground antenna motion (variation over 12-h pass)	0.3	0.3	DPODP models' effect for "rigid" antenna	0.02	0.02
Electrical path-length variation through the DSS (over 12-h pass)	1	1	Same	1	1
Long-term (~12 h) oscillator instability	0.5	0.5	Same	0.5	0.5
High-frequency "visible" doppler noise:					
Oscillator frequency jitter	0.2	0.4	Same	0.2	0.4
Phase jitter	0.02	0.05	Same	0.02	0.05
			Mariner Mars 1969:		
			Committed	3	5
			Goals	1	2

[a]Does not include limitations controlled by the project; i.e., software (orbit determination program), ephemeris, nongravitations forces (gas leakage, etc.).

[b]International Polar Motion Service

[c]Bureau International de l'Heure

such as the gravitational bending of the orbit, provided that the position of the target planet with respect to earth is well known. This situation arises during the period of closest approach of the spacecraft to the target body.[9] The position of the target planet with respect to the earth can be determined from the ephemerides of the earth and the target planet.

[9]Gravity bending due to the sun can also have appreciable effect from relatively long data arcs during the cruise portion of a planetary mission to allow the determination of DSS locations.

It should be emphasized that although special spans of tracking data, as described above, were selected for postflight analysis to determine the DSS locations, the quality of the solutions was limited by precisely the same error sources that limit navigation accuracy during the cruise and encounter phases of a planetary mission. Consequently, the technological advances made in the 1969 system over the 1967 system were important not only in that they directly improved navigation accuracy capability, but also because they could be applied to past tracking data (data from earlier missions) to improve the DSS location solutions.

IV. Credibility of DSS Location Solutions

The navigation accuracy capability for deep space missions can be limited by the uncertainties in the DSS locations with respect to the crust of the earth. The extent of these limitations in the encounter support of the *Mariner* Mars 1969 mission is illustrated in Figs. 2 and 3, which show proportional sources of error in estimates of declination and right ascension of the spacecraft.

The *Mariner* Mars 1969 goals asked that the 1σ uncertainty in the distance off the spin axis (σ_{r_s}) be held to 1.5 m and the uncertainty in longitude (σ_λ) to 3 m. These represent the primary limitation in the declination and right ascension directions, respectively. Even though these DSS location uncertainties were the leading limitation, they still represent considerable improvement in the state of the art over previous planetary missions. For example, $\sigma_{r_s} = 8$ m and $\sigma_\lambda = 12$ m for the *Mariner* Venus 67 mission. Considerable effort was expended to effect the desired improvement. However, proof that the *Mariner* Mars 1969 goals were actually achieved is at present difficult to establish and must await even more accurate solutions in the future, which can be used as a comparison standard.

The station locations used for *Mariner* Mars 1969 were produced through the detailed postflight analysis of selected portions of the *Mariner IV* and *Mariner V* missions. The primary improvement made in 1969 over 1967 was the incorporation of the corrections to account for the effect of the charged particles in the ionosphere on tracking data. The current best estimates with the ionospheric corrections included are listed in Table 4, along with previous solutions which do not include the ionospheric corrections. The method of obtaining these solutions, which are admittedly limited in number, is described in the next article in this report. The main limitation on the number of solutions was one of resources. In the future, when more ionospheric data has been obtained, the analysis will be extended to include zero-declination cases for the *Pioneer* spacecraft as well as selected lunar missions.

Since no comparison standard for absolute location solutions is currently accepted as superior to the solutions obtained from postflight processing of radio tracking data, the accuracy of the solutions must be inferred from other means. These include:

(1) The repeatability of solutions for a single station.

(2) For DSSs within a few kilometers of each other, comparison of relative locations as obtained from radio tracking data with those obtained from ground survey results.

(3) Comparisons made with solutions derived from independent means.

As an example of (3), Refs. 4 and 5 compare station location solutions obtained by the Smithsonian Astrophysical Observatory (SAO) and the DSN. These comparisons depend on relative DSS–SAO distances as derived from ground survey data, since the two organizations determine only the locations of their own tracking stations. SAO determined the locations of their stations through the use of Baker–Nunn optical and laser tracking data, while the DSN determined the locations of the DSS by the use of radio tracking data. While such comparisons

Table 4. Comparison of ionospheric effects on station location estimates

Deep Space Station	Data from *Mariner* Mars 1969 mission		Data from *Mariner* Venus 67 mission		Differences due to ionosphere (results with ionosphere calibration minus results without ionosphere calibration)	
	Best estimates with ionosphere calibration		Best estimates without ionosphere calibration			
	r_s, km	λ, deg	r_s, km	λ, deg	Δr_s, m	$\Delta\lambda$, 10^{-5} deg
11	5206.3419	243.150627	5206.3381	243.150637	3.8	−0.94
12	5212.0535	243.194559	5212.0497	243.194568	3.8	−0.94
14	5203.9989	243.110513	5203.9951	243.110523	3.8	−0.96
41	5450.1986	136.887507	5450.1984	136.887540	0.26	−3.24
42	5205.3504	148.981301	5205.3501	148.981300	−0.28	−0.32
51	5742.9417	27.685432	5742.9410	27.685441	−0.61	−0.84
61	4862.6078	355.751007	4862.6043	355.751018	3.47	−1.04
62	4860.8176	355.632200	4860.8141	355.632211	3.45	−1.08

may not prove the actual accuracy of either set of solutions, they are a very useful tool with which to uncover blunders if agreement is not as good as predicted from the claimed accuracies of the respective solutions. In fact, these solutions uncovered a large bias, as yet unexplained, between the two sets of longitude solutions, although the quality of both the r_s and $\Delta\lambda$ comparisons is compatible with the claimed accuracies of the SAO and DSN determinations.

V. Establishment of Credibility Through Repeatability of Solutions

One of the chief limitations of this method is the sparsity in the number of solutions for each individual DSS, although this can be overcome to some extent by referencing all DSS within a geodetic datum to one site by the use of relative locations derived from ground survey data. Even though the effect of most error sources is independent for data spans widely separated in time, some error sources may bias the DSS solutions. Fortunately, however, an error source that causes a compensating bias (an error that is consistent for all of the missions considered) in the DSS location will not affect the ability to compute or predict at some future time the trajectory of the spacecraft. An offset in UT1 is an example of an error that could be consistent from mission to mission, while the error incurred in DSS locations by not accounting for the effect of the ionosphere may tend to bias the DSS solutions for the small set considered in preparation for the *Mariner* Mars 1969 mission, but would not in general be consistent from mission to mission.

The DSS location solutions are affected by much the same error sources as affect navigation capability; namely, the platform parameters such as UT1 and pole motion and those error sources that affect the observable, such as the effects of the transmission media.

The case for pole motion is illustrated in Fig. 4. As far as the tracking data are concerned, the pole of the earth is the spin axis. This means that if the crust of the earth slips with respect to the spin axis, for the case shown in Fig. 4, then r_s shortens and the longitude between Greenwich and a DSS in the northern hemisphere increases. In the case of UT1, an error has no effect on r_s, but affects the λ of all the DSS by the same (angular)

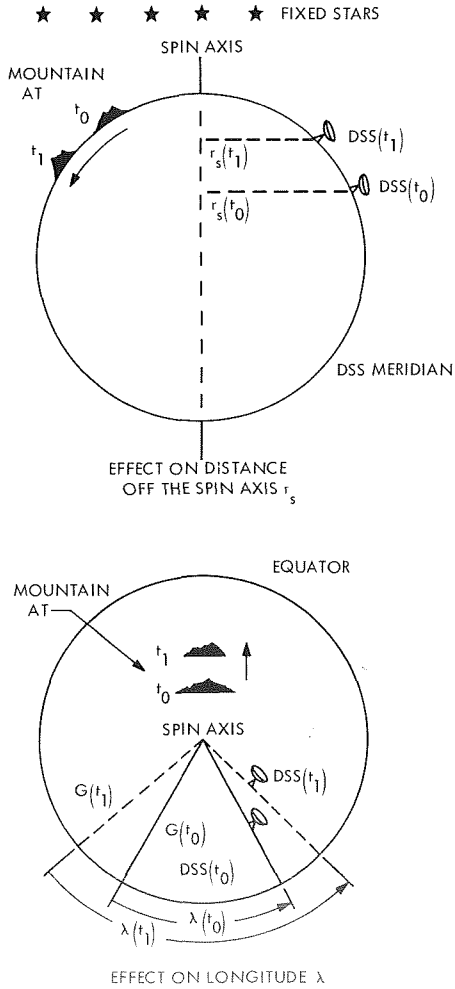

Fig. 4. Polar motion

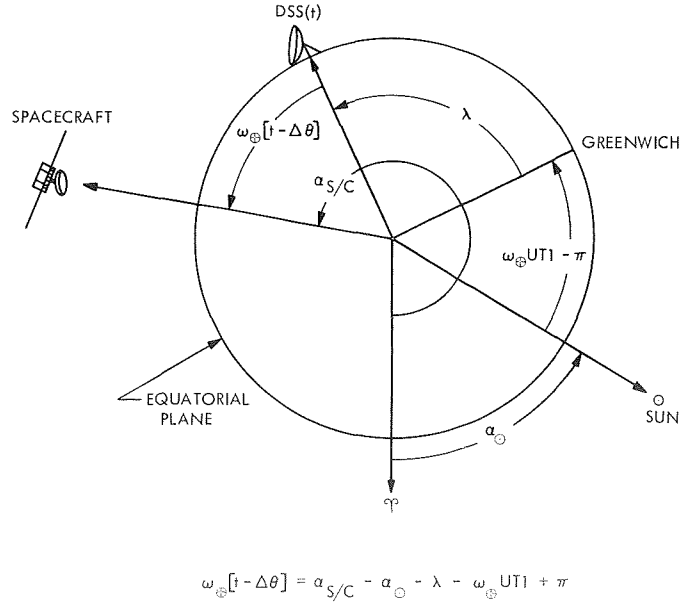

Fig. 5. Correlation of universal time: DSS longitude and solar longitude

amount; that is, Δ UT1 = 1 ms will produce $\Delta\lambda$ = 0.4 m at the typical DSS latitude (35°). This is illustrated in Fig. 5 where the tracking data senses the angle $\omega_\oplus\ (t - t_0)$, where $\omega_\oplus\ (t - t_0) = (\alpha_{S/C} - \lambda - \omega_\oplus$ UT1 $+ \pi - \alpha_\odot)$. Therefore, when determining λ, any error in the other quantities on the right-hand side of the above equation will be reflected as errors in the solution of λ on a one-to-one (angular) basis.[10]

As previously mentioned, the ionosphere, which prior to the 1969 mission preparations was ignored, is an example of an error source that can produce systematic errors in the DSS location solutions. Figures 6 and 7 show the shift in the r_s and λ solutions, respectively, due to applying the ionospheric corrections to the radio tracking data. Notice that for the data spans considered, the r_s is always positive and averages 3½ m for the Goldstone Complex.

The errors in both r_s and λ caused by ignoring the ionosphere are significant. The effect of the ionospheric charged particles on the tracking is proportional to the number of charged particles in a column of unit area that contains the propagation path of the radio signal between the DSS and the spacecraft. This columnar content is a function not only of the ray path, but also of the time of day, as illustrated in Fig. 8. The action of the ultraviolet rays of the sun on the ionosphere disassociates or ionizes the particles of the upper portion of the atmosphere. The maximum concentration of charged particles occurs near the subsolar point, while toward

[10]Again, errors in quantities not considered in the Hamilton–Melbourne model, such as pole motion and the effect of transmission media, will also affect the longitude solution.

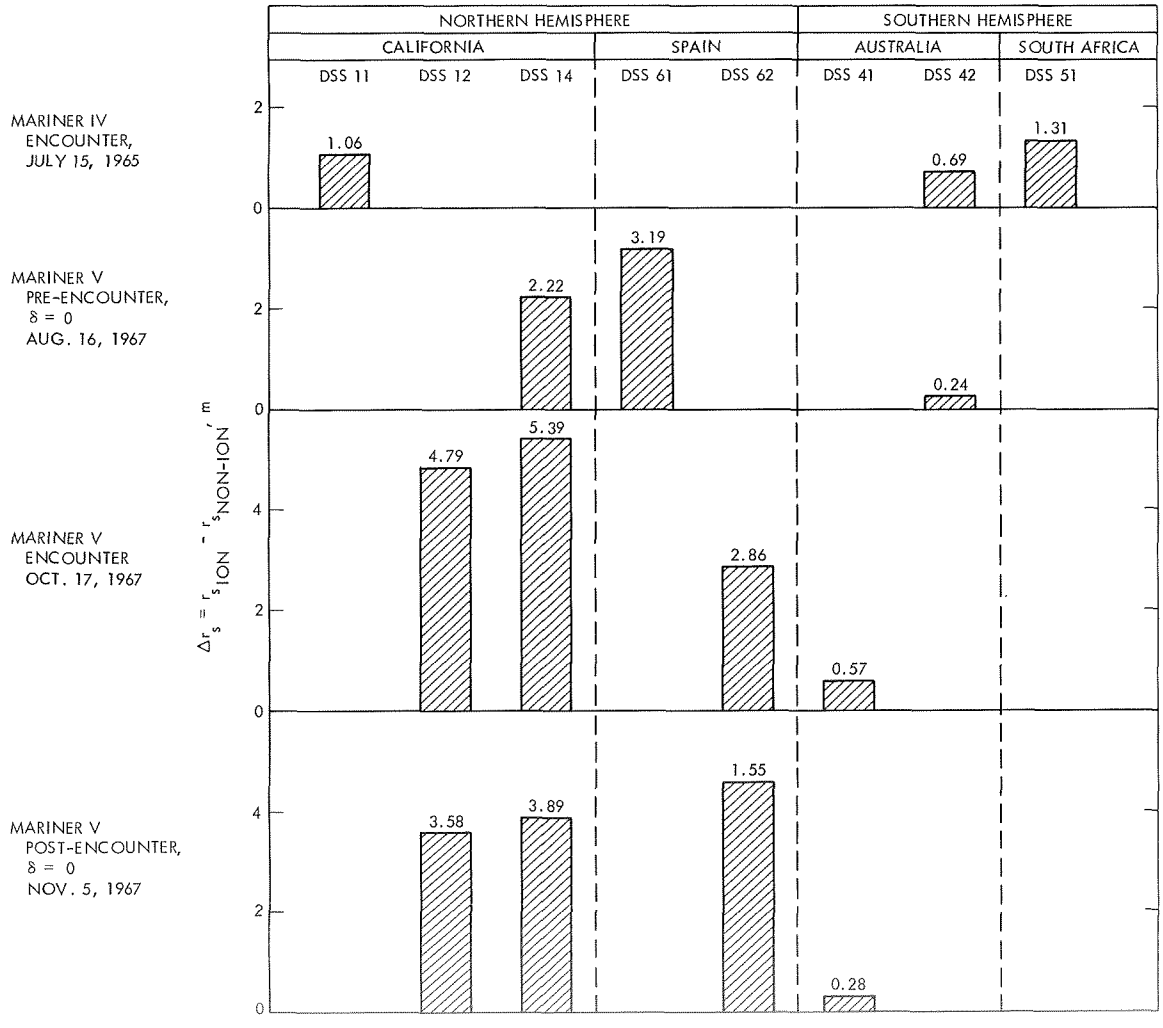

Fig. 6. Effect of ionosphere on spin radius solutions

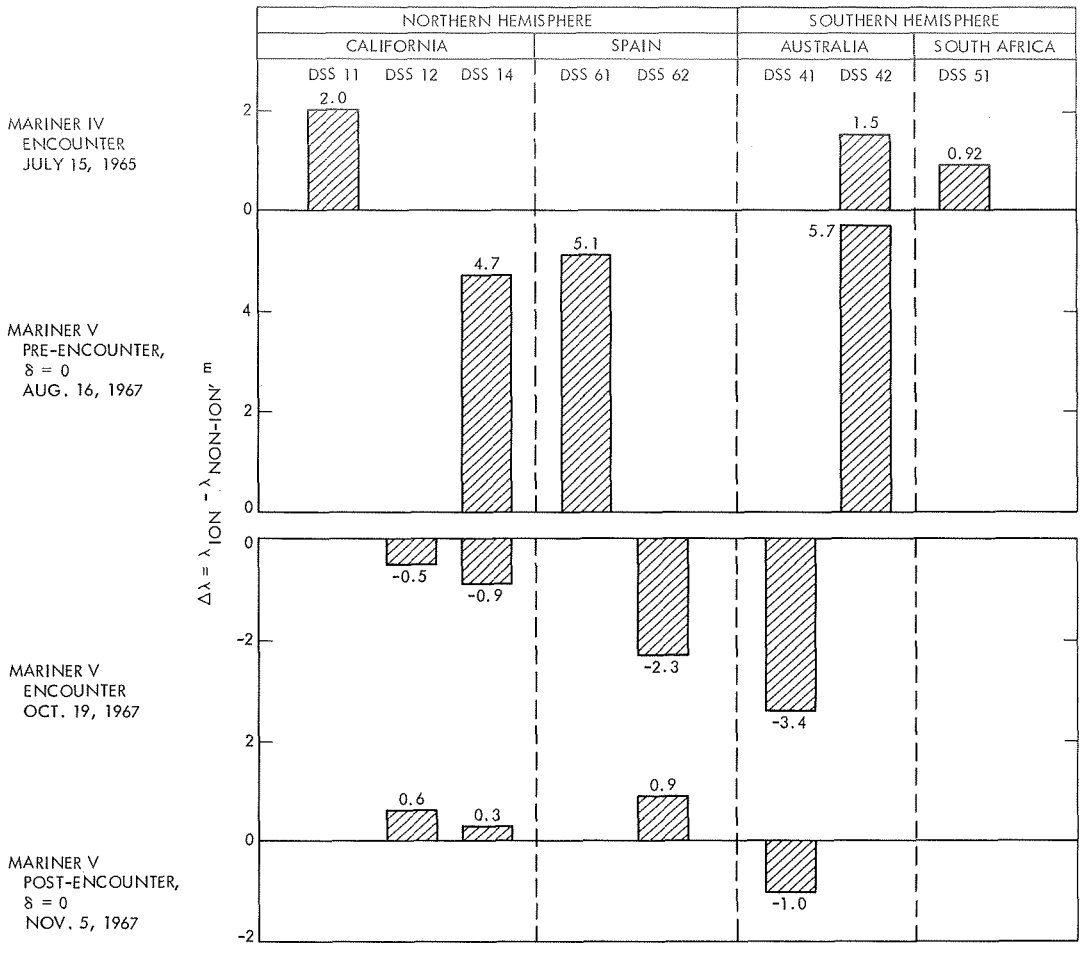

Fig. 7. Effect of ionosphere on longitude solutions

nightfall, recombination dominates and a minimum number of charged particles exist on the nightside of the earth. A number of dashed lines are traced out in Fig. 8, representing the error in counted doppler ($\Delta\rho_I$) caused by the charged particles. Solid lines apply to a geostationary satellite at a constant elevation angle; the lower curve is for a spacecraft directly over the station ($\gamma = 90°$) and the top curve is for a spacecraft on the observer's horizon ($\gamma = 0°$) and is generally a factor of 3 to 3.5 times greater than the $\gamma = 90°$ case. The peaks of these curves usually occur between noon and 3 p.m. local time; that is, sometimes the rate of ionization exceeds the rate of the recombination even after high noon. However, the DSS locations are not derived from tracking geostationary spacecraft, but from planetary probes, in which case the sun–earth probe angle (SEP) and not γ is relatively constant throughout the day. Dashed lines in Fig. 8 represent the time history of $\Delta\rho_I$ for spacecraft at SEP = 0, 90, and 270°. Each trace starts as the spacecraft rises on the horizon ($\gamma = 0°$), continues to the peak elevation angle,[11] and then continues on until the spacecraft sets ($\gamma = 0$) (Ref. 6).

Errors in station location solutions will arise during the postflight processing of the radio tracking data if the effect of the ionosphere, as illustrated in Fig. 8, is ignored. In particular, a $\Delta\rho_I$ signature shaped like a cosine wave, centered at the mid-point of the pass, will cause an error in r_s (ϵ_{r_s}) equal to the amplitude of the cosine wave (and a similar relationship exists between a sine-shaped $\Delta\rho_I$ and an error in λ). This means that for the three cases illustrated in Fig. 8, r_s will be positive for SEP = 90 or 270° and may have either sign (although the error may be small) for SEP = 0°, depending upon the actual maximum elevation angle and the time of day at which the peak ionospheric activity occurs.

[11]The peak elevation angle is a function of the declination of the spacecraft and the latitude of the station, ϕ; i.e., $\gamma_{max} = 90° - |\phi - \delta|$.

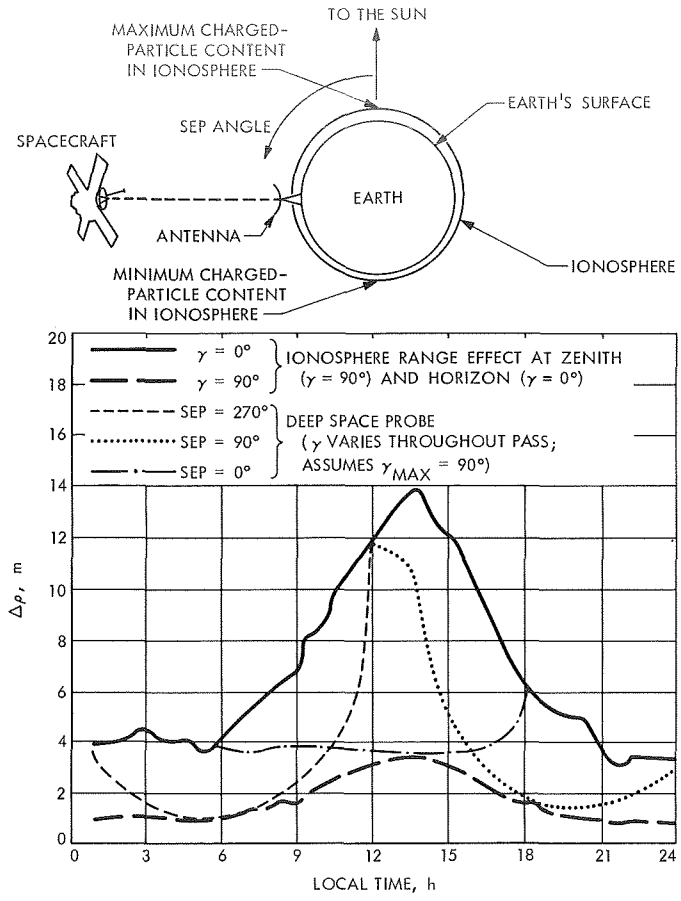

Fig. 8. Effect of ionosphere on radio tracking data

For past probes at planetary encounter, SEP $\sim$ 90 to 120° for Mars missions and SEP $\sim$ 45° for Venus missions. This means that ϵ_{r_s} will be larger for a Mars mission than for Venus missions, although exceptions can occur, because the ionosphere, that is, the charged particle content, does vary as a function of parameters not considered in the above discussion, such as seasonal variation and changes in solar activity.

The net effect is that although it is coincidental (the data set could have included zero-declination *Pioneer* cases at SEP $\sim$ 0°), the ionospheric corrections did bias the r_s solutions for the cases analyzed.

There still may be biases in the DSS solutions due to other error sources, such as the troposphere and the space plasma, although at present the extent of these effects is yet to be defined. In the case of the troposphere the current model, which is described later in this report,[12] is in the process of being revised and probably does contribute systematic errors to the DSS location solutions, if the tracking station's geometry is similar for the data spans analyzed.

The effect of charged particles in the space plasma may account for small systematic errors. Not only does the average number of charged particles in the column generally increase as the earth–spacecraft distance increases, but for the relatively small number of data sets included, the effects of the random fluctuations may not have been adequately averaged out. These random fluctuations are due to concentrations of charged particles spewing out from the sun as demonstrated by the model of charged particles in the space plasma described in Ref. 7. The model includes from 3 to 5 spiral arms that exist at any one time, each rotating with the solar equatorial period of about 28 days. Unfortunately, the measurements of the effect of the space plasma during the periods of interest are rather sparse. The *Mariner* Venus 67 mission yielded the most information. It carried the Stanford dual-frequency experiment, which provided measurements of the columnar electron content in the space plasma during the time the spacecraft was in view of the Stanford, California, tracking station. The error caused by the space plasma during portions of this mission is discussed in Ref. 8. However, as described in Ref. 8, the data were not obtained during all days of interest, and the fluctuations of the data obtained are of such a nature that it is difficult to predict what takes place between the set at the Goldstone tracking station and rise the following day. Even a lesser amount of data was available during the *Mariner II* (1962) and *Mariner IV* (1964) missions, which did not measure the total electron content, but only the charge density at the spacecraft. In the *Mariner* Mars 1969 spacecraft, no plasma experiments were carried similar to those of previous missions.

The scatter among the r_s solutions before and after applying the ionospheric corrections is illustrated in Fig. 9. Before the ionospheric corrections are applied, the scatter among the six solutions is 2 m about the mean. After applying the ionospheric corrections, the scatter is reduced to 1 m, but the average of the solution has jumped 3.5 m. If it could be guaranteed that no serious unknown biases existed, the r_s solution provided for the *Mariner* Mars 1969 mission is well within the ϵ_{r_s} = 1.5-m goal. The effect of the charged particles in the space plasma for the *Mariner* Venus 67 encounter and post-encounter zero-declination cases is the suspected primary cause of the remaining scatter.

[12]"The Troposphere," by V. J. Ondrasik.

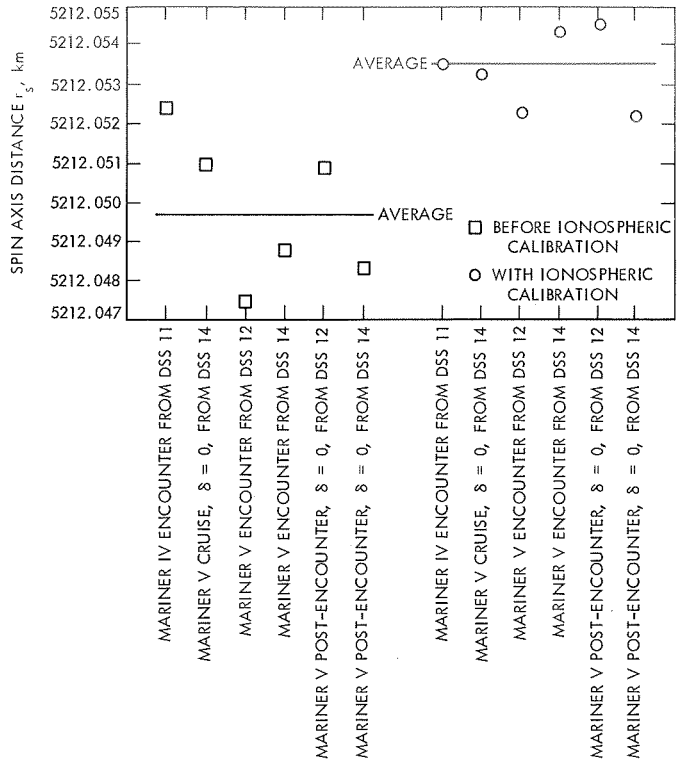

Fig. 9. Post-flight analysis of distance off spin axis

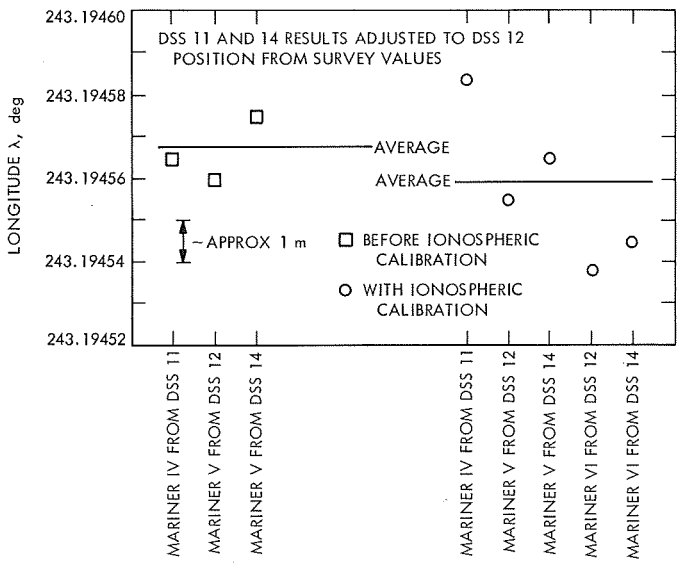

Fig. 10. Post-flight analysis of longitude

Unlike the r_s case, adding the ionospheric corrections made the λ case worse, as illustrated in Fig. 10. In fact, once the ionospheric corrections are applied, there appears to be a drift vs time in the longitude solutions. As discussed in Refs. 5 and 9, the cause of this drift is as yet unknown. The apparent drift, illustrated in Fig. 11 for

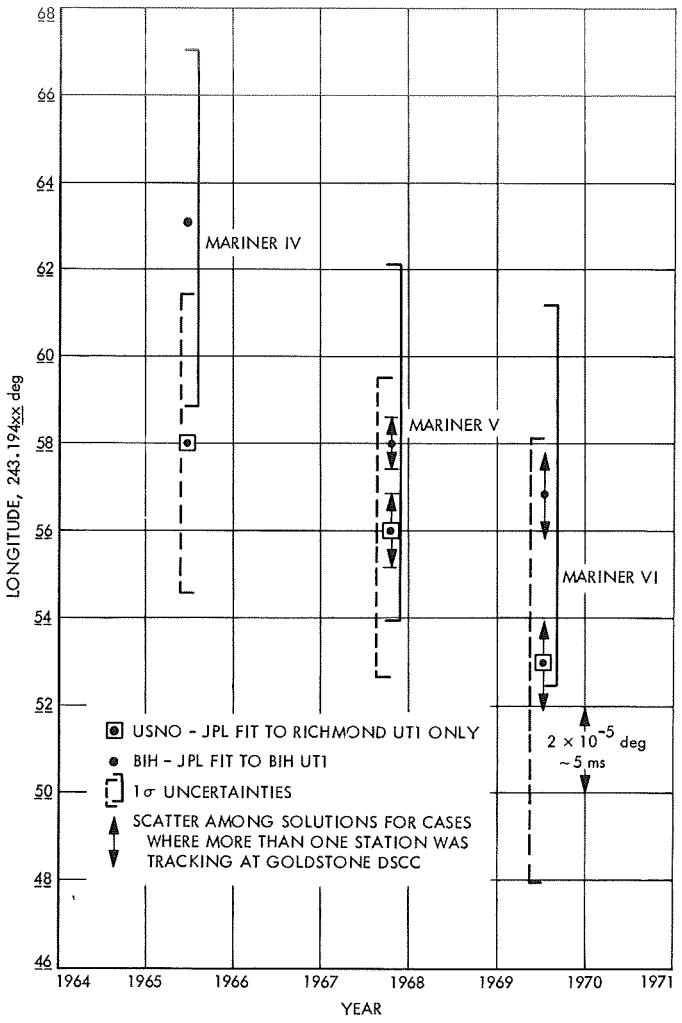

Fig. 11. Longitude solutions for DSS 12 with USNO and BIH UT1

the Goldstone Complex, is 1.2 m per year if UT1 as derived by the USNO is used and 1.5 m per year if the UT1 provided by the BIH is used.

The Goldstone Complex is the only one with as many as six pre-*Mariner* Mars 1969 solutions that can be used to make an r_s scatter comparison. For comparing relative DSS locations with the Goldstone Complex, there is an even more sparse data set available. In this case, the comparison is between those relative locations derived from radio tracking data and those derived from ground survey data. The first-order surveys[13] that have been performed for all the DSSs (Ref. 10) should be good to one part in 10^6 or 0.5 m for stations 50 km apart. The

[13]Communication from B. Bollinger to W. D. Merrick, First-Order Survey Data, Oct. 39, 1964.

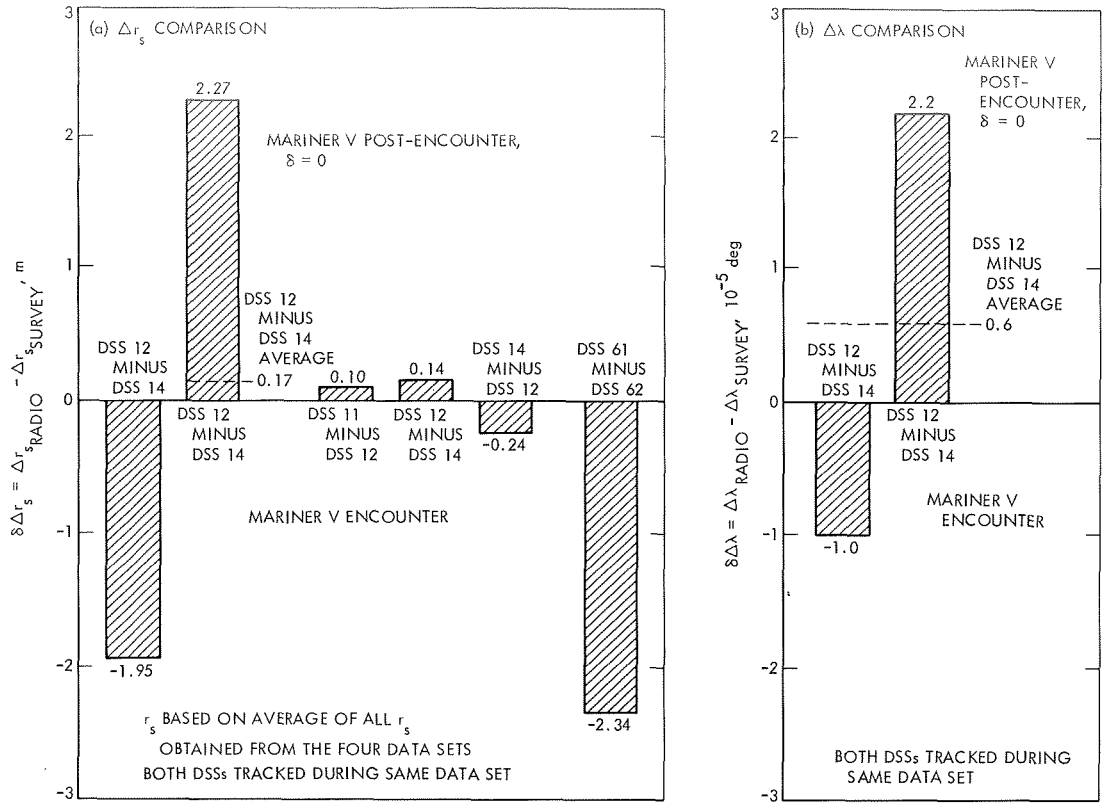

Fig. 12. DSS relative locations: radio tracking minus ground survey

relative DSS distance varies from 2 to 8.5 km within the Goldstone Complex, and the two DSSs at the Madrid Complex are separated by 5 km for r_s and 36 km for λ. However, the two Australian stations are really not within the same complex, and differ by 250 km in r_s and 1,200 km in λ. Not only do these relatively large differential distances rule the Australian stations out of such a comparison to the meter level, but in addition, other investigators (Refs. 11 and 12) report that the Australian geodetic datum has a tilt that would further invalidate such comparisons.

The differences between relative locations derived from radio tracking data minus those determined from ground survey data are shown in Fig. 12. Because of the "observed" drift in the longitude solutions, the only radio-determined relative longitude locations considered are those derived from tracking data spans during which both stations tracked. If these tracking spans are relatively short, not only will this observed drift, but also polar motion and UT1 errors that introduce the same errors in the absolute coordinates, cancel out the relative coordinates. Some reduction is also realized in most other error sources (tropospheric refraction, effect of charged particles, electrical path-link variation through the DSS and the spacecraft) because of the similar ambient conditions, both at the DSS and along the respective DSS–spacecraft communication links. Therefore, these comparisons ought to have less scatter than the repeatability comparisons for the absolute location determinations. However, this is not borne out in Fig. 12, although admittedly the data sample is small.

VI. Recommendations for Future TSAC Activities

A great part of the TSAC resources was spent in devising a scheme to automatically collect, process, and produce calibration data for the *Mariner* Mars 1969 encounter. Hand-processing of data consumed another large portion of TSAC resources when computerized approaches could not be used or there was not sufficient time to develop automated techniques. The problem arises from using the data of various agencies, institutions, and observatories from all corners of the world. Though these organizations proved extremely cooperative and helpful, the requested data could not always be transmitted in a standard format.

To make calibration procedures operational on a routine, as opposed to a research, basis the following steps should be taken:

(1) Models to predict the effects requiring calibration should be developed and perfected to eliminate the need for making measurements especially for in-flight calibration.

(2) Where modelling cannot provide sufficiently accurate calibrations, instrumentation to measure the effects requiring calibration should be installed at each DSS and connected into the tracking data acquisition system so that collection and processing of calibration is as nearly automated as possible.

(3) Measurement techniques that hold the most promise of inherent accuracy should be exploited, as opposed to techniques that have inherent limitation in accuracy, which will make them obsolete for future missions. For example, techniques that provide measurements along the entire probe–DSS ray path should be developed. Also, techniques such as very long baseline interferometry, which will permit the DSN to calibrate timing and polar motion directly, should be exploited.

References

1. Light, J. O., "An Investigation of the Orbit Redetermination Process Following the First Mid-Course Maneuver," in *Supporting Research and Advanced Development*, Space Programs Summary 37-33, Vol. IV, pp. 8–17. Jet Propulsion Laboratory, Pasadena, Calif., June 30, 1965.

2. Hamilton, T. W., and Melbourne, W. G., "Information Content of a Single Pass of Doppler Data From a Distant Spacecraft," in *The Deep Space Network*, Space Programs Summary 37-39, Vol. III, pp. 18–23. Jet Propulsion Laboratory, Pasadena, Calif., May 31, 1966.

3. Hamilton, T. W., Grimes, D. C., and Trask, D. W., "Critical Parameters in Determining Navigational Accuracy for a Deep Space Probe During Planetary Encounter," in *The Deep Space Network*, Space Programs Summary 37-44, Vol. III, pp. 4–11. Jet Propulsion Laboratory, Pasadena, Calif., Mar. 31, 1967.

4. Vegos, C. J., and Trask, D. W., "Tracking Station Locations as Determined by Radio Tracking Data: Comparison of Results Obtained From Combined Ranger Block III Missions and From Baker-Nunn Optical Data," in *The Deep Space Network*, Space Programs Summary 37-43, Vol. III, pp. 3–18. Jet Propulsion Laboratory, Pasadena, Calif., Jan. 31, 1967.

5. Mottinger, N. A., "Status of DSS Location Solutions for Deep Space Probe Missions: Comparison With the SAO Standard Earth 1969 Station Locations," in *The Deep Space Network*, Space Programs Summary 37-62, Vol. II, pp. 41–45. Jet Propulsion Laboratory, Pasadena, Calif., Mar. 31, 1970.

6. Ondrasik, V. J., and Mulhall, B. D., "Estimation of the Ionosphere Effect on the Apparent Location of a Tracking Station," in *The Deep Space Network*, Space Programs Summary 37-57, Vol. II, pp. 29–42. Jet Propulsion Laboratory, Pasadena, Calif., May 31, 1969.

References (contd)

7. Trask, D. W., and Efron, L., "DSIF Two-Way Doppler Inherent Accuracy Limitations: III. Charged Particles," in *The Deep Space Network*, Space Programs Summary 37-41, Vol. III, pp. 3–12. Jet Propulsion Laboratory, Pasadena, Calif., Sept. 30, 1966.

8. Ondrasik, V. J., Mulhall, B. D., and Mottinger, N. A., "A Cursory Examination of the Effect of Space Plasma on Mariner V and Pioneer IX Navigation With Implications for Mariner Mars 1971 TSAC," in *The Deep Space Network*, Space Programs Summary 37-60, Vol. II, pp. 89–94. Jet Propulsion Laboratory, Pasadena, Calif., Nov. 30, 1969.

9. Fliegel, H. F., and Lieske, J. H., "Inherent Limits of Accuracy of Existing UT1 Data," in *The Deep Space Network*, Space Programs Summary 37-62, Vol. II, pp. 46–49. Jet Propulsion Laboratory, Pasadena, Calif., Mar. 31, 1970.

10. *Position of DSS 14 Antenna*, Report. Teledyne, Inc., Monrovia, Calif., Nov. 1966.

11. Fischer, I., and Slutsky, M., "A Preliminary Geoid Chart of Australia," published in the *Australian Surveyor*. Army Map Service, Washington, D. C., Dec. 1967.

12. Fischer, I., Slutsky, M., Shirley, F. R., and Wyatt, P. Y., IV, *New Pieces in the Picture Puzzle of an Astrogeodetic Geoid Map of the World*. Army Map Service, Washington, D. C., Sept. 1967.

Station Locations

N. A. Mottinger and W. L. Sjogren

I. Introduction

When undertaking a task as complex as navigating a deep space probe to a specified target, it is important to have a simple representation of fundamental processes involved. The Hamilton-Melbourne model of the information content of doppler data (Ref. 1), discussed in the preceding article, supplies such a need for orbit determination with the use of earth-based radio tracking. The parameterization method developed by Hamilton and Melbourne can be used to determine how well station locations must be known to meet navigation accuracy requirements. The method was used by Hamilton, Trask, and Grimes (Ref. 2) to determine the uncertainties in r_s (station distance off earth's spin axis) and λ (station longitude) needed to support the *Mariner* Mars 1969 navigation accuracy requirements. Since station locations and probe position are highly correlated, the station locations can be estimated when the location of the probe is known in inertial space. The right ascension and declination of the probe are determined by the ephemeris of a body (other than the earth) that is exerting strong gravitational forces on the probe. This occurs at planetary or lunar encounter and enables r_s and λ to be estimated. With more careful observation of the model it can be noted that at zero geocentric declination the uncertainty in the probe position does not degrade the information content of the doppler data for estimating r_s. The zero-declination cases available have never been noted to occur at encounter, but rather in deep interplanetary space when only the distant sun is the primary attracting body. At this time it is assumed that it is not possible to determine the absolute longitude, but rather the difference in longitude between stations.

All missions for which earth-based radio tracking is available were considered as possible sources for station locations. These fell generally into two categories, lunar and planetary. None of the lunar missions offered zero-declination cases independent of encounter (impact), whereas *Mariner* V offered two. One occurred during

cruise and the other after encounter. All together, 21 different data periods were considered. In the final analysis many had to be omitted because of lack of sufficient analysis and/or lack of charged-particle calibrations. In the case of the lunar missions, disagreements with the planetary absolute-longitude solutions exceeded allowable limits for combination.

One very significant factor in reducing the uncertainty in the location estimates was the ionosphere calibrations. In the cases of greatest scatter among r_s solutions, these corrections reduced uncertainty from 5 m to approximately 2⅓ m.

Improved methods and programs for combining station location estimates were used to make optimum use of the information obtained in the orbit-determination program and to constrain the relative locations within a complex of tracking stations to the geodetic survey relative locations.

II. Data Set and Solutions Obtained

Although there were 21 different data packages considered as possible sources for station locations, those computed for *Mariner* Mars 1969 were obtained from only 5. There were many probes among these 21 that offered several opportunities. For example, the cruise and lunar orbit phase of four *Lunar Orbiters* and the cruise and post-touchdown phases of five *Surveyors* were all potential location sources. There are essentially two reasons why these were not included in the final analysis. In some cases the analysis had not been done or in others there were problems peculiar to the particular mission in terms of modeling inadequacies that have inhibited the ability to produce, among other things, consistent station location solutions. The second reason would suffice in itself—a fundamental discrepancy between the lunar and planetary ephemerides produces solved-for station longitudes that do not agree below the 3-m level with the planetary-derived longitude solutions. When this difference was originally noted and confirmed by Van Flandern (Ref. 3), the difference was approximately 20 m. The use of lunar ephemerides that are corrected for this difference has not produced station locations as consistent as expected with the changes induced in the lunar ephemeris or with the existing planetary longitudes.

Although the solutions would have to be obtained from the existing planetary flights, this was really not too restrictive. In addition to the *Mariner IV* and V encounter solutions, there were the two *Mariner* V zero-declination reductions and various *Pioneer* zero-declination situations already available. Others were requested and the tracking data were obtained. During the early part of the mission, simple techniques were used to combine the estimates obtained from the *Mariners* and *Pioneer VII*. Later in the mission, ionosphere calibrations were available, but only for the *Mariners*; even so, at least one solution remained for each station in the network.

Solutions obtained with the Single Precision Orbit Determination Program (SPODP) (Ref. 4) used *Mariner IV* encounter and the *Mariner V* zero-declination and encounter data. These solutions produced locations accurate to 5 m (Refs. 5 and 6). The same data were then reprocessed with the improved third-generation orbit determination program, the Double Precision Orbit Determination Program (DPODP).[1] *Pioneer VII* zero-declination solutions were used with the *Mariners* to produce a set of station locations, location set (LS) 17, to support the launch and premidcourse activities of the *Mariner* Mars 1969 mission. The simple averaging technique of weighting each solution by 1 over its variance was used to produce this set. These results when compared as in Table 1 with the best set, LS 14, from the SPODP showed an average difference of 1 m in r_s and 1.6 m in λ. Since the DPODP and SPODP were to support the *Mariner* Mars 1969 orbit determination effort,

[1]Mottinger, N. A., *Breaking the 5-Meter Level in Obtaining Station Location Solutions From the Reduction of Radio Probe Data,* JPL Internal Report, Oct. 2, 1969.

Table 1. First DPODP estimates compared with best SPODP

Deep Space Station	DPODP (LS 17) — SPODP (LS 14)	
	Δr_s, m	$\Delta_{\Delta\lambda}$ from 12,[a] m
DSS 12	0.1	1.0
DSS 41	0.5	0.7
DSS 42	0.8	1.3
DSS 51	3.0	4.2
DSS 61	3.3	1.5
DSS 62	0.4	2.2
Average	1.0	1.6

[a]Note: $(\lambda_i - \lambda_{12})_{LS\ 17} - (\lambda_i - \lambda_{12})_{LS\ 14}$

the general harmony displayed between the results of the data reduction techniques employed in both programs served to increase the confidence of the capabilities of each.

The "worst case" example of the consistency among station location solutions is shown in Figs. 1 and 2. Two sets of DPODP solutions are shown in these figures. Those to the left are labeled NO IONOSPHERE to distinguish them from those on the right, which were obtained after the ionosphere corrections were applied. Before application of the ionosphere corrections, an approximate 5-m scatter exists in the r_s solutions and about 1½ m in longitude. Their application will be discussed in more detail in Section IV of this article. It can be noted in Fig. 2 how the planetary longitude solutions agreed before and after the application of the charged-particle calibrations. The spread increased slightly to 2½ m from 1¾. This may be due to errors in the ephemerides, precession constants for the earth-centered coordinate system, or in the star catalogs used to compute UTI at the Naval Observatory.[2] Also significant is the additional ½-m spread in longitude induced by processing the *Mariner IV* data with the specific ephemeris,[3] DE 71, developed to support the encounter activities of *Mariner* Mars 1969. This ephemeris is not recommended for general use; however, as part of the station location effort, the *Mariner IV* data were refit and produced the expected ½-m change in longitude. In the combining process, however, the *Mariner V* solutions dominated the leasts squares adjustment because of its smaller uncertainties and essentially negated the effects of the change in *Mariner IV*.

The various solutions obtained for all stations in the DSN are presented in Tables 2, 3, and 4. Information concerning the time span of each flight used in the DPODP is shown in Tables 5 and 6. Other important factors affecting their derivation will be discussed in following sections.

III. Timing Polynomials and Polar Motion Effects on *Mariner* Mars 1969 Station Locations

To reduce earth-based radio tracking data to the accuracy required for nearly all space ventures, it is necessary to represent the differences between universal time coordinated (UTC), UT1, ephemeris time (ET), and atomic time (A.1). A linear relationship is used for A.1–ET relationships and a quadratic for UT1–UTC. These are prepared from timing information supplied by the U.S. Naval Observatory as described in the next article in this report.[4]

At the time of launch it was necessary to modify the longitudes provided to account for a redefinition of UT1 disseminated by the U.S. Naval Observatory after January 1, 1968. This introduced a discontinuity between the timing system used to produce station locations and the timing system used to reduce the *Mariner* Mars 1969 data. To counteract this, the longitude of each station was increased 3×10^{-5} deg prior to updating for polar motion.

Before encounter occurred, this situation was corrected. Corrections were made so that the continuity of UT1 was not interrupted between the previous and present mission and, furthermore, the raw data supplied by Muller and Chao (Ref. 7) had been recomputed using the Bureau International de l'Heure (BIH) polar motion. A new program was developed to prepare the necessary polynomials representing the required relationships. The previous data were reduced by the DPODP with these new polynomials and were noted to show excellent agreement between observed changes in UT1–UTC and the longitude solutions obtained. It was therefore no longer necessary to apply any corrections for timing discontinuities.

Before any Location Set could be used by the SPODP to process the *Mariner data,* it was necessary to update it for the polar motion predicted by Muller and Chao. Updating of the SPODP took place at intervals sufficient to minimize the effects of the unmodeled polar motion on the data reduction.[5] As the updating was required, only the current best set of station locations was corrected. Updating in the DPODP is handled by inserting new polar motion model coefficients obtained when new timing coefficients are produced. The station locations used for input were at the reference, 1903.0 pole. The updated station locations supplied for use by the SPODP are listed in the Appendix.

---

[2] *Ibid.*

[3] O'Handley, D. A., *Ephemeris of Mars for Mariners VI and VII,* JPL Internal Report, Aug. 15, 1969.

[4] "Timing Errors and Polar Motion," by P. M. Muller and C. C. Chao.

[5] A description of the effect of polar motion on station locations is given by P. M. Muller in *Polar Motion and DSN Station Locations,* JPL Internal Report, Apr. 20, 1967.

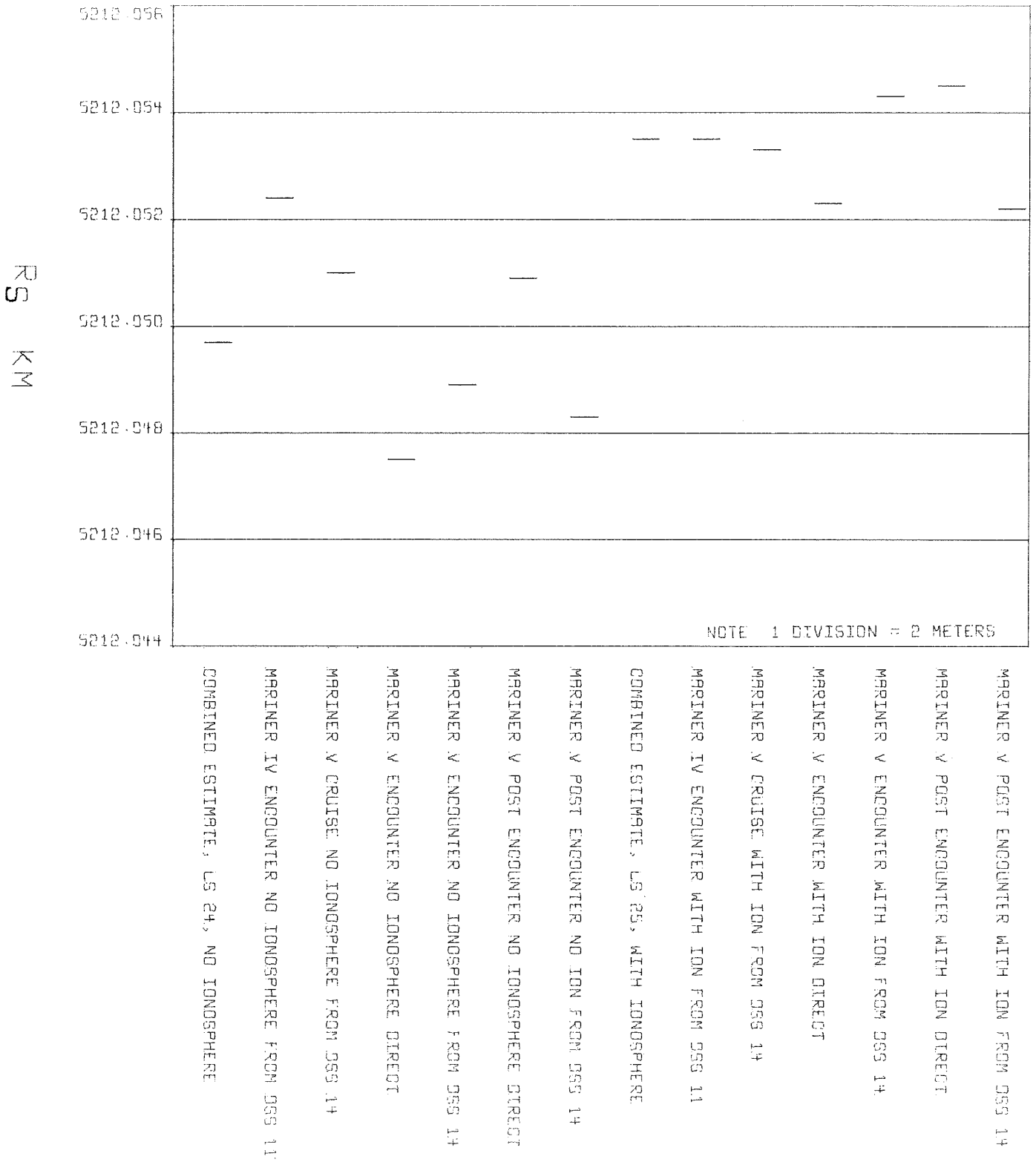

Fig. 1. Distance off spin axis, earth-fixed system (1903.0 pole), DSS 12

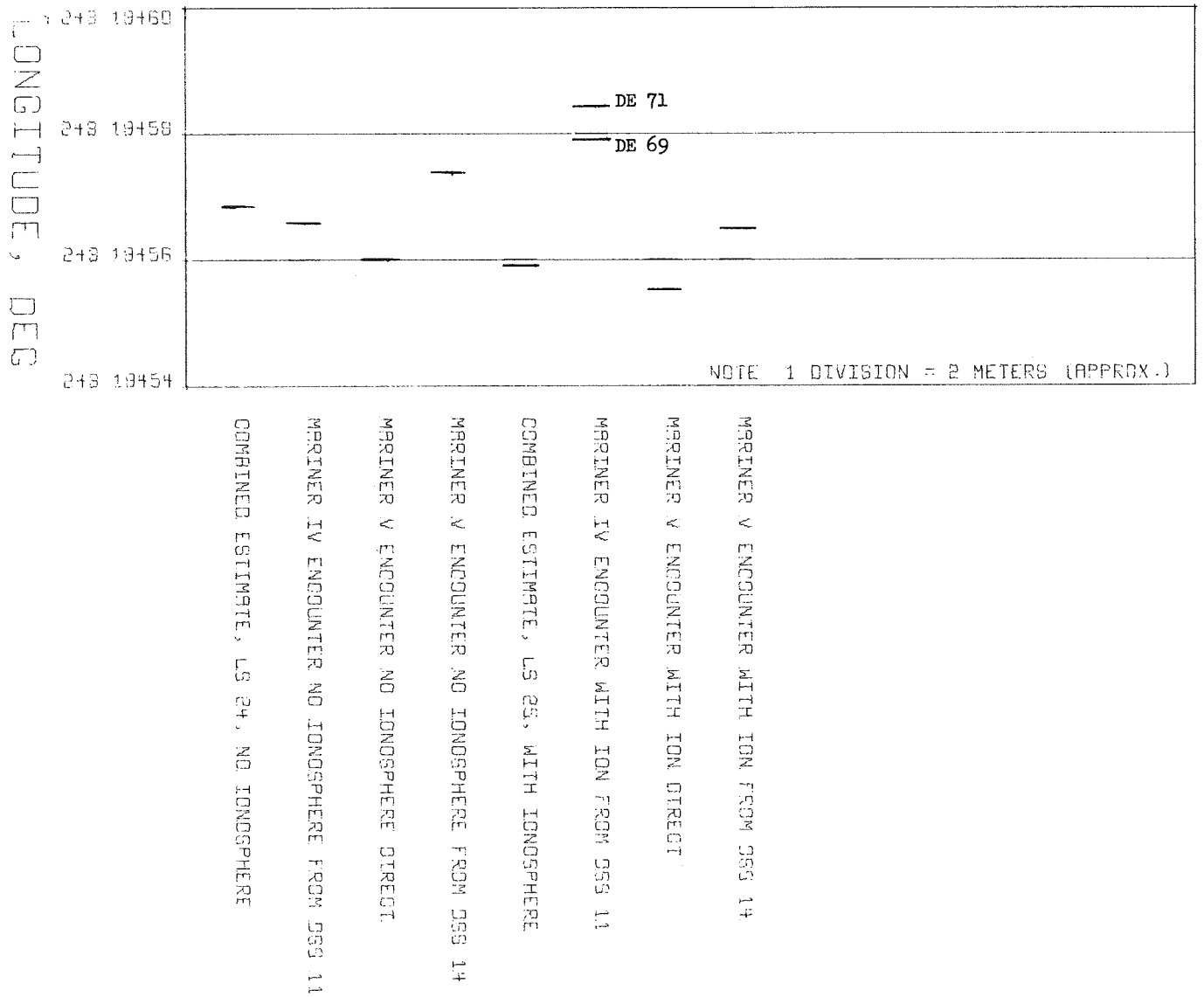

Fig. 2. Geocentric longitude, earth-fixed system (1903.0 pole), DSS 12

Table 2. Absolute station locations and statistics: non-ionosphere reductions

DSS	Data source	Distance off spin axis, km	1 σ standard deviation,[a] m	Geocentric longitude,[b] deg	1 σ standard deviation,[a] 10^{-5} deg	Distance along spin axis,[c] km
11		5206.3xxx		243.15xxxx		3673.xxx
	Mariner IV encounter	40.8	2.9	063.3	5.6	759
	Pioneer VIIA	40.8	1.6	045.4	17.0	759
	Pioneer VIIIA	38.2	1.9	068.6	109.0	759
12		5212.0xxx		243.19xxxx		3665.xxx
	Mariner V encounter	47.5	2.1	456.0	3.6	624
	Mariner V post-encounter	50.9	1.9	458.8	9.8	624
	Pioneer VIIA	50.8	1.2	438.2	16.5	624
	Pioneer VIIIB	48.4	3.6	431.8	77.4	624
	Pioneer IX	46.9	5.8	449.8	61.0	624
14		5203.9xxx		243.11xxxx		3677.xxx
	Mariner V cruise	96.4	2.4	053.1	9.2	048
	Mariner V encounter	94.2	1.7	052.8	3.6	048
	Mariner V post-encounter	93.6	3.0	052.3	9.8	048
	Pioneer VIIB	95.7	2.5			
	Pioneer IX	99.2	5.7	043.8	62.0	048
41		5450.xxxx		136.88xxxx		−3302.xxx
	Mariner V encounter	197.5	2.1	753.1	3.0	238
	Mariner V post-encounter	200.0	2.4	757.8	9.7	238
	Pioneer VIIA	200.6	8.0	736.5	17.6	238
42		5205.3xxx		148.98xxxx		−3674.xxx
	Mariner IV encounter	49.4	2.9	128.8	5.0	628
	Mariner V cruise	50.3	1.4	131.1	9.3	628
	Pioneer VIIA	51.9	1.6	112.9	16.5	628
	Pioneer VIIIA	47.8	1.6	137.8	108.0	628
	Pioneer VIIIB	47.5	2.1	100.4	75.7	628
	Pioneer IX	42.4	7.8	126.8	62.0	628
51		5742.9xxx		27.68xxxx		−2768.xxx
	Mariner IV encounter	40.8	2.6	543.2	4.5	760
	Pioneer VIIIB	37.0	2.4	519.2	75.7	760
	Pioneer IX	39.7	9.1	539.6	62.0	760
61		4862.6xxx		355.75xxxx		4114.xxx
	Mariner V cruise	03.7	1.4	101.9	9.3	829
	Mariner V post-encounter	05.6	5.5	103.3	10.4	829
	Pioneer VIIIA	12.0	1.9	107.4	109.0	829
62		4860.8xxx		355.63xxxx		4116.xxx
	Mariner V cruise	14.9	2.1	221.9	9.8	950
	Mariner V encounter	15.1	2.0	222.1	3.3	950
	Mariner V post-encounter	15.5	2.4	223.4	10.0	950
	Pioneer IX	12.7	8.1	207.5	69.0	950

[a]These are formal uncertainties computed by the DPODP. They do not include uncertainties in universal time, polar motion, ephemeris, ionosphere, or space plasma, but are about 1½ times the visible noise on the data.

[b]The minor part may be assumed to be tabulated in meters where the equivalence of 10^{-5} deg at DSS 11, 12, and 14 is 0.91, at DSS 61 and 62 is 0.85, at DSS 51 is 1.00, at DSS 41 is 0.95, and at DSS 42 is 0.91.

[c]This component was not estimated, but is included for completeness.

Table 3. Absolute station locations: ionosphere reductions

DSS	Data source	Distance off spin axis, km	1 σ,[a] m	Geocentric longitude,[b] deg	1 σ,[a]	Distance along spin axis,[c] km
11		5206.3xxx		243.15xxxx		3673.xxx
	Mariner IV encounter	41.8	2.9	065.3	6.2	763
12		5212.0xxx		243.19xxxx		3665.xxx
	Mariner V encounter	52.3	2.1	455.5	3.6	628
	Mariner V post-encounter	54.5	2.0	459.4	10.8	628
14		5203.9xxx		243.11xxxx		3677.xxx
	Mariner V cruise	98.6	2.7	057.7	4.9	052
	Mariner V encounter	99.6	1.7	051.9	3.6	052
	Mariner V post-encounter	97.5	3.0	052.6	10.8	052
41		5450.xxxx		136.88xxxx		−3302.xxx
	Mariner V encounter	198.0	2.1	749.7	3.0	243
	Mariner V post-encounter	200.3	3.0	756.8	10.7	243
42		5205.3xxx		148.98xxxx		−3674.xxx
	Mariner IV encounter	50.1	3.3	130.3	5.8	646
	Mariner V cruise	50.5	2.0	136.8	6.0	646
51		5742.9xxx		27.68xxxx		−2768.xxx
	Mariner IV encounter	42.1	3.2	544.1	5.0	744
61		4862.6xxx		355.75xxxx		4114.xxx
	Mariner V cruise	06.9	1.6	107.0	6.0	829
62		4860.8xxx		355.63xxxx		4116.xxx
	Mariner V encounter	17.9	2.0	219.8	3.3	908
	Mariner V post-encounter	20.1	3.0	224.3	11.0	908

[a]These are formal uncertainties computed by the DPODP. They do not include uncertainties in universal time, polar motion, ephemeris, ionosphere, or space plasma, but are about 1½ times the visible noise on the data.

[b]The minor part may be assumed to be tabulated in meters where the equivalence of 10^{-5} deg at DSS 11, 12, and 14 is 0.91, at DSS 61 and 62 is 0.85, at DSS 51 is 1.00, at DSS 41 is 0.95, and at DSS 42 is 0.91.

[c]This component was not estimated, but is included for completeness.

Table 4. Relative longitude solutions: non-ionosphere

Data source	Goldstone DSS 12 minus:				
	DSS 41	DSS 42	DSS 51	DSS 61	DSS 61
	906.30xxxx	94.21xxxx	215.50xxxx	−112.55xxxx	−112.43xxxx
Mariner IV encounter		327.6	913.3		
Mariner V cruise		326.6		644.3	764.3
Mariner V encounter	702.9				766.1
Mariner V post-encounter	701.0			644.5	764.6
Pioneer VIIA	701.7	325.3			
Pioneer VIIIA		323.9		645.7	
Pioneer VIIIB		331.4	912.6		
Pioneer IX		323.0	910.2		757.7

Table 5. Flight analysis summary: non-ionosphere reductions

Flight	Doppler tracking, No. of points	Doppler count time, s	Tracking span	Ephemeris		DPODP		ET–UTC, s	UTI–UTC, ms	Effective data weights, 1 pt/min, mm/s	Instantaneous pole position (Bureau International de l'Heure)				Declination, deg	SEP[a] angle, deg	Location set
				DE[a]	LE[a]	MOD[a]	Lock file				X, M	Change in X, M	Y, M	Change in Y, M			
Mariner IV encounter	419	600 and 60	14 days (July 5–21, 1965)	69	16	5.0	5A	36.178	19	3.3	−2.9	1.3	13.9	0.6	−3	77	22, 24
Mariner V cruise	616	600	57 days (July 21–Sept. 16, 1967)	69	16	4.3	5A	Start 37.965 End 38.113	66 94	3.3	−0.2	0.5	6.5	0.4	−8 to +8	35–20–35	22, 24
Mariner V encounter	561	600	10 days (Oct. 14–24, 1967)	69	16	5.0	5A	38.198	107	3.3	−0.5	0.1	6.5	0.1	6	45	22, 24
Mariner V post-encounter	665	600	15 days (Oct. 29–Nov. 12, 1967)	69	16	5.0	5A	38.240	100	3.3	−0.6	0.03	6.7	0.4	2 to −2	43	22, 24
Pioneer VIIA	1392	600	42 days (Aug. 30–Sept. 30, 1966)	69	16	5.0	5A	Start 37.095 End 37.204	13 30	3.3	0.8	2.4	10.9	0.4	−1.4 to 0.8	150	22
Pioneer VIIB	75	60	7 days (July 27–Aug. 3, 1968)	69	16	5.0	5A	38.837	36	3.3	2.6	0.06	5.2	0.1	3 to −2	54	22
Pioneer VIIIA	370	300	8 days (June 3–11, 1968)	69	16	5.0	5A	38.699	−4	3.3	1.5	0.2	6.7	0.2	1.3 to −1.3	102–105	—
Pioneer VIIIB	520	600	18 days (Dec. 25, 1968–Jan. 12, 1969)	69	16	5.0	5A	39.244	30	3.3	−4.6	0.5	7.6	1.2	−2.8 to +5.0	80	—
Pioneer IX	309	600	5 days (May 8–13, 1969)	69	16	5.0	5A	39.573	−1	3.3	1.0	0.3	11.4	0.06	−3 to +3	50	—

[a]DE Development Ephemeris
LE Lunar Ephemeris
MOD DPODP identifier
SEP Sun–earth–probe

Table 6. Flight analysis summary: ionosphere reductions

Flight	Doppler tracking, No. of points	Tracking span	Ephemeris		DPODP[a]		Effective data weights, 1 pt/min, mm/s	Location set
			DE[a]	LE[a]	MOD[a]	Lock file		
Mariner IV encounter	373	11 days (July 10–21, 1967)	71	16	5.0	5A	3.3	25
Mariner V cruise	364	57 days (July 21–Sept. 16, 1967)	69	16	5.0	5A	3.3	25
Mariner V encounter	561	10 days (Oct. 14–24, 1967)	69	16	5.0	5A	3.3	25
Mariner V post-encounter	411	15 days (Oct. 29–Nov. 12, 1967)	69	16	5.0	5A	3.3	25

[a]DE Development Ephemeris
LE Lunar Ephemeris
MOD DPODP identifier

IV. Atmospheric Effects on Derived Station Locations

Two distinct portions of the atmosphere have important effects on the propagation of the radio signal received from a deep space probe. One of these, the troposphere, could be modeled with sufficient accuracy to meet the goals of the *Mariner* Mars 1969 mission, but the charged-particle effects of the ionosphere had to be calibrated with many different data types and data handling techniques as described later in this report.[6] The effects of the ionosphere can be seen in Figs. 1 and 2, in which r_s and λ solutions are shown before and after ionosphere corrections were applied. These effects are representative of the changes that occurred at the Northern Hemisphere stations, which at the time *Mariner IV* and *V* missions were under the influence of higher ionospheric activity than those in the Southern Hemisphere. Differences at all the stations are given in Table 7. Calibrations for the *Pioneer* data did not arrive in time for processing.

Changes were made in the troposphere model[7] when it was noted that the model could be improved. This resulted in small changes to r_s only. To obtain these, time permitted only refitting the *Mariner V* cruise zero-declination case to the new refraction model. The deltas obtained are listed in Table 8. These were applied only

[6]"The Ionosphere," by B. D. Mulhall, V. J. Ondrasik, and K. L. Thuleen.

[7]See "The Troposphere," by V. J. Ondrasik.

Table 7. Differences due to ionosphere corrections: LS 25 − LS 24

DSS	Δr_s, m	$\Delta\lambda$, m	Δ Relative λ: DSS 12 minus DSS xx
11	3.8	−0.94	
12	3.8	−0.94	
14	3.8	−0.96	
41	0.26	−3.24	2.3
42	−0.28	−0.32	−0.62
51	−0.61	−0.84	−0.1
61	3.47	−1.04	0.1
62	3.45	−1.08	0.14

Table 8. Corrections to r_s for new troposphere model

DSS	Value added to old solutions, m
11	0.5
12	0.5
14	0.6
41	0.8
42	0.8
51	0.8
61	0.7
62	0.7

to the station locations being used by the DPODP, since the original model was retained in the SPODP.

The ionosphere calibrations have been applied only to station location solutions obtained from past missions. To use these locations for the inflight reduction of *Mariner* Mars 1969 data, it was necessary to apply the corrections to the data and then redetermine the encounter point. The application was a two-step operation following the initial reductions of the 1969 data with the use of the current best set of non-ionosphere-corrected station locations. The "zeroth" step was one that had already occurred as a part of the inflight data processing—the orbit determination program is run to form the residuals between the observed and computed data types. The first step is to apply the ionosphere corrections to these residuals, with the use of program MODIFY.[8] The third step is to resolve the normal equations with these modified residuals. However, for the application of the ionosphere corrections to be meaningful in determining the changes on the spacecraft trajectory, it would be necessary to have the computed data based on the ionosphere-corrected station locations. To do this would have required long, time-consuming reductions, so a method of effectively tricking the program into behaving as if this had been done was used. When the normal equations were resolved with the modified residuals, station locations were "estimated," but the ionosphere corrected locations were input as *a priori* final estimates in the vector of estimated parameters (which included the probe orbit).[9] Because of the high correlation between the probe orbit and the station locations, the orbit would change as a result of the induced change in station locations and also as a function of the modified residual used in the normal equations. Mapping the newly obtained estimates of the spacecraft position and velocity vector permitted an estimate of the ionosphere effects on the aiming point to be made.

V. Combination Techniques

An important part in preparing the best estimate of station locations for use in the *Mariner* Mars 1969 mission was the technique used to combine the various solutions. The first set of station locations, LS 17, was prepared for *Mariner* Mars 1969 with each solution being weighted by 1 over its variance. At the Goldstone Complex, where the stations are within 10 km of one another, geodetic survey locations were used to compute the relative position of the three antennas with respect to one another. This information was used to transfer a solution obtained from DSS 11 or DSS 14 to DSS 12, and then these locations for DSS 12 were combined and the relative locations reapplied to determine positions for DSS 11 and 14. Although the antennas at the Madrid Complex are close to one another also, the survey data had not been verified in time for use in a similar manner during the construction of LS 17. This information did become available, however, and was used in later combinations. The stations at the Canberra Complex are about 12 and 4 deg apart in longitude and latitude, respectively. The geodetic surveys have been checked at these sites, but the differences between the relative locations derived from them and those obtained from radio tracking are 11 and 28 m in λ and r_s, respectively. These are obviously much too large for use in transferring locations from one site to another when 3-m or better accuracies are required. As can be seen in Figs. 1 and 2, the relative locations obtained from radio tracking agree with the relative survey location to about 2 m in r_s and about 1 m in λ at Goldstone. Similar results have been noted for the Madrid stations.

To do a more rigorous job of preparing location sets, a statistical combination technique was programmed (Ref. 8). This technique uses the normal equations matrix computed by the orbit determination program to produce a reduced normal matrix of the parameters in that solution, which is to be combined with similar parameters from other reductions. Slight modification was necessary for the zero-declination cases where r_s and relative λ are determined. The orbit determination program directly estimates absolute locations. In doing so, it often attaches statistical significance to solutions not predicted by the Hamilton–Melbourne model (Ref. 1). To "rearrange" the information in the normal matrix so as to destroy the unrealistic information on absolute longitude and maintain the realistic relative longitude information, the normal matrix was inverted and an arbitrary factor, 0.01 deg, was combined in a root-mean-squared sense with the longitude terms. The matrix was then reinverted to produce the desired normal matrix. The double inversion is undesirable from a numerical standpoint, and new techniques will be investigated for accomplishing this "rearranging" task. In the time available to prepare the program this was deemed adequate and appeared to work effectively.

---

[8]Described in *User's Guide to MODIFY, Version 2*, by R. W. Schumann (in press).

[9]To ensure that the differences between the two sets of station locations were maintained, a tight *a priori* standard deviation of 0.03 m was input.

Table 9. Relative locations at Goldstone and Madrid complexes — computed from geodetic survey reductions

Goldstone

	−DSS 11	−DSS 12	−DSS 14	
DSS 11		−5.7117 km	2.3430 km	Δr_s
		−0.043931 deg	0.040114 deg	$\Delta\lambda$
		8.1353 km	−3.288 km	Δz
DSS 12			8.0547 km	Δr_s
			0.084046 deg	$\Delta\lambda$
			−11.42364	Δz

Madrid

	−DSS 62	
DSS 61	1.7902	Δr_s km
	0.118807	$\Delta\lambda$ deg
	−2.0232	Δz km

Relative Locations								
DSS	Minus	DSS	LS 22[a]		LS 24[b]		LS 25[b]	
			$\Delta\lambda$, deg	Δr_s, km	$\Delta\lambda$	Δr_s	$\Delta\lambda$	Δr_s
12	→	41	106.307025	−238.1482	106.307029	−238.1487	106.307052	−238.1451
12	↓	42	94.213261	6.6997	94.213264	6.6996	94.213258	6.7032
12	↓	51	215.509124	−530.8909	215.509128	−530.8913	215.509127	−530.8881
12	↓	61	−112.556444	349.4463	−112.556449	349.4454	−112.556448	349.4457
12	↓	62	−112.437653	351.2350	−112.437643	351.2356	−112.437641	351.2359
41	↓	42	− 12.093764	244.8480	− 12.093764	244.8483	− 12.093794	244.8483
41	↓	51	109.202099	−292.7426	109.202099	−292.7427	109.202075	−292.7430
41	↓	61	−218.863470	587.5946	−218.863478	587.5940	−218.863500	587.5908
41	↓	62	−218.744679	589.3832	−218.744671	589.3842	−218.744693	589.3811
51	↓	61	−328.065568	880.3372	−328.065577	880.3367	−328.065575	880.3339
51	→	62	−327.946777	882.1258	−327.946770	882.1269	−327.946768	882.1241

[a]Relative locations for DSS 12−11, 12−14 in Table 7, 61 and 62 not constrained.

[b]Relative locations for DSS 12−11, 12−14, 61−62 listed in Table 7.

Table 10. Absolute locations

LS 17					
DSS	*RI*, km	ϕ, deg	λ, deg	r_s, km	Z, km
11	6372.0062	35.208019	243.15070	5206.3382	3673.759
12	6371.9905	35.118642	243.19463	5212.0498	3665.624
14	6371.9892	35.244330	243.11059	5203.9950	3677.048
41	6372.5534	−31.211386	136.88760	5450.1983	−3302.238
42	6371.7003	−35.219524	148.98138	5205.3505	−3674.628
51	6375.5291	−25.739440	27.68552	5742.9382	−2768.760
61	6369.9899	40.238519	355.75108	4862.6077	4114.829
62	6369.9924	40.263496	355.63228	4860.8154	4116.950

LS 17				
DSS	Minus	DSS	$\Delta\lambda$	Δr_s
12	→	41	106.30703	−238.1485
12	↓	42	94.21325	6.6993
12	↓	51	215.50911	−530.8884
12	↓	61	−112.55645	349.4421
12	↓	62	−112.43765	351.2344
41	↓	42	− 12.09378	244.8478
41	↓	51	109.20208	−292.7399
41	↓	61	−218.86348	587.5906
41	↓	62	−218.74468	589.3829
51	↓	61	−328.06556	880.3305
51	↓	62	−327.94676	882.1228
61	→	62	0.11880	1.7923

LS 22					
DSS	*RI*, km	ϕ, deg	λ, deg	r_s, km	Z, km
11	6372.0065	35.208017	243.150630	5206.3386	3673.759
12	6371.9907	35.118640	243.194561	5212.0501	3665.624
14	6371.9895	35.244328	243.110516	5203.9955	3677.048
41	6372.5535	−31.211386	136.887536	5450.1983	−3302.238
42	6371.7002	−35.219525	148.981300	5205.3504	−3674.628
51	6375.5316	−25.739430	27.685437	5742.9410	−2768.760
61	6369.9869	40.238543	355.751006	4862.6038	4114.829
62	6369.9922	40.263498	355.632215	4860.8151	4116.950
LS 24					
11	6372.0084	35.208049	243.150637	5206.3381	3673.763
12	6371.9927	35.118672	243.194568	5212.0497	3665.628
14	6371.9915	35.244360	243.110523	5203.9951	3677.052
41	6372.5561	−31.211425	136.887540	5450.1984	−3302.243

Table 10 (contd)

LS 24 (contd)					
DSS	RI, km	ϕ, deg	λ, deg	r_s, km	Z, km
42	6371.7103	−35.219659	148.981300	5205.3501	−3674.646
51	6375.5247	−25.739300	27.685441	5742.9410	−2768.744
61	6370.0235	40.238924	355.751018	4862.6043	4114.885
62	6369.9643	40.263216	355.632211	4860.8141	4116.908
LS 25					
11	6372.0115	35.208029	243.150627	5206.3419	3673.763
12	6371.9958	35.118652	243.194559	5212.0535	3665.628
14	6371.9946	35.244340	243.110513	5203.9989	3677.052
41	6372.5563	−31.211423	136.887507	5450.1986	−3302.243
42	6371.7106	−35.219658	148.981301	5205.3504	−3674.646
51	6375.5252	−25.739297	27.685432	5742.9417	−2768.744
61	6370.0262	40.238904	355.751007	4862.6078	4114.885
62	6369.9670	40.263196	355.632200	4860.8176	4116.908

To constrain the relative locations at the Goldstone and Madrid Complexes, a covariance matrix was constructed similar to that developed for the zero-declination cases. Very large sigmas (1000 km) were assigned to the absolute survey locations, but very tight sigmas (0.3 m) to the relative locations. Correlations were computed and the off-diagonal terms constructed. No correlation was assumed to exist between λ and r_s. This covariance matrix was inverted and used directly as an information matrix in the combination program. The relative locations obtained from the combination were observed to have been held to a 0.01-m level. In the future it would be better to use a more rigorous method to compute the relative location uncertainties between the antennas. Perhaps the uncertainty should be a function of the distance between the sites.

Three location sets—LS 22, 24, and 25—were computed with this program while the mission was in progress. Their constituent runs are given in Tables 5 and 6. It should be noted that the *Mariner IV* DE 71 station locations were used only in the ionosphere set, LS 25. The *Mariner V* DE 69 solutions were used in the non-ionosphere sets LS 24 and 22. However, in both sets *Mariner V* dominated because of the significantly smaller uncertainties on its solutions.

Information for future comparisons of these sets is included in Tables 2–6. Tables 2 and 3 list the solutions obtained and the formal statistics for each; Table 4 gives the relative longitude for the non-ionosphere runs. Tables 5 and 6 summarize the data arc, ephemeris, orbit determination program, timing relations, pole position, declination, and sun–earth–probe angle for each planetary mission considered. The relative locations at Goldstone and Madrid from geodetic survey data are given in Table 9, and Table 10 lists the absolute location sets 17, 22, 24, and 25.

The third component of station locations, distance along the earth's spin axis Z, cannot be obtained from reducing the tracking data from the previously discussed missions. Similarly, the insensitivity of the doppler to the Z component does not affect the real-time orbit determination. For this reason, values obtained from geodetic surveys have been used successfully for mission support. Values for Z obtained from reductions of Baker-Nunn optical data performed at the Smithsonian Astrophysical Observatory (SAO) were taken from the Standard Earth 1966 publication. This included Z for Goldstone, Woomera (DSS 41), and Johannesburg (DSS 51). Near the end of June 1969, new solutions were prepared at SAO by Lambeck (Ref. 8), which included DSS 42 and DSS 61 in addition to those above. DSS 62 was referenced from DSS 61 by using the survey deltas. Differences of 4 to 56 m exist between these new values and the old. When implemented in the DPODP for processing *Mariner* Mars 1969 doppler and range data, reductions of 40 m occurred in range biases. The orbits determined

by doppler data only were unaffected, but because of the declination of the 1969 probes, the Z component does affect the reduction of range data. Following this general confirmation of the quality of the new Z values, they were used in successive location sets provided to both orbit determination programs.

References

1. Hamilton, T. W., and Melbourne, W. G., "Information Content of a Single Pass of Doppler Data From a Distant Spacecraft," in *The Deep Space Network*, Space Programs Summary 37-39, Vol. III, pp. 18–23. Jet Propulsion Laboratory, Pasadena, Calif., May 31, 1966.
2. Hamilton, T. W., Grimes, D. C., and Trask, D. W., "Critical Parameters in Determining Navigational Accuracy for a Deep Space Probe During Planetary Encounter," in *The Deep Space Network*, Space Programs Summary 37-44, Vol. III, pp. 4–11. Jet Propulsion Laboratory, Pasadena, Calif., Mar. 31, 1967.
3. Van Flandern, Thomas C., "A Preliminary Report on a Lunar Latitude Fluctuation," in *Proceedings of the JPL Seminar on Uncertainties in the Lunar Ephemeris*, edited by J. Derral Mulholland, Technical Report 32-1247. Jet Propulsion Laboratory, Pasadena, Calif., May 1, 1968.
4. Warner, M. R., and Nead, M. W., *SPODP—Single Precision Orbit Determination Program*, Technical Memorandum 33-204. Jet Propulsion Laboratory, Pasadena, Calif., Feb. 15, 1965.
5. Mottinger, N. A., "DSS Location Solutions for Deep Space Probe Missions, Using *Mariner IV*, *Mariner V*, and *Pioneer VII* Data," in *The Deep Space Network*, Space Programs Summary 37-56, Vol. II, pp. 45–58. Jet Propulsion Laboratory, Pasadena, Calif., Mar. 31, 1969.
6. Mottinger, N. A., "Breaking the 10-Meter Level in Obtaining Consistent Station Location Solutions From the Reduction of Deep Space Probe Data," paper presented at the 50th annual meeting of the AGU.
7. Muller, P. M., and Chao, C. C., "New Timing Polynomial Program and Data," in *The Deep Space Network*, Space Programs Summary 37-57, Vol. II, pp. 42–51. Jet Propulsion Laboratory, Pasadena, Calif., May 31, 1969.
8. Muller, P. M., Anderson, J. D., and Vegos, C. J., "Equations and Program for the Combination of Statistical Estimates," in *The Deep Space Network*, Space Programs Summary 37-47, Vol. II, pp. 41–45. Jet Propulsion Laboratory, Pasadena, Calif., Sept. 30, 1967.
9. Mulholland, J. D., and Holdridge, D. B., "Application of a Transformation of Equinox in the Lunar Theory: Lunar Ephemeris No. 16," in *The Deep Space Network*, Space Programs Summary 37-57, Vol. II, pp. 51–53. Jet Propulsion Laboratory, Pasadena, Calif., May 31, 1969.

Appendix

Updating of DSN Station Locations for the Single Precision Orbit Determination Program

The following tables summarize the updating information on DSN station locations generated for use in the Single Precision Orbit Determination Program during the *Mariner* Mars 1969 mission.

Table A-1. Update for launch, LS 17 (longitude-biased for UT1 discontinuity)[a]

Deep Space Station	Pole position: $X = -2.2$ m, $-0.071''$; $Y = 11.2$ m, $0.362''$				
	RI, km	Latitude, deg	Longitude, deg	R_s, km	Z, km
DSS 11	6372.0061	35.208118	243.15071	5206.3319	3673.7679
DSS 12	6371.9904	35.118741	243.19464	5212.0435	3665.6329
DSS 14	6371.9891	35.244429	243.11060	5203.9887	3677.0569
DSS 41	6372.5534	−31.211440	136.88768	5450.1952	−3302.2430
DSS 42	6371.7003	−35.219559	148.98148	5205.3483	−3674.6311
DSS 51	6375.5290	−25.739504	27.685511	5742.9351	−2768.7663
DSS 61	6369.9899	40.238507	355.75120	4862.6086	4114.8279
DSS 62	6369.9924	40.263484	355.63240	4860.8163	4116.9489
DSS 72	6378.2386	−7.899908	345.67364	6317.7071	−876.6439

[a]Mottinger, N. A., and Sjogren, W. L., *Recommended Values of DSN Tracking System Parameters for Mariner Mars 1969: Premidcourse Activities*, JPL Internal Report, Apr. 1969.

Table A-2. Update for interim use to May 9 pole, LS 17 (longitude-biased for UT1 discontinuity)[a]

Deep Space Station	Pole position: $X = 2.2$ m, $0.071''$; $Y = 11.7$ m, $0.378''$				
	RI, km	Latitude, deg	Longitude, deg	R_s, km	Z, km
DSS 11	6372.0061	35.208104	243.15068	5206.3328	3673.7667
DSS 12	6371.9904	35.118727	243.19461	5212.0444	3665.6317
DSS 14	6371.9891	35.244415	243.11057	5203.9896	3677.0556
DSS 41	6372.5534	−31.211472	136.88767	5450.1933	−3302.2461
DSS 42	6371.7003	−35.219595	148.98147	5205.3459	−3674.6343
DSS 51	6375.5290	−25.739471	27.685501	5742.9367	−2768.7630
DSS 61	6369.9899	40.238546	355.75120	4862.6057	4114.8312
DSS 62	6369.9924	40.263524	355.63240	4860.8134	4116.9523
DSS 72	6378.2386	−7.899869	345.67364	6317.7077	−876.6396

[a]Mottinger, N. A., *Recommended Values of DSN Station Locations for Interim Use by Mariner Mars 1969*, JPL Internal Report, May 15, 1969.

Table A-3. Update to June 15 pole, LS 22 (longitude-biased for UT1 discontinuity)[a]

Deep Space Station	Pole position: X = 2.70 m, 0.087″; Y = 10.5 m, 0.340″				
	RI, km	Latitude, deg	Longitude, deg	R_s, km	Z, km
DSS 11	6372.0065	35.208090	243.15058	5206.3339	3673.7656
DSS 12	6371.9907	35.118713	243.19451	5212.0454	3665.6305
DSS 14	6371.9895	35.244401	243.11047	5203.9908	3677.0545
DSS 41	6372.5535	−31.211468	136.88757	5450.1936	−3302.2457
DSS 42	6371.7002	−35.219594	148.98135	5205.3459	−3674.6342
DSS 51	6375.5316	−25.739451	27.685394	5742.9399	−2768.7621
DSS 61	6369.9869	40.238574	355.75109	4862.6016	4114.8316
DSS 62	6369.9922	40.263529	355.63229	4860.8128	4116.9525

[a]Mottinger, N. A., and Sjogren, W. L., *New Values of DSN Station Locations for Use by Mariner Mars 1969 in SPODP*, JPL Internal Report, July 2, 1969.

Table A-4. Update to July 28 pole, LS 24 (no biasing required)[a]

Deep Space Station	Pole position: X = 4.1 m, 0.133″; X = 8.5 m, 0.275″				
	RI, km	Latitude, deg	Longitude, deg	R_s, km	Z, km
DSS 11	6372.0084	35.208100	243.15059	5206.3348	3673.7676
DSS 12	6371.9927	35.118724	243.19452	5212.0464	3665.6327
DSS 14	6371.9915	35.244410	243.11047	5203.9918	3677.0565
DSS 41	6372.5561	−31.211504	136.88756	5450.1938	−3302.2505
DSS 42	6371.7103	−35.219730	148.98133	5205.3455	−3674.6524
DSS 51	6375.5247	−25.739303	27.685400	5742.9409	−2768.7443
DSS 61	6370.0235	40.238966	355.75108	4862.6013	4114.8885
DSS 62	6369.9643	40.263259	355.63227	4860.8110	4116.9116

[a]Mottinger, N. A., and Sjogren, W. L., *Encounter Station Locations (July 28 pole) for Use by Mariner VI in the SPODP*, JPL Internal Report, July 25, 1969.

Table A-5. Update to June 25 pole, LS 24[a]

Deep Space Station	Pole position: X = 3.2 m, 0.103″; Y = 10.05 m, 0.325″				
	RI, km	Latitude, deg	Longitude, deg	R_s, km	Z, km
DSS 11	6372.0084	35.208117	243.15059	5206.3338	3673.7691
DSS 12	6371.9927	35.118740	243.19452	5212.0454	3665.6341
DSS 14	6371.9915	35.244427	243.11047	5203.9908	3677.0580
DSS 41	6372.5561	−31.211508	136.88757	5450.1936	−3302.2509
DSS 42	6371.7103	−35.219730	148.98134	5205.3455	−3674.6524
DSS 51	6375.5247	−25.739316	27.685396	5742.9402	−2768.7456
DSS 61	6370.0235	40.238959	355.75109	4862.6018	4114.8879
DSS 62	6369.9643	40.263252	355.63228	4860.8115	4116.9110

[a]Mottinger, N. A., and Sjogren, W. L., *New Values of DSN Station Locations (25 June Pole) for Use by Mariner Mars 1969 in SPODP*, JPL Internal Report, July 28, 1969.

Timing Errors and Polar Motion

P. M. Muller and C. C. Chao

I. Timing Errors

Three types of time are used when computing an orbit: ephemeris time (ET), used to look up positions of the celestial bodies; universal time (UT1), used to determine the location of a tracking station in space; and station time (t_s), the time tag that is associated with the actual tracking data (Ref. 1). The behavior of these times with respect to a uniform time is schematically illustrated in Fig. 1, where the abscissa is a uniform time defined for purposes of this discussion as atomic time (A.1), and the ordinate represents units in one of the above three time systems.

The lack of precise knowledge of the relationships among the three times illustrated in Fig. 1 can result in a degradation in the apparent quality of the tracking data, incorrect solutions for the tracking station locations, and an erroneous prediction of the spacecraft coordinates near planetary or lunar encounter. The latter two effects are related in the case of an error between t_s and UT1. Two limiting cases are illustrated in Fig. 2 for spacecraft tracked by a single station. In both instances, the orbit determination process is not aware of any error in the timing relationships.

For case 1 in Fig. 2, the orbit determination process assumes that the tracking station location is known perfectly and determines the orbit. This will cause the spacecraft trajectory to rotate in space such that for

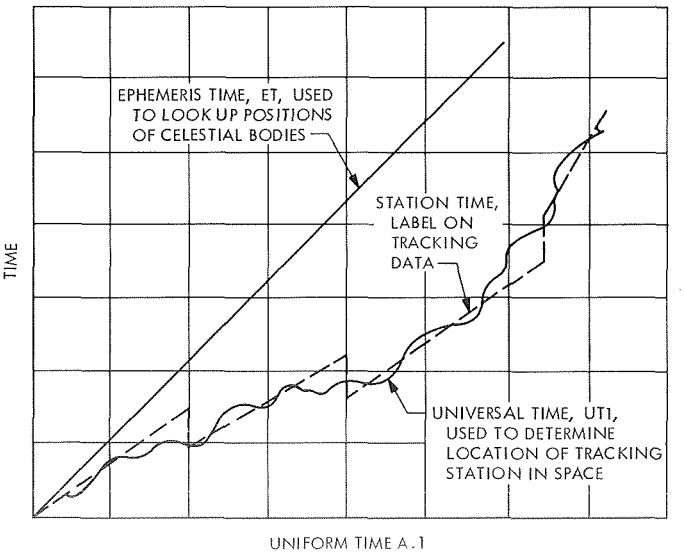

Fig. 1. Relationship of time systems in the orbit determination process

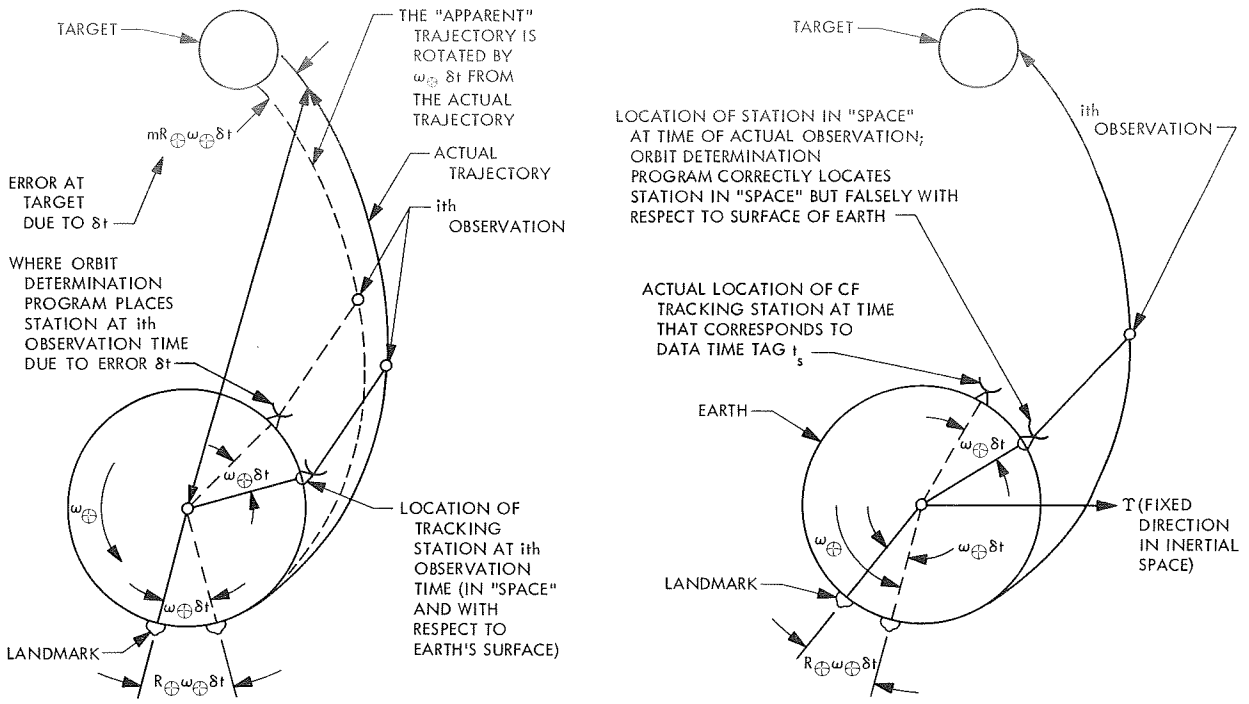

Fig. 2. Effect of an error (Δt_s) in UT1 − t_s

the *Mariner* Mars 1969 mission the coordinates near encounter will be in error by 6400 km (1 m $\oplus \approx$ 16 km Mars) for each second of error in UT1 − t_s. Midcourse maneuver preparations during a mission represent an example of this situation where only near-earth tracking data are available to determine the orbit and predict the trajectory near the target body.

If on the other hand it is assumed, as in case 2, that the orbit is perfectly known while solving for the longitude of the tracking station, the station will shift 400 m in longitude for each second of time error in the quantity UT1 − t_s. This situation is approximated during the cruise phase of a planetary mission after the spacecraft orbit has been "defined in space" due to the influence of the sun or similarily in a planetary flight as the spacecraft approaches the planet.

The preceding discussion does not differentiate between an error in UT1 or in t_s with respect to an "absolute reference time." In the case of an orbit program, this reference time is ET (or A.1). When processing data, the orbit determination program is basically dependent on the station tags. That is, the UT1 and ET corresponding to the time tag are associated with the data point. Therefore, an error in t_s − A.1 (or ideally, t_s − ET) differs from an A.1 − UT1 error in that the former causes a "shift" in the ephemeris bodies at the time the orbit determination program believes the data point to be taken. However, this effect is of secondary importance for the example considered here.

The error in range differences measured by the DSN stations in "space" is a function of the error δt in t_s − UT1 = (A.1 − UT1) − (A.1 − t_s). A "bias" in t_s − UT1 would show up in the orbit determination solutions as a shift in station longitude. This discussion will limit itself to the assumed unknown "daily" variation of t_s − UT1. The ability of the stations of synchronize themselves to the National Bureau of Standards UTC timing signal is a limiting factor until time synchronization by use of the ranging system is available. After that, the variations of A.1 − UT1 dominate.

II. Polar Motion Errors

The earth's principal axis is not coincident with the spin axis; it moves with respect to the latter, causing the so-called polar motion. The precision with which we are seeking to evaluate DSN stations requires consideration of this polar motion and its effects.

Polar motion, which is different from the earth's precession and nutation (Ref. 2), is observed indirectly through determinations of the variations in latitude of various observatories. If we take the nominal station location of any observatory or DSN station in earth-fixed system (EFS) coordinates (Ref. 3) and then observe its location in the instantaneous (INS) coordinates, there will be a difference. It is clear that such a coordinate difference is caused by polar motion. The following equations give the relations between the instantaneous north pole position and the INS − EFS coordinate differences for latitude, longitude, and r_s:

$$\Delta\lambda = \lambda_{INS} - \lambda_{EFS} = \tan\phi\,(X\sin\lambda - Y\cos\lambda) \qquad (1)$$

$$\Delta\phi = \phi_{INS} - \phi_{EFS} = X\cos\lambda - Y\sin\lambda \qquad (2)$$

$$\Delta r_s = -\Delta\phi\sin\phi \qquad (3)$$

where X, Y are polar coordinates; ϕ, λ are station latitude and longitude; and r_s is the distance from earth's spin axis to a station or observatory.

Figure 3 plots the path of the north pole for the period 1959 to 1962. The X-Y plane is tangent to the north pole with the x axis along the Greenwich meridian. It is seen that the pole completes a revolution for 1.1 to 1.2 years with an amplitude ranging from 5 to 20 m. Such an appreciable motion will obviously cause variations in DSN station location with the same order of magnitude of the polar motion. As an example, Fig. 4 shows the station location variations at the Goldstone DSCC for the period 1960 to 1966. The deviation of 10 m seen in the figure is typical. The maximum, however, ranges up to 23.5 m for some station pairs. Besides, polar motion has a correlation with timing, since UT1 is, by definition, obtained from observed data (UT0) after polar motion correction. The relation between UT1 and UT0 is given as

$$UT1 = UT0 + \frac{\tan\phi\,(X\sin\lambda - Y\cos\lambda)}{15} \qquad (4)$$

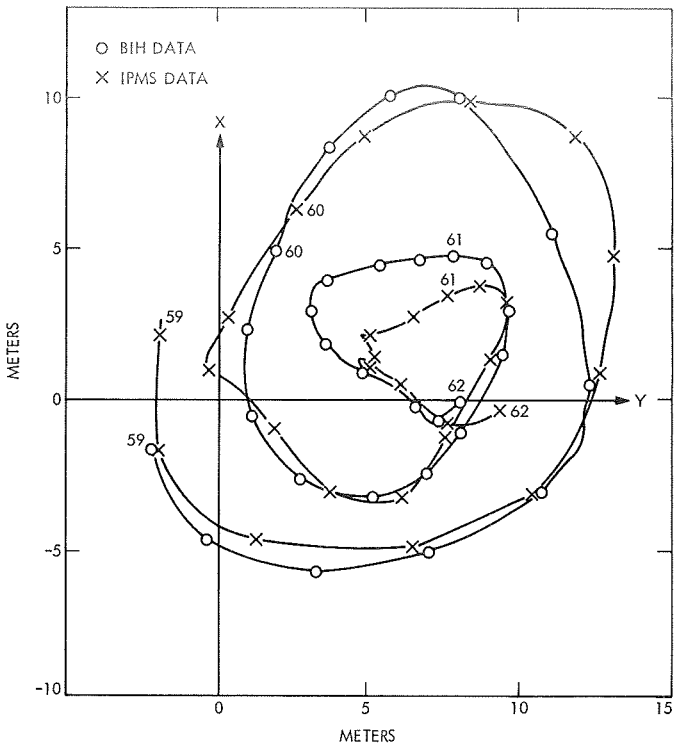

Fig. 3. Path of the North Pole for the period 1959 to 1962

III. Procedures for Implementing Corrections to the Data

A. Timing

1. Selection of data source. Currently, the quantity A.1 − UT1 is determined by many agencies and observatories. The quality of A.1 − UT1 varies from observatory to observatory, depending on their instruments and the local weather conditions throughout the year. Among them, only two agencies were considered for our use because of their relative excellence in the observed data. They are the U. S. Naval Observatory (USNO), and the Bureau International de l'Heure (BIH). The USNO, which has been in close contact with JPL in supplying data for earlier missions, has two stations, one at Washington, D. C., and one at Richmond, Florida. Both stations use PZT (photographic zenith tube) to do the time measurement. An appreciable difference between the smoothed value of A.1 − UT1 of the two stations has been found, and the USNO-adopted A.1 − UT1 is the linear combination of the two results by weighting Richmond 2 and Washington 1 (i.e., USNO A.1 − UT1 = 2/3 Richmond (A.1 − UT1) + 1/3 Washington

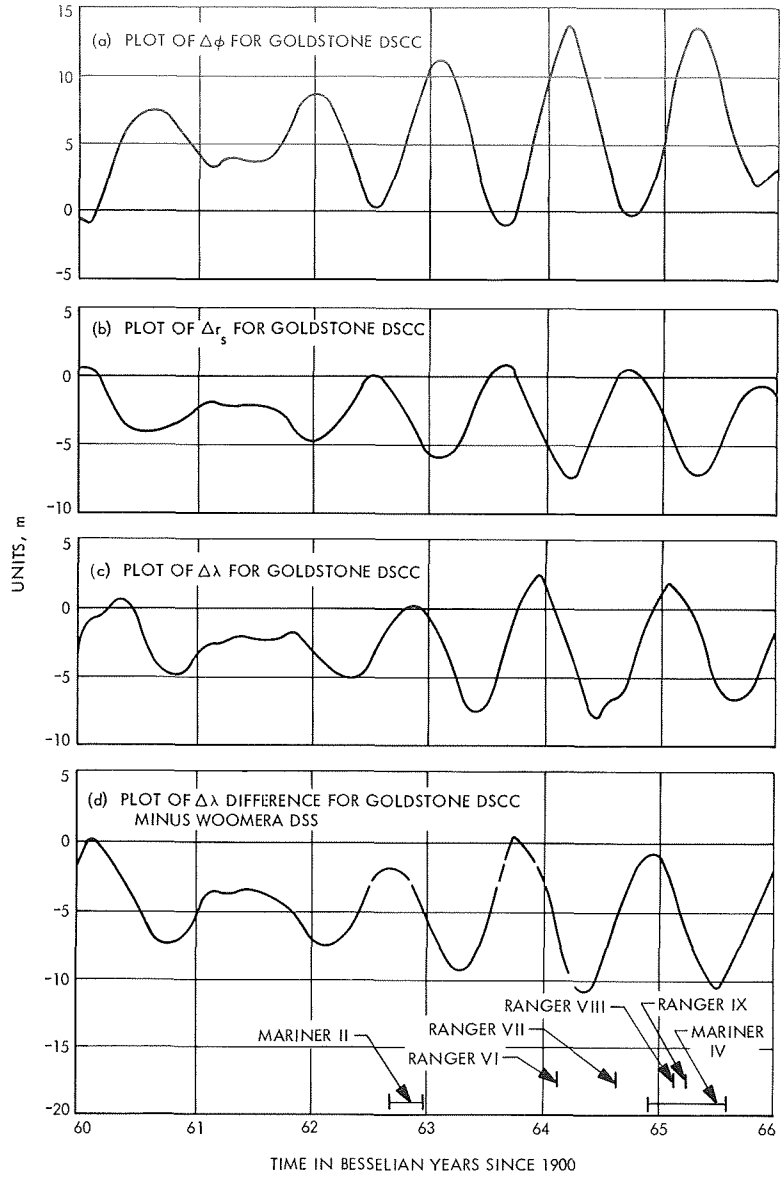

Fig. 4. Station location variations caused by polar motion, 1960 to 1966

(A.1 − UT1)). The relative weighting of the two stations has no theoretical or experimental justification. It was adopted because previous experience has shown Richmond to have more observations and better results than Washington. Thus, the USNO-adopted A.1 − UT1 may tend to have a bias toward one station's result when the other station has no observations because of bad weather. Therefore, when we use the USNO data, we use the result from one station (Richmond) all the time.

The BIH-adopted A.1 − UT1 results from combined UT observation of over 40 stations around the world, including Washington and Richmond. A very sophisticated computing program (Ref. 4) is employed by the BIH to solve for A.1 − UT1. As claimed by BIH, their results are superior than those of USNO. The claimed uncertainty of A.1 − UT1 from these sources is shown in Table 1. The estimated uncertainties in Table 1 clearly suggest that we should use BIH-adopted A.1 − UT1. However, after a practical test with the previous mission results, Richmond A.1 − UT1 (smoothed by JPL) turned out to be more consistent with the mission data than the BIH-adopted value. This implied that a long-term difference between the two data sources might exist.

Table 1. Claimed short-term A.1 − UT1 uncertainties

Time when A.1 − UT1 was determined	USNO		BIH	
	One sigma, ms	Worst case, ms	One sigma, ms	Worst case, ms
One night	6	30	Not applicable	Not applicable
1 year later; final smoothed data	5	25 (between Washington and Richmond)	2	?

Finally, we decided that it is wise to stay with a single station that produces consistent results. Thus the nightly observed A.1 − UT1 from Richmond was the source of timing data for the *Mariner* Mars 1969 mission.

2. Procedures of processing the data. A monthly recap of a daily report of observed raw data of A.1 − UT1 of Richmond together with that of Washington was received from USNO on keypunched cards around the 15th of each month. The JPL Timing Polynomial Computer Program (TPOLY) computes quadratic polynomials (first derivative continuous at the monthly breakpoints) for the received A.1 − UT1 data by employing a least-squares fitting technique (Ref. 5). In the meantime, TPOLY also generates the required prediction of A.1 − UT1 for the mission. The output of TPOLY, which is the fitted value of Richmond A.1 − UT1 and the predicted values, becomes the JPL-adopted A.1 − UT1. They are delivered to SPODP and DPODP for orbit determination via punched cards containing polynomials.

During the encounter period of *Mariner VI* and *VII* ($E - 30$ to $E + 6$ days), a special arrangement was made to receive the up-to-date data from USNO daily by teletype and/or telephone. This was to eliminate unnecessary error accumulated in the predicted A.1 − UT1 to obtain better navigational accuracy during encounter.

B. Polar Motion

1. Selection of data source. The polar motion is measured independently by two organizations. They are the International Polar Motion Service (IPMS) (Ref. 6) and the Bureau International de l'Heure (BIH) (Ref. 4). IPMS utilizes measurements taken from five observatories, which are at the same latitude and share the same star catalog. BIH determines the polar motion by averaging the results from over 25 stations with distinct latitudes and catalogs. In solving for the polar coordinates X and Y, BIH solves Eqs. (1) and (2) simultaneously. IPMS solves Eq. (2) alone.

Figure 3 shows the comparison between the data from the two organizations in the period 1959 to 1962. According to the data from 1956 to present, they differed by 3 m in the worst case and 1½ m on the average.

Recently, as a research effort, the IPMS also computed the polar motion using the results from 26 of their stations (including the 5 original stations) from 1962 to 1968. Figure 5 shows the variations of the polar coordinates X, Y from BIH results and the research results of 26 IPMS stations. It clearly indicates that the BIH results are in better consistency with the IPMS 26-station results than with the IPMS 5-station results. It is probable, as pointed out by Yumi of IPMS (Ref. 6), that the polar coordinates from only a few stations (5) are apt to be affected strongly by a local error of a certain station. This implies that the results from BIH, which uses more than 25 stations to compute the polar path, are superior to those of the 5 IPMS stations.

Therefore we chose the published results from BIH as JPL-adopted polar motion data. Washington and Richmond UT1 is determined from UT0 via the BIH pole for consistency.

According to B. Guinot of BIH*, the probable error on their published X and Y of polar motion is $\pm 0''.01$ (or ⅓ meter), which is the accidental error. But periodic systematic error may exist, because of the errors of the declinations of stars as a function of right ascension α, or to some seasonal changes in the zenithal refraction. There is no way to have a precise estimation of this systematic error, except by using many stations sharing the same star catalog. The total amplitude, as Guinot believed, does not exceed $0''.02$.

2. Procedures of processing data. Together with raw data of A.1 − UT1, the BIH polar motion data were received from USNO on the same keypunched cards every month. TPOLY computes linear polynomials for the BIH polar motion data (X and Y). Although the BIH publishes final, as well as predicted polar motion data, we only use the final data and do our own prediction with the circular arc prediction model in TPOLY (Ref. 5).

*Personal communication.

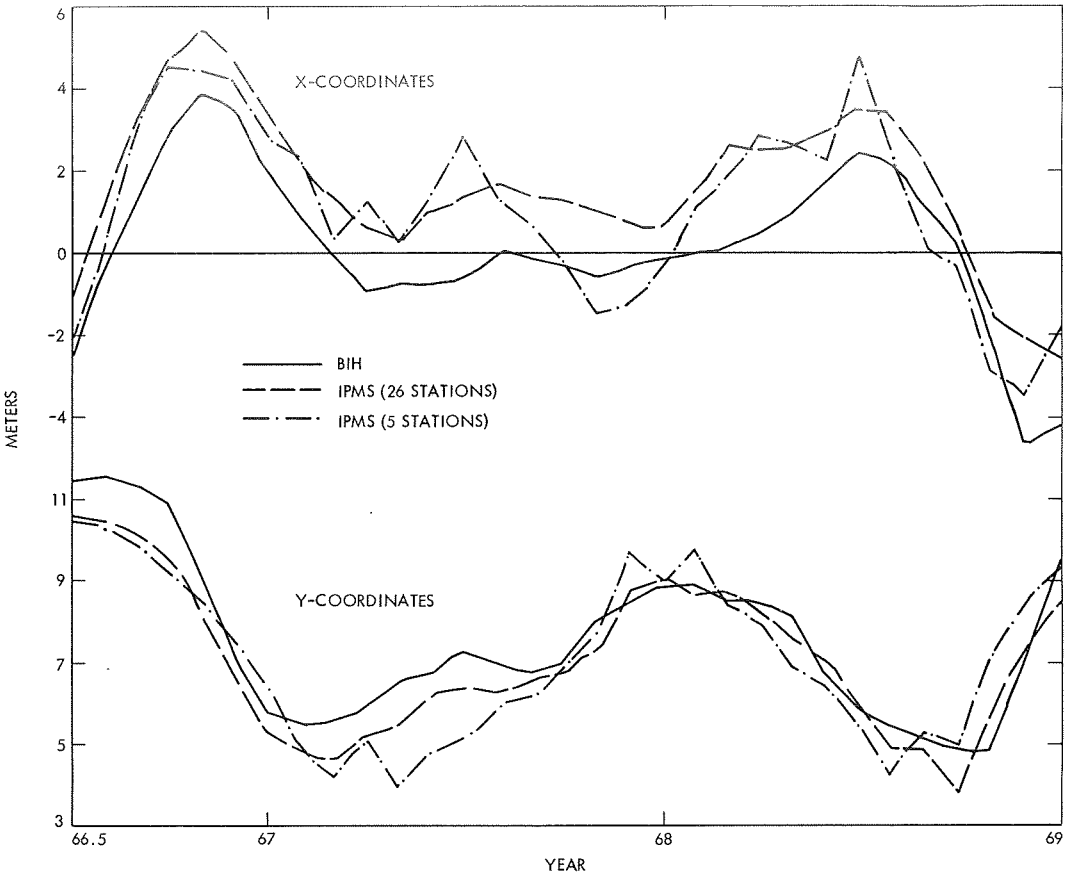

Fig. 5. Comparison of polar motion coordinates between BIH and IPMS

This is done because the BIH data always has a discontinuity between their final and predicted data.

Since the BIH requires one month to prepare their final polar motion data, the prediction of polar motion for supplying up-to-date data becomes as important as that of A.1 − UT1. A possible correlation between earthquakes and polar motion was investigated (Ref. 7) to search for a model to predict polar motion. Unfortunately, the possible correlation discovered was of no help in predicting the polar motion. An empirical method—the circular arc extrapolation—was employed to do the prediction. The JPL-predicted polar motion data are expected to be good to ½ m within one-month prediction, provided that the pole moves along its regular circular (relatively well-behaved) path. However, within one-month prediction, the maximum deviation from final data should not exceed 1 m.

During the encounter period, a special computer run was made at BIH to supply us with the final (last date on July 7) polar motion data on July 29 (E − 2 of *Mariner VI*). This reduced the prediction length at encounter from 2 months to 25 days.

IV. Perturbation in JPL-Adopted Timing Data

It was found, as expected, that the JPL-adopted A.1 − UT1 data are perturbed each time newly received data are used for TPOLY input (Ref. 5). This is because the least-squares fitting curve will alter its path to fit the new data points. An analysis was made on such perturbation from launch to encounter of *Mariner VI* and *VII* (Ref. 8). The greatest magnitude of the perturbation reached 14 ms, which is twice as great as the uncertainty allowed by mission requirements, and the perturbation penetrated backward (at a lesser amplitude) two to three weeks from the last data point. Figure 6 shows the variations of the perturbed A.1 − UT1, obtained by subtracting the values of A.1 − UT1 given by a TPOLY run made on X day from the corresponding results of the next TPOLY run (made on Y day). For instance, let us look at curve C in Fig. 6, which represents the difference between the results of the two TPOLY runs made on

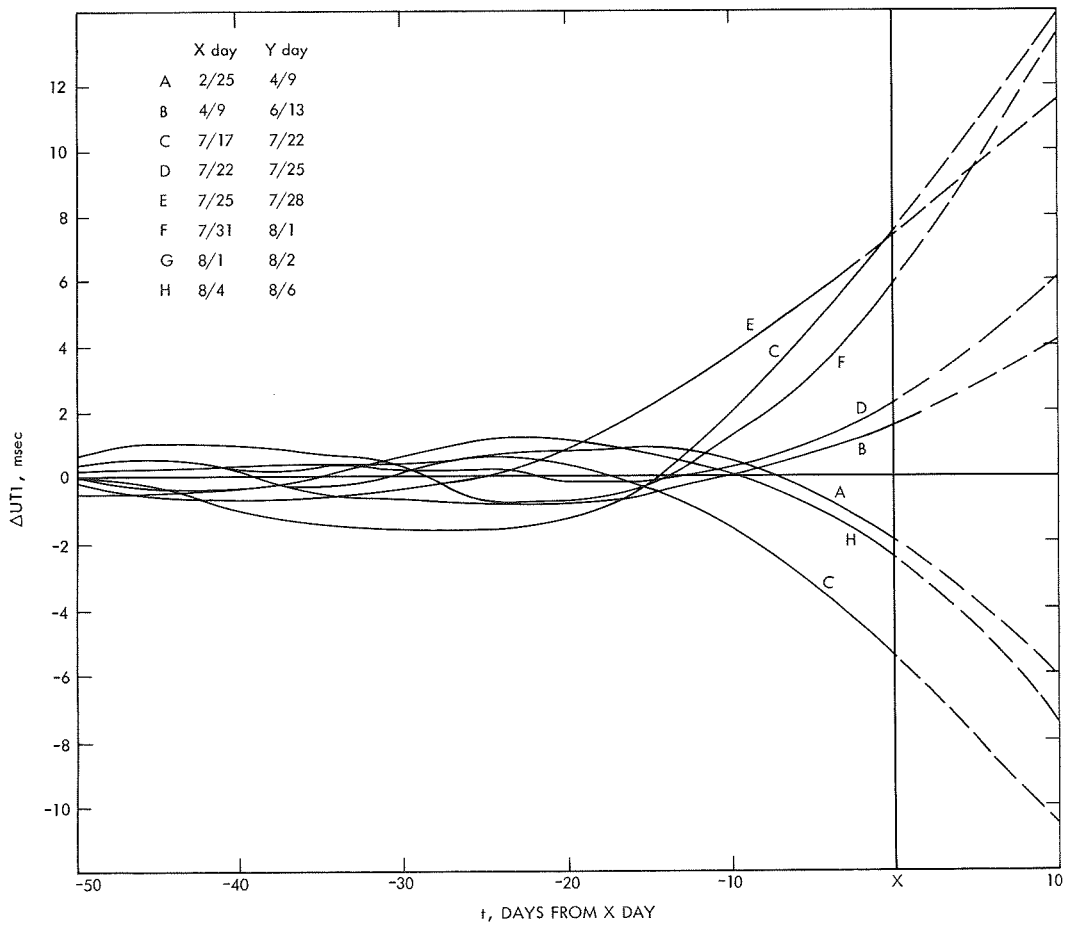

Fig. 6. Perturbation in JPL-adopted A.1 — UT1 due to new input data

July 17 and July 22. For a particular date, say July 7, the difference (relative perturbation) in A.1 − UT1 between the two TPOLY runs is found to be 2 ms (the value of curve C on X − 10 day). In other words, the JPL-adopted final A.1 − UT1 on July 7, which ideally should not change with time, decreased by 2 ms, when a later TPOLY run was made on July 22.

As can be seen, the perturbations in JPL-adopted *final* A.1 − UT1, which start from X day (X = July 17 for curve C), converge to within ±1 ms after one month backward from X day. The biggest value of these relative perturbations is found to be 7.5 ms on July 17. The portion of those curves after X day, which represent the difference between JPL *final* A.1 − UT1 of Y day TPOLY output and JPL *predicted* A.1 − UT1 of X day output, is actually the accuracy of prediction and cannot be considered as perturbation. Therefore, the conclusion can be reached that the JPL final A.1 − UT1 values will remain unchanged when they pass through the perturbation region; i.e., when they are about 30 days away from the last final data point.

Figure 7 shows the true perturbations of A.1 − UT1, the perturbations with respect to a fixed reference (the results of TPOLY made on September 4, one month after encounter). The greatest perturbation, which occurred two weeks before encounter, reached 14 ms, twice as high as the required accuracy. On that day the 5-day and 10-day predictions deviated from the true values by 21 and 30 ms, respectively.

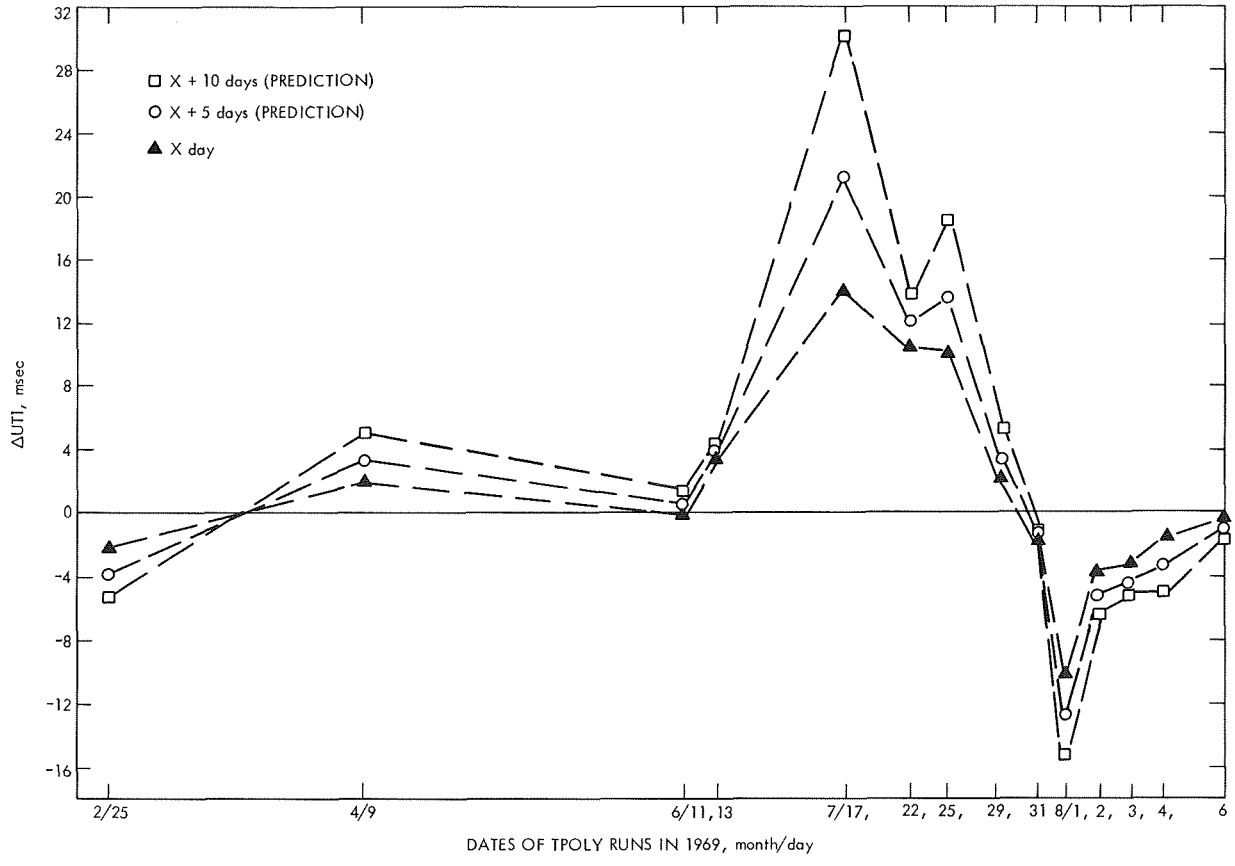

Fig. 7. Variation of A.1 − UT1 perturbations on X days with respect to TPOLY results on September 4, 1969

References

1. Trask, D. W., and Muller, P. M., "Timing: DSIF Two-Way Doppler Inherent Accuracy Limitations," in *The Deep Space Network*, Space Programs Summary 37-39, Vol. II, pp. 7–16. Jet Propulsion Laboratory, Pasadena, Calif., May 31, 1966.

2. *Explanatory Supplement to the Ephemeris*, pp. 26–44. Her Majesty's Stationery Office, London, 1961.

3. Muller, P. M., "Polar Motion and DSN Station Locations," in *The Deep Space Network*, Space Programs Summary 37-45, Vol. III, pp. 10–14. Jet Propulsion Laboratory, Pasadena, Calif., May 31, 1967.

4. Guinot, B., and Feissel, M., *BIH Annual Report for 1968.*

5. Muller, P. M., and Chao, C. C., "New Timing Polynomial Program and Data," in *The Deep Space Network*, Space Programs Summary 37-57, Vol. II, pp. 42–51. Jet Propulsion Laboratory, Pasadena, Calif., May 31, 1969.

6. Yumi, A., *Annual Report of the IPMS.*

7. Chao, C. C., and Muller, P. M., "A Study of Polar Motion and Earthquakes for the Period 1904–1966," in *The Deep Space Network*, Space Programs Summary 37-56, Vol. II, pp. 69–74. Jet Propulsion Laboratory, Pasadena, Calif., Mar. 31, 1969.

8. Chao, C. C., "Perturbation in JPL-Adopted Time Data Due to Newly Input Raw Data," in *The Deep Space Network*, Space Programs Summary 37-59, Vol. II, pp. 110–114. Jet Propulsion Laboratory, Pasadena, Calif., Sept. 30, 1969.

The Ionosphere

B. D. Mulhall, V. J. Ondrasik, and K. L. Thuleen

I. Charged-Particle Effect on Radio Signals

The charged particles in the ionosphere and the interplanetary space plasma along the ray path of the radio signal transmitted to and received from a spacecraft have various effects upon the signal. Among these effects are absorption, refraction, scintillation, polarization rotation, phase path-length decrease, and group path delay. For orbit determination, the two effects of concern are phase path decrease and group path delay.

Reference 1 describes the effect of a plasma on radio-wave phase and group paths. Briefly, the plasma delays the propagation of the energy in the wave. This effect is called group path delay. The phase of the wave propagates at a faster rate. This increase in phase velocity, or decrease in phase path, is a function of the wave frequency and so the plasma has a dispersive effect on the spectrum of the radio signal.

As the number of charged particles along the ray path changes, the phase path changes and shifts the S-band carrier frequency. This frequency shift cannot be distinguished from the doppler effect unless the change in the number of charged particles is determined. Similarly, the charged particles delay the energy of the S-band signal, a result that increases the round-trip time (the group path length) and corrupts range data, since these measurements are based on the time required for the energy to propagate from the tracking station to the spacecraft and return.

II. Charged-Particle Effect on Interplanetary Navigation

In a preceding article,[1] an explanation is given of the method for converting a doppler error into equivalent station location errors by employing the Hamilton–Melbourne model of the information content of doppler data (Ref. 2). This technique is used extensively to describe the ionospheric effect on navigation in the following discussion.

[1] "Tracking System Analytic Calibration Description," by D. W. Trask and B. D. Mulhall.

The ionosphere causes two types of navigational errors: random and systemic. Random errors in the doppler observable can be reduced by taking data over many passes. Systematic errors cannot be reduced by averaging. If the systematic error is essentially constant over each pass, it will corrupt the estimate of geocentric range rate, the a parameter of the Hamilton–Melbourne model, rather than station location. However, if the error is a time-varying function with a diurnal period, then estimates of station spin radius r_s will be corrupted by antisymmetric (odd) errors, and station longitude λ by symmetric (even) errors.

The earth's ionosphere is caused by ultraviolet light from the sun ionizing the upper atmosphere. Consequently, the density of charged particles in the ionosphere increases and decreases with a diurnal period. For post-flight analysis,[2] the diurnal variation of the ionosphere will corrupt the station location estimates. For in-flight orbit determination, the ionospheric effect will corrupt the estimate of the probes orbit.

The tracking data from the *Mariner IV* and *V* missions have been calibrated for ionospheric effect. The *Mariner IV* spacecraft flew by the planet Mars in July 1965. That year was a period of very low solar activity and, consequently, concentrations of charged particles in the earth's ionosphere were low. The ionospheric calibration for *Mariner IV* caused a change of about 1 m in the estimate of station location, both in distance from the earth's spin axis (spin radius) r_s and longitude λ.

Mariner V flew during 1967, a period of much higher solar activity. The ionospheric calibration for this mission resulted in changes of about 6 m in both spin radius and longitude. The day-by-day effect of the ionosphere on station location for this mission is shown in Fig. 1. From this graph it is apparent that errors greater than 10 m occurred on single days.

It was anticipated that solar activity in 1969 would be as great as in 1967; therefore, the *Mariner* Mars 1969 navigational accuracy goal of 1.5 m in spin radius and 3 m in longitude dictated that ionospheric calibration be performed. The 6- to 10-m errors in spin radius and longitude caused by the ionosphere in 1967 could have resulted in errors (1σ) of 170 to 255 km in spacecraft declination and right ascension for *Mariner* Mars 1969 at encounter.

[2]See discussion in "Station Locations," by N. Mottinger and W. L. Sjogren.

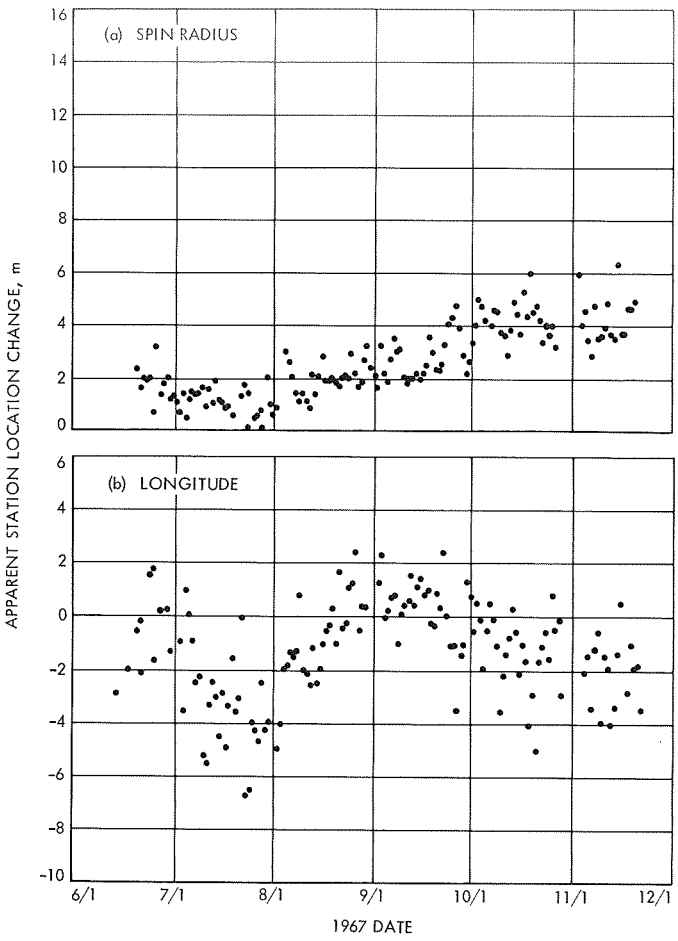

Fig. 1. Ionospheric effect on station location—*Mariner V*

III. Methods for Measuring and Estimating Charged Particles

There are many techniques for measuring charged particles in the earth's ionosphere and interplanetary space. Four techniques that have been studied as part of the TSAC effort are:

(1) Dual frequency.

(2) Group velocity vs phase velocity.

(3) Faraday rotation.

(4) Vertical soundings, ionosonde.

These techniques are discussed in the following paragraphs.

A. Dual-Frequency Measurements

The ray path length change due to interaction of a radio signal with charged particles is frequency dependent

(Ref. 3) and is expressed as

$$\pm\Delta l = \frac{k}{f^2}\int_{\text{path}} N(s)\,ds \qquad (1)$$

where

Δl = the change in path length, positive for group path and negative for phase path, m

k = 40.3 in mks units

f = signal frequency, Hz

$N(s)$ = local density of electrons along the ray path, electrons/m^3

ds = increment of path length, m

Consequently, when two signals at different frequencies are transmitted coherently through a medium they will lose coherency. The shift in phase of one signal with respect to the other is a measure of the integrated charged-particle content, expressed as

$$E_c = \int_{\text{path}} N(s)\,ds$$

along the path.

Dual-frequency experiments have been performed with the *Mariner V* spacecraft and many of the *Pioneer* series. When these data have been reduced they can be used to calibrate the tracking data for these missions. The two *Mariner* Mars 1969 spacecraft do not carry dual-frequency experiments, so other measurement sources are required.

B. Group Velocity vs Phase Velocity

Equation (1) provides a second means for measuring total electron content E_c along the ray path. Since the path-length change has opposite signs for phase and group path lengths, variations in E_c can be deduced if the variations in both the phase and group path lengths can be measured. A turn-around ranging system, such as those carried by *Mariners VI* and *VII*, provides a measure of the group path length between the tracking station and the spacecraft. The doppler measurement made on the spacecraft S-band carrier is affected by changes in E_c. From a comparison of integrated doppler with differenced range measurements, the time rate of change of E_c can be determined, and from dE_c/dt, a doppler calibration can be computed. In Ref. 4, MacDoran and Wimberly discuss the experiment being performed to determine the effectiveness of this method in actual operation. However, even if this method is successful, ranging at planetary distances can be performed only from the Mars DSS at the Goldstone Complex so that other methods must be found for calibration at the overseas stations.

C. Faraday Rotation

The plane of polarization of a radio signal passing through a charged-particle medium in the presence of a magnetic field is rotated by the Faraday effect. If the radio wave is linearly polarized and the initial polarization is constant with respect to some known frame of reference, then the polarization of the received signal can be used to measure the combined effect of the number of charged particles and the strength of the magnetic field encounter along the ray path (Ref. 3) according to

$$\Omega = \frac{R}{f^2}\int_{\text{path}} ||\mathbf{H}||\cos\theta N(s)\,ds \qquad (2)$$

where

Ω = Faraday rotation of the plane of polarization, rad

θ = angle between the signal wave normal and $\mathbf{H}$, the magnetic field vector

$||\mathbf{H}||\cos\theta$ = tangential component of the magnetic field along the ray path, A-turns/m

$R = 2.97 \times 10^{-2}$ in mks units

By computing the tangential component of the earth's magnetic field along the ray path, we can find

$$E_c = \int_{\text{path}} N(s)\,ds$$

For convenience, $||\mathbf{H}||\cos\theta$ is computed for one point along the path through the ionosphere, which simplifies Eq. (2) to the form

$$\Omega = \frac{R}{f^2}\,(||\mathbf{H}||\cos\theta)_{\text{ref}}\int_{\text{path}} N(s)\,ds \qquad (3)$$

The approximation made in Eq. (3) is being evaluated and will be the subject of a subsequent report. Preliminary

results indicate that for the range of interest of the ionospheric calibration effort, the approximation will be sufficiently accurate.

Unfortunately, both the high- and low-gain antennas on the *Mariner* Mars 1969 spacecraft are circularly polarized, which prevents measurement of the Faraday rotation effect. However, there are several geostationary satellites transmitting beacons that are linearly polarized. A receiver–polarimeter has been installed at the Venus DSS to provide measurements of the ionosphere to calibrate tracking data received at Goldstone.

D. Ionosonde

Before the advent of artificial satellites, the only method of measuring the ionosphere was vertical sounding called *ionosonde*. A radio signal is transmitted vertically, reflected by the ionosphere, and received by the transmitting station. This process is repeated while increasing the transmitted frequency until the signal pierces the ionosphere. The density of electrons required to reflect a particular frequency is (Ref. 1)

$$N = Af^2 \tag{4}$$

where

$A = 1.24 \times 10^{-2}$ electrons/m^3-Hz^2

N = density of electrons, electrons/m^3

f = reflected frequency, Hz

By measuring the time of flight for each reflected frequency, we can determine $N(h)$, the altitude dependence of the electron density. This method measures $N(h)$ for the lower or bottom side of the ionosphere, that is, up to the F_2 layer. The topside, above the F_2 layer, must be estimated by employing a model for $N(h)$ in this region.

Comparisons of total electron content computed from ionosonde data vs E_c measured by Faraday rotation indicate that total content can be estimated with usable accuracy from vertical soundings. As shown by comparison of Faraday rotation measurements made by Stanford (mapped to the Point Arguello zenith) with Point Arguello ionosonde data (Figs. 2 and 3), E_c computed by the Environmental Sciences Service Administration (ESSA) from ionosonde data is in better agreement with Faraday rotation measurements for quiet ionospheres, such as July 1965 (Fig. 2), than for active ionospheres, such as October 1967 (Fig. 3). Note also that the nighttime estimates are very accurate. The comparison seems poorest during the morning, probably because the sunlight initiates ionization more rapidly above the F_2 layer, the region the ionosonde does not measure.

E. Estimation Based on f_{0F_2} Data

Measurements of the peak frequency reflected, f_{0F_2}, and calculated values of total content for DSN stations in South Africa, Spain, and Australia were provided during the *Mariner* Mars 1969 encounter. The f_{0F_2} data for the entire pass with one total content for the pass were available in near-real time. The value for total electron content E_c for the entire pass was delayed until the additional computation could be performed. To estimate the ionosphere before the receipt of E_c for the entire pass, the following procedure was used.

As shown by Eq. (4), the maximum electron density can be found from the f_{0F_2} data. The Chapman model for the altitude dependence of the ionosphere is

$$N(h) = N_{\max}\, e^{\left[(1-u-e^{-u})/2\right]} \tag{5}$$

where

$N(h)$ = local density of the ionosphere, electrons/m^3

$N_{\max}$ = maximum electron density, electrons/m^3

$u = \dfrac{(h - h_{\max})}{B}$

h = altitude, km

$h_{\max}$ = altitude of the maximum density $N_{\max}$, km

B = scale height, km

To find total content from $N(h)$ we integrate

$$E_c = \int_0^\infty N(h)\, dh$$

$$E_c \sim BN_{\max} \int_{-\infty}^{\infty} e^{1/2(1-u-e^{-u})}\, du$$

Since $N(0) < 10^{-9}$, the lower limit of integration can be taken as $-\infty$. By substituting $x = e^{-u/2}$, we find

$$\left.\begin{aligned} E_c &= BN_{\max}\, e^{1/2} \int_{-\infty}^{\infty} e^{-(x^2/2)}\, dx \\ &= BN_{\max} \sqrt{2\pi e} \end{aligned}\right\} \tag{6}$$

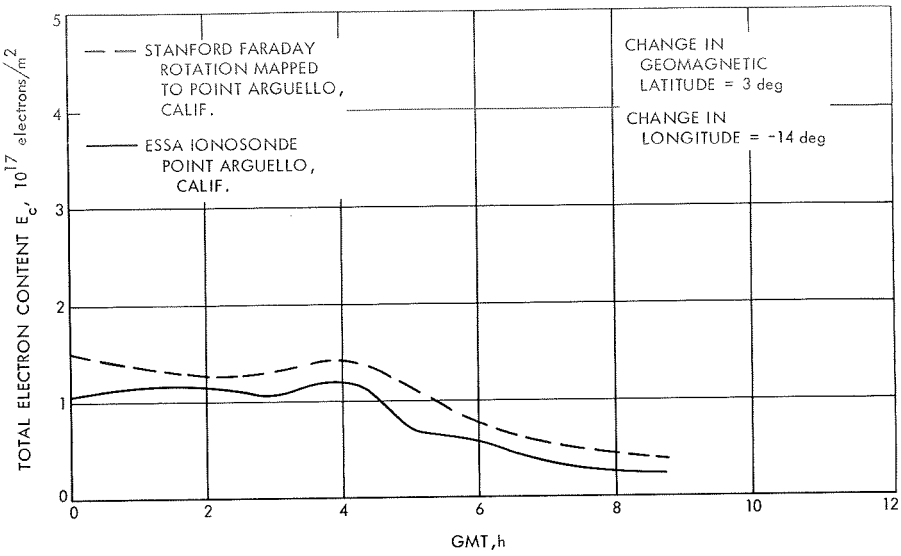

Fig. 2. Comparison of ionospheric measurements, July 1965

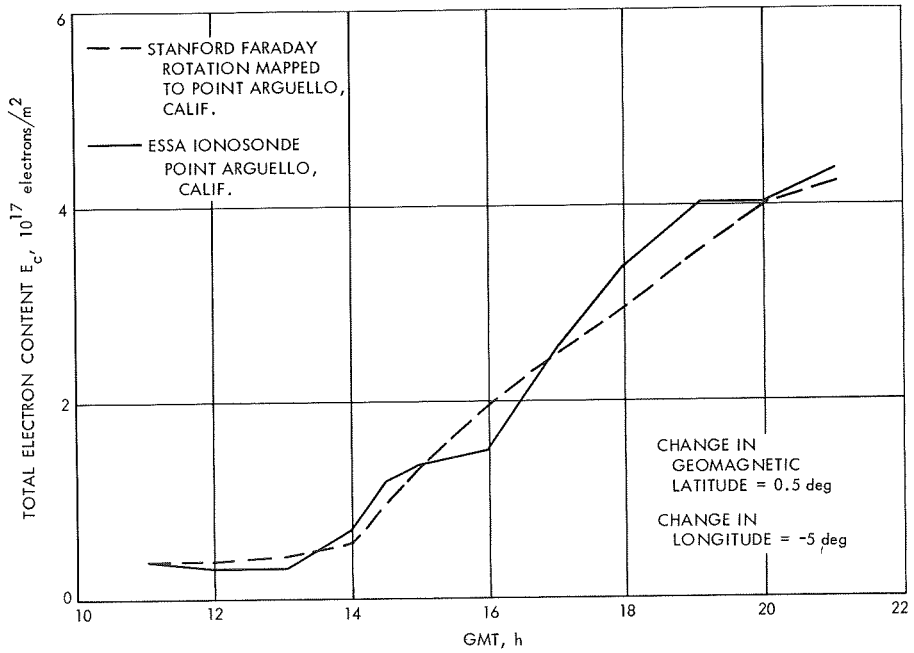

Fig. 3. Comparison of ionospheric measurements, Oct. 1967

Thus if E_c and f_{0F_2} are known, B can be calculated directly.

The maximum electron density is probably the most easily obtained of any ionospheric quantity, since it is proportional to the square of the f_{0F_2}, or critical, frequency, as shown in Eq. (4). A good estimate of the f_{0F_2} frequency may be obtained at the ionosonde station itself and may be made available in near-real time. Thus, the only missing factor in calculating the total electron content from Eq. (6) is a determination of the scale height

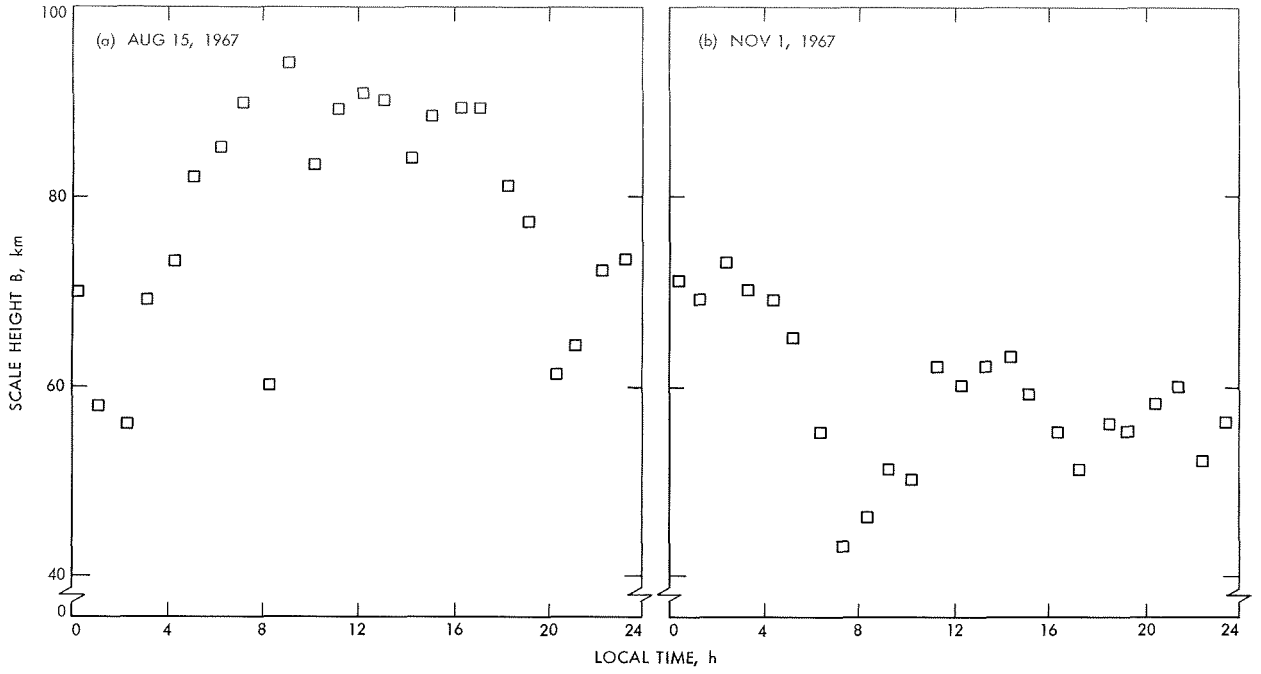

Fig. 4. Diurnal variation of scale height: (a) atypical day; (b) typical day

B. Unfortunately, a determination of B is almost as difficult to make as the determination of the total content itself. However, this is not a mortal blow to the computation of the total electron content from Eq. (6), because the behavior of B is fairly predictable.

Figure 4 shows the hourly variations of B as computed from Eq. (6), with Stanford Faraday rotation and Point Arguello f_{0F_2} measurements for August 15 and November 1, 1967. The fairly constant behavior of B (remaining within $\pm 25\%$ of the average) is true almost without exception for every day of the year.

1. Constant B method of determining total electron content. An approximate method for determining E_c is to hold B constant throughout the day. The actual noontime value of B for the day, as determined from Eq. (6), is used. The results shown for August 15 and November 1, 1967, in Fig. 5, in comparison with Stanford Faraday rotation measurements. The comparison between the constant B and Faraday rotation total content values is reasonably good on November 1, which is representative of most of the days in the year, particularly for the fall, winter, and spring. This same comparison on August 15 is not as satisfactory. However, this day was chosen to characterize one of the bad summer days and was not of much concern, since the *Mariner* Mars 1969 encounters occurred during the winter in the southern hemisphere.

2. Modified constant B method of obtaining total electron content. The constant B method of obtaining the total electron content may be improved by noting that the largest deviations from the Faraday rotation values occur at the rise and fall of the peak where the values of B are depressed. Operationally it is much easier to overcome this defect, not by modifying B, but by plotting the values of f_{0F_2} and modifying them so that certain rules will be satisfied.

These rules were developed by examining Stanford Faraday rotation measurements for 312 days in 1967. This examination showed that usually ($\sim 80\%$ of the time) the total electron content as a function of the time of day has a grossly similar pattern. For these normal days the total electron content follows the rules listed below, with exceptions occurring as noted:

(1) At about 20 min before sunrise, E_c starts to rise rather steeply from a fairly constant nighttime level. (There were five days when this did not occur.)

(2) The value of E_c continues to rise in a generally monotonic fashion until a fairly rounded top is reached, with the maximum value occurring between 11:00 and 15:00. Violations were as follows:

   (a) Maximum occurred 11 times before 11:00 or after 15:00.

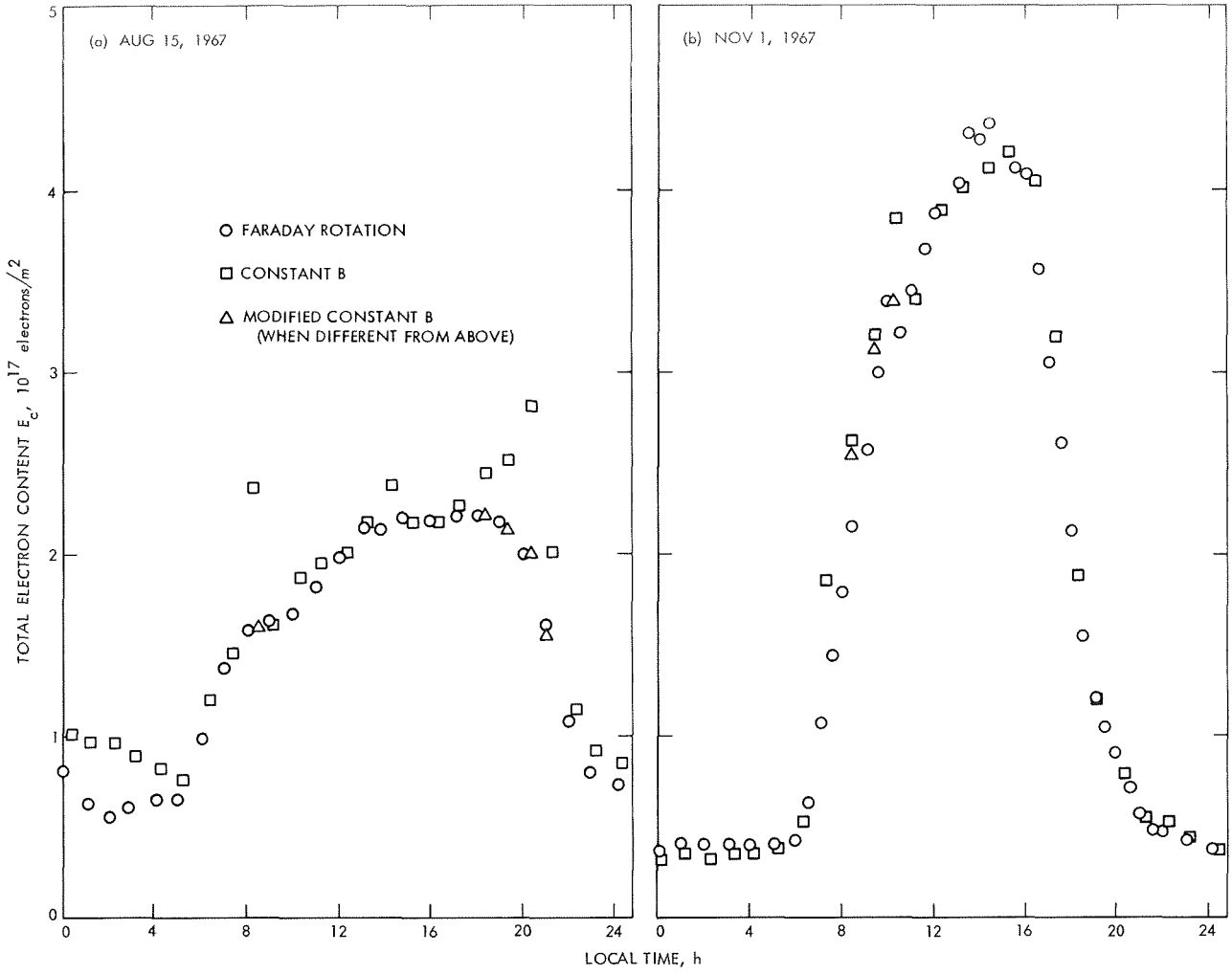

Fig. 5. Estimation of total electron content: (a) atypical day; (b) typical day

(b) Pointed or distorted peaks occurred 15 times.

(c) Double peaks occurred 4 times.

(3) The maximum value of E_c was at least 3 times the minimum value. (There were 6 days when this did not occur.)

(4) After the peak has been reached, E_c usually starts to descend rather slowly and is down to a nighttime level shortly after sunset. (During the summer months the peak often continued until the early morning hours.)

(5) The value of E_c may have an early morning hump with a small dip just before sunrise.

Fortunately, most of the violations to these rules took place in the summer, while the *Mariner* Mars 1969 encounters were winter events for the southern hemisphere station. This method will be called the "modified constant B" method of obtaining total electron content. Typical modifications to the f_{0F_2} values are shown in Fig. 6 with the resulting change in total electron content values shown in Fig. 5. As can be seen, this method considerably improves the August 15 results.

3. ***Daily scale height.*** In the preceding paragraphs it was assumed that at least one value of the total electron content was available during the day, from which the scale height could be determined. However, since the value of B for the particular time of day does not change much from day to day, the modified constant B method is still applicable, if weekly or even monthly values of B are used. Certainly the accuracy of the approximation is degraded in proportion to the scarcity of the B values. Figure 7 shows the daily variation of the noontime values of B at Stanford University for most of July and

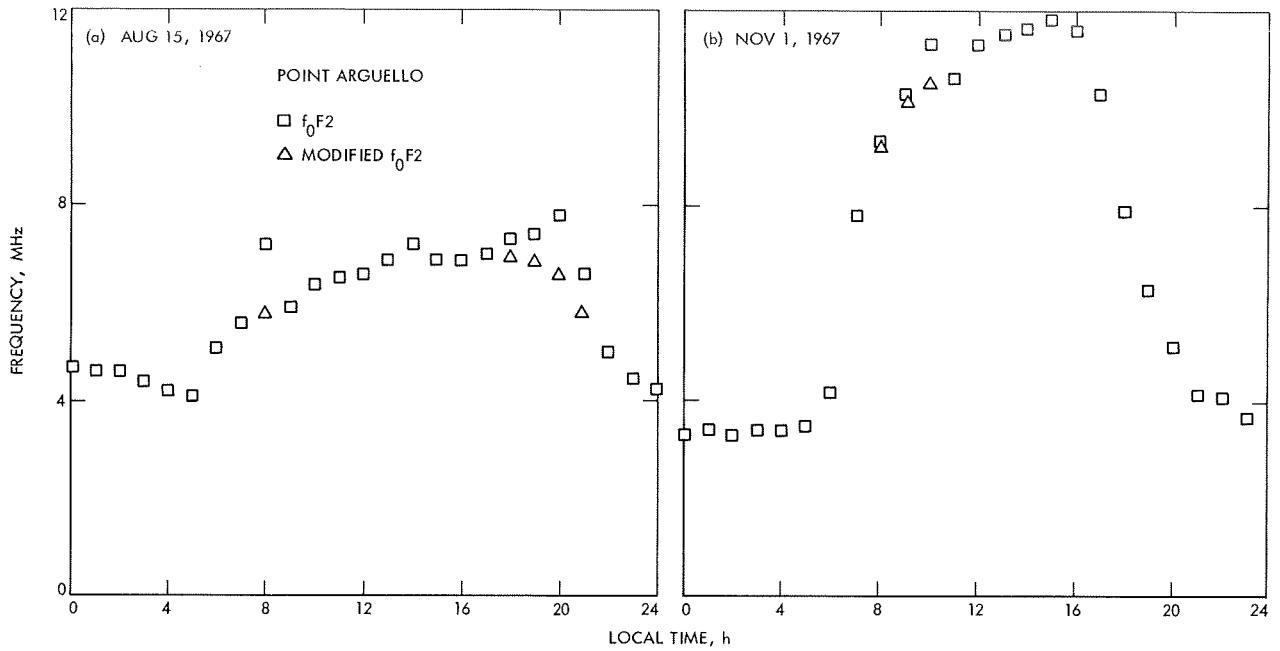

Fig. 6. Diurnal variation in $f_{0F}2$: (a) atypical day; (b) typical day

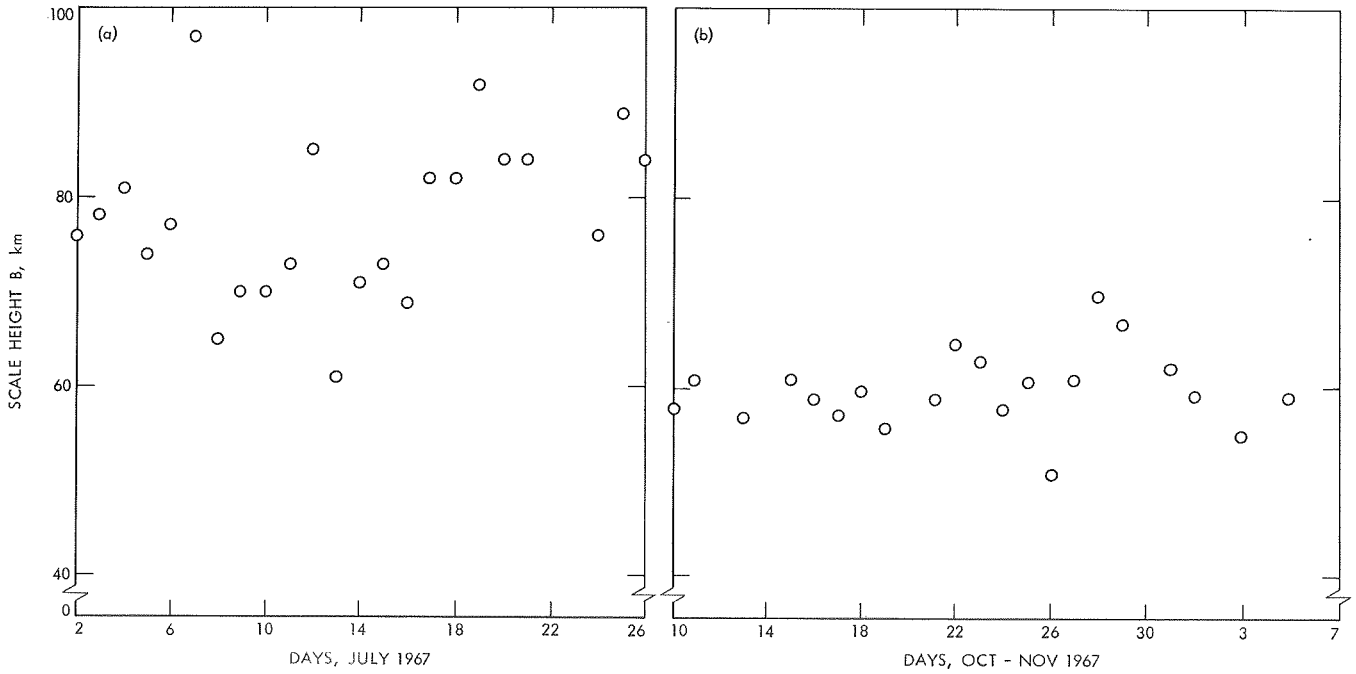

Fig. 7. Seasonal variation in scale height: (a) summer; (b) fall

October 1967. The standard deviations from the average value is 7% in October and 13% in July. Of course, the errors in the value of B could be as much as 60% in July and 37% in October if the reference B was determined on a day when it was a maximum or minimum. Once again, the variation of B, this time in a daily sense, appears to be larger in the summer than in the fall, winter, or spring.

4. Southern hemisphere data. The ionospheric data available for the southern hemisphere tracking stations for the *Mariner* Mars 1969 mission were as follows:

(1) From Johannesburg, South Africa,[3] for most days the data consisted of hourly values of f_{0F_2} starting on May 1, 1969, with noontime values of the total electron content computed by the Titheridge method.

(2) From Canberra, Australia,[4] the data consisted of hourly values of f_{0F_2} with scattered daytime values of Faraday rotation measurements around the beginning of August, from which it was decided to use a scale height of 40 km during July and August for both Australian stations.

(3) From Woomera, Australia,[5] the data consisted of hourly values of f_{0F_2} starting on July 15.

During July and early August, the data were supplied daily, except for the encounter days when data were sent hourly with a 3- or 4-h delay from the actual measurement times.

Even though the modified constant B method of obtaining total electron content was developed from California data, it was decided to use this method for the following reasons:

(1) The small amount of southern hemisphere total electron content measurements seems to support the method.

(2) A southern hemisphere ionosphere expert[6] agreed that this was probably the best approach.

(3) This method was the only one known to us that would give reasonable results with the available data.

[3]National Institute for Telecommunications, Johannesburg.

[4]Australian Bureau of Meteorology, Mt. Stromlo Ionosonde Station.

[5]Australian Bureau of Meteorology, Woomera Ionosonde Station.

[6]Professor Hibberd, University of New England, Armindale, New South Wales, Australia.

It was estimated that this method enabled total electron content values to be determined generally within 30%.

F. Estimation Based on Model Prediction

Even for Goldstone there was some delay in obtaining ionospheric data during the *Mariner* Mars 1969 mission. To perform calibration for real-time orbit determination, an attempt was made to predict the ionosphere. Figure 1 shows the effect of the ionosphere on apparent station location during the *Mariner V* mission. The effect on spin radius r_s is fairly consistent, especially over short periods, less than a week, for example. Longitude effect varies more dramatically, but would seem to also be predictable.

The following scheme was investigated to predict the ionospheric effect. As each day's data were received, they were fitted to a temporal model of the ionosphere. This model is stated as

$$E_{cm} = \begin{cases} D_c + A_c \cos(\omega t - \Phi) \\ D_c \end{cases} \quad \text{(whichever is greater)}$$

where

E_{cm} = modelled total electron content, electrons/m^2

D_c, A_c, and Φ = parameters of the model

ω = earth's rotational rate

Physically, D_c represents an estimate of the nighttime level of E_c, which is nearly constant; A_c is the amplitude of the diurnal pulse that occurs during the day. The parameter Φ is varied to estimate the time of the maximum ionization, which can occur any time between 11 a.m. and 3:30 p.m. local time.

It was hoped that by observing the day-to-day variation of these parameters, the predicted value of each parameter could be determined and the modelled electron content E_{cm} could be computed.

Figure 8 shows the day-by-day variation in D_c, A_c, and Φ from July 1 to August 5, 1969, for the ionospheric measurements made at Goldstone. Because of the sporadic behavior of these parameters, no attempt was made to predict the ionosphere for the *Mariner VI* or *VII* encounters. More analysis is required before a reliable prediction technique is formulated.

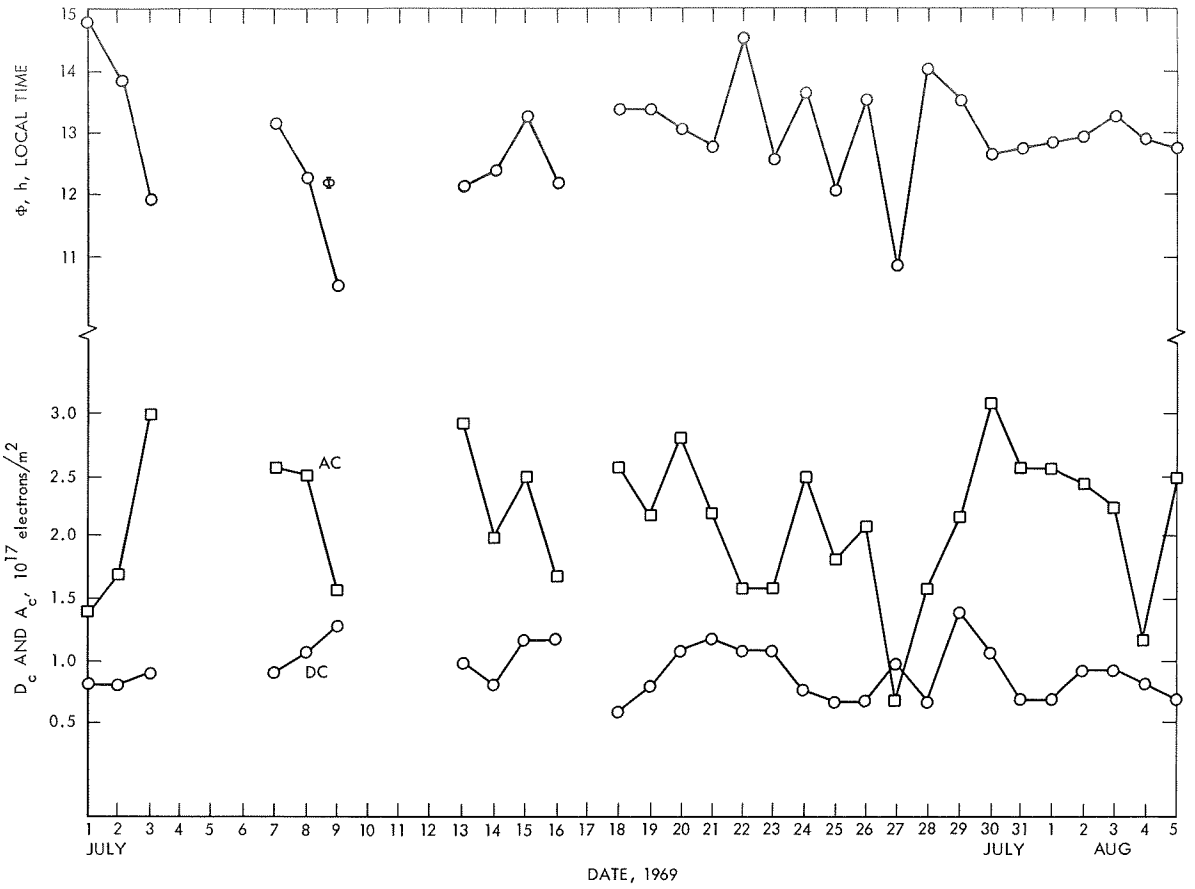

Fig. 8. Diurnal variation in ionospheric model parameters

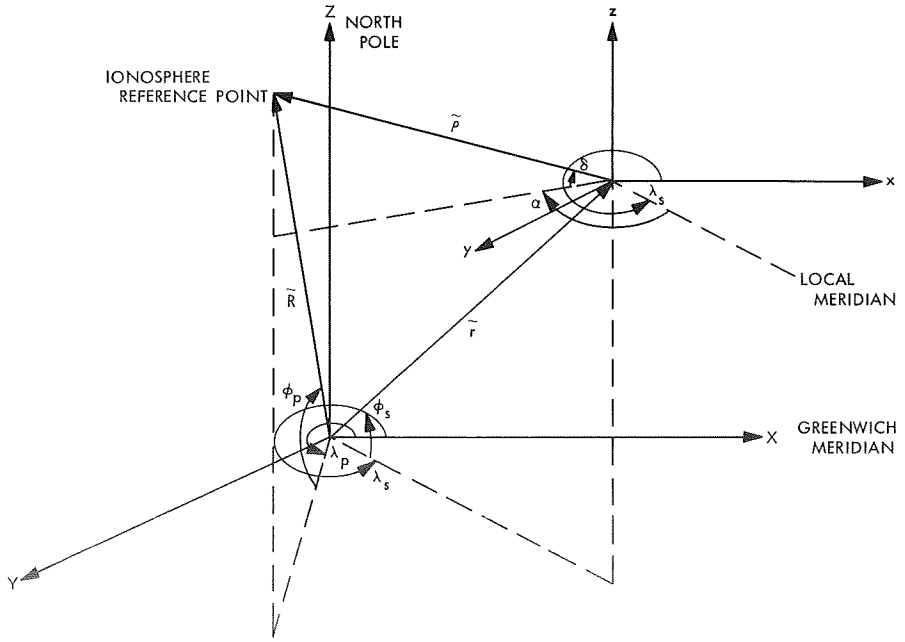

Fig. 9. Calculation of ionospheric reference point

IV. Mapping of Measurements

Ideally, calibration of the spacecraft signal should be computed from measurements made along the signal's ray path. Both the Faraday rotation and ionosonde measurements must be related to the ionosphere actually pierced by the *Mariner* spacecraft signal. A computer program called ION (described in Section VII-B) has been developed to calculate the differences between the ionospheric conditions at the point where a measurement was taken and the points where the spacecraft signal pierced the ionosphere during an entire pass. Adjustments are due to differences in the length of the ray path through the ionosphere, in the local hour angle of the sun, and in the geomagnetic latitude.

A. Computation of the Ionospheric Reference Point

To relate ionospheric measurements to tracking data, ionosphere reference points are calculated for both the measurement and the probe–station line of sight. The ionosphere reference point is defined as the point on the earth's surface directly below the point where the radio signal ray path is at reference altitude, typically 400 km. Ionospheric conditions at this point are used to typify conditions along the entire ray path. The validity of this assumption is under investigation and is discussed later.

The ionosphere reference point is computed as follows (see Fig. 9):

$$\tilde{R} = \tilde{\rho} + \tilde{r}$$

$$\tilde{r} = r \begin{bmatrix} \cos\lambda_s \cos\phi_s \\ \sin\lambda_s \cos\phi_s \\ \sin\phi_s \end{bmatrix}$$

$$\tilde{\rho} = \rho \begin{bmatrix} \cos(\lambda_s - \alpha)\cos\delta \\ \sin(\lambda_s - \alpha)\cos\delta \\ \sin\delta \end{bmatrix}$$

$$\tilde{R} = R \begin{bmatrix} \cos\lambda_p \cos\phi_p \\ \sin\lambda_p \cos\phi_p \\ \sin\phi_p \end{bmatrix}$$

where

$\tilde{R}$ = a vector from the center of the earth to the ionosphere reference point:

$|\tilde{R}| = R = h + R_e$, $h = 400$ km, R_e = earth's radius

$\tilde{\rho}$ = a vector from the station to the subionosphere point: $|\tilde{\rho}| = \rho = -R_e \sin\gamma + (2hR_e + h^2 + R_e^2 \sin^2\gamma)^{1/2}$, γ = elevation angle of probe

$\tilde{r}$ = a vector from the center of the earth to the station: $|\tilde{r}| = R_e$

λ_s and ϕ_s = station longitude and latitude

α and δ = probe's topocentric hour angle and declination

λ_p and ϕ_p = longitude and latitude of the subionosphere point:

$$\lambda_p = \tan^{-1}\left[\frac{\rho \sin(\lambda_s - \alpha)\cos\delta + R_e \sin\lambda_s \cos\phi_s}{\rho\cos(\lambda_s - \alpha)\cos\delta + R_e \cos\lambda_s \cos\phi_s}\right]$$

$$\phi_p = \sin^{-1}\left[\frac{1}{R}(\rho\sin\delta + R_e \sin\phi_s)\right]$$

The elevation angle γ is computed from α and δ by the spherical trigonometry relationships:

$$\sin\gamma = \sin\phi_s \sin\delta + \cos\phi_s \cos\delta \cos\alpha$$

B. Ray Path-Length Adjustment

The length of the ray path through the ionosphere is a function of elevation angle if the latitude and longitude variation in the ionosphere are neglected. Liu and Cain[7] have determined the ray path length as a function of elevation angle $R(\gamma)$ for various Chapman ionospheres by employing a ray trace program. The resulting $R(\gamma)$ for the Chapman model was approximated by an $R'(\gamma)$ based on a homogeneous or uniform ionosphere (by uniform is meant a constant charged-particle density from the lower limit h_1 to the upper, h_2):

$$R'(\gamma) = [(R_e + h_2)^2 - R_e^2\cos^2\gamma]^{1/2} - [(R_e + h_1)^2 - R_e^2\cos^2\gamma]^{1/2}$$

Table 1 shows the values of h_1 and h_2 that will result in the $R'(\gamma)$ that best approximates the $R(\gamma)$ for various values of h_{max} and a scale height of 39 km.

[7]Liu, A., and Cain, D., JPL internal document, Mar. 23, 1966.

Table 1. Values of h_1 and h_2 for various h_{max}

h_{max}, km	h_1	h_2
200	113	364
250	171	412
300	206.5	441.4
350	251	490

Currently, the $R(\gamma)$ for an h_{max} of 300 km is being used and is shown in Fig. 10; $R'(\gamma)$ is computed for the measurement and the station–probe line of sight. The ratio of these two numbers is used to adjust the measurement ray path length to the probe's ray path length.

C. Time Adjustment

Besides ray path-length adjustment, there is an additional time difference seen by the spacecraft signal that must be accounted for.

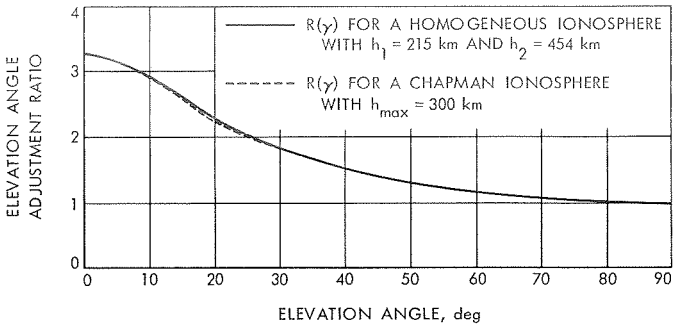

Fig. 10. Comparison of the elevation angle and adjustment ratio for a homogeneous and a chapman ionosphere

Consider a tracking station located on the equator viewing a spacecraft at zero declination (Fig. 11). Ionospheric measurements are obtained from an observatory on the equator monitoring a geostationary satellite. The ionospheric reference points, A and B, are defined by the

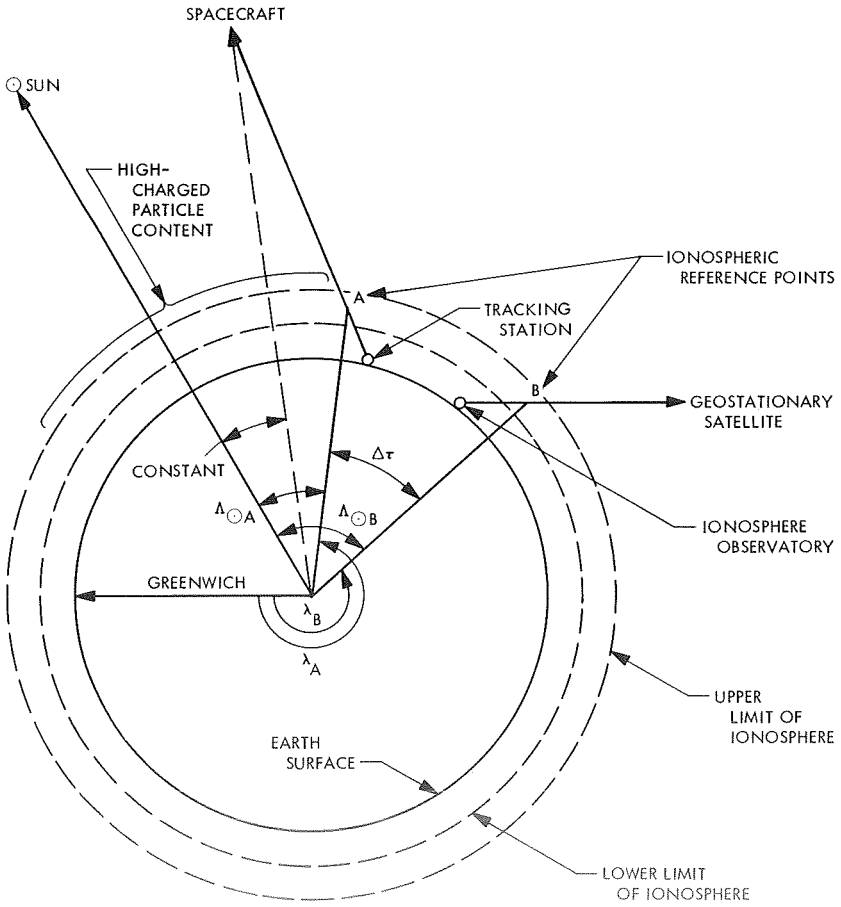

Fig. 11. Geometry for longitude time adjustment

coordinates (latitude and longitude) on the earth's surface directly below the point where the ray path reaches a reference altitude, usually taken as 400 km.

The diurnal variation of the ionosphere is caused by the sun. The local hour angle of the sun $\Lambda_\odot$ for ionospheric reference points A and B is shown in Fig. 11. Both $\Lambda_{\odot A}$ and $\Lambda_{\odot B}$ vary as the earth rotates. Measurements of the ionosphere made at point B must be related to point A by the instantaneous difference in local hour angles of the sun for the two ionospheric reference points. This difference is expressed by

$$\Delta\tau = \Lambda_{\odot A} - \Lambda_{\odot B} = \lambda_A - \lambda_B$$

where λ_A and λ_B are the longitudes of the two ionospheric reference points, and $\Delta\tau$ is the time adjustment which must be made to the ionospheric measurement.

D. Magnetic Latitude Adjustment

The third adjustment made as part of the mapping procedure is the adjustment for differences in geomagnetic latitude between the measurement and the probe's ray path. The geomagnetic latitude is determined for the measurement and probe's ionospheric reference point from

$$\sin\phi_m = \cos\phi_N \cos\phi_R \cos(\lambda_N - \lambda_R) + \sin\phi_N \sin\phi_R$$

where ϕ_m is the geomagnetic latitude; ϕ_N and λ_N are the geocentric latitude and longitude of the north magnetic pole (79°N, 291°E); ϕ_R and λ_R are the geocentric latitude and longitude of the ionospheric reference point.

The adjustment is then computed from

$$G = \frac{\pi - 2|\phi_m|}{\pi - 2|\phi'_m|}$$

where G is the adjustment ratio for geomagnetic latitude, and ϕ_m and ϕ'_m are the magnetic latitudes of the probe's and the measurement's reference points.

The path-length change Δl is computed from

$$\Delta l(t) = E_c(t - \Delta\tau)\left(\frac{R_P(\gamma)}{R_S(\gamma)}\right)\frac{Gk}{f^2}$$

where

E_c = measured columnar electron content used to compute the calibration

t = time

$\Delta\tau$ = time adjustment

$\frac{R_P(\gamma)}{R_S(\gamma)}$ = ratio of path-length adjustments for the probe P and the data source S

G = ratio of geomagnetic latitude adjustments

k = 40.3 in mks units

V. Computation of the Calibration

When the ION program (see Section VII-B) has mapped the measurements to the probe's ray path, the range and doppler calibrations are computed.

From Fig. 12 it can be seen that the charged-particle effect for one sample of two-way doppler Δf_2 taken over a count time of T_c involves the change in path length, Δl, resulting from four passes through the ionosphere (keyed by number in Fig. 12):

(1) The down-link pass at the end of the count time (received at t).

(2) The up-link pass corresponding to (1) (transmitted at $t - \tau$, where τ is the round trip time).

(3) The down-link pass at the start of T_c (received at $t - T_c$).

(4) The up-link pass corresponding to (3) (transmitted at $t - \tau - T_c$).

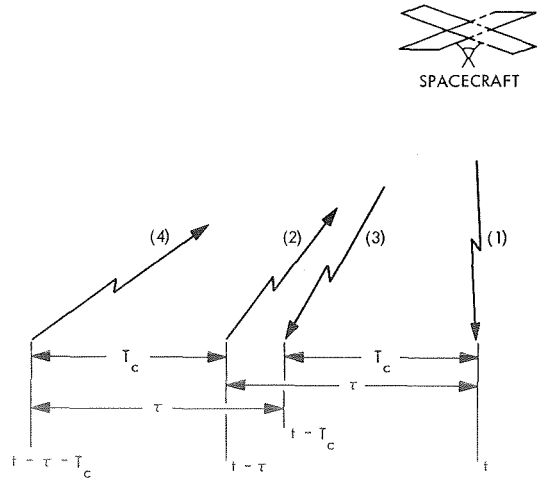

Fig. 12. Calculation of Δf_2

The effect in Hertz is then

$$\Delta f_2 = \frac{1}{T_c}\left[\{\Delta l_{up}(t-\tau) + \Delta l_{dn}(t)\} - \{\Delta l_{up}(t-\tau-T_c) + \Delta l_{dn}(t-T_c)\}\right]\left(\frac{f}{c}\right) \quad (7)$$

where

Δl = change in phase path length due to the charged particles, a negative quantity, m

f = received carrier frequency, Hz

c = speed of light, m/s

A turn-around ranging effect, $\Delta\rho$, is computed only for passes (1) and (2) listed above. The effect in meters is

$$\Delta\rho = \Delta l_{dn}(t) + \Delta l_{up}(t-\tau) \quad (8)$$

where

Δl = change in group path length due to the charged particles, a positive quantity, m

To calibrate ranging data, $\Delta\rho$ is converted to the change in round-trip light time $\Delta\tau$ by dividing by the speed of light.

For operational convenience, the program computes the correction independent of the actual time a sample was recorded, t. Instead, an arbitrarily selected time t' is used in Eqs. (7) and (8). Values of T_c, f, and τ must be entered as input data.

At present, the range and doppler effects are each fitted with a Tchebychev series up to order nineteen and the coefficients of the two series are punched on cards together with appropriate identification.

At the time of the *Mariner* Mars 1969 encounter, a power series was being used to fit the calibrations. The power series was not always capable of satisfactory fits. However, it was considered too risky to undertake the reprogramming that would have been required prior to encounter.

VI. Evaluation of the Calibration

The program HAMMEL uses the coefficients produced by ION to solve for the changes in a, b, and c due to the charged-particle effect. As discussed in Section II, the changes in r_s and $\Delta\theta$ that will result from applying the calibration can be predicted. The three parameters a, b, and c are solved for in closed form as follows:

$$\begin{bmatrix}\delta a\\ \delta b\\ \delta c\end{bmatrix} = \Lambda A^T \Delta f_2$$

where

δa, δb, and δc = minimum variance estimates of the changes in a, b, and c due to $\delta\dot{\rho}$

Δf_2 = calibration to observed doppler

Λ = Hamilton–Melbourne covariance matrix (Ref. 2) for a, b, and c for a symmetric pass:

$$\Lambda = \begin{bmatrix} \dfrac{1}{1-\rho_{13}^2} & 0 & \dfrac{-2\sin\psi}{\psi\left(1+\dfrac{\sin 2\psi}{2\psi}\right)\left(1-\rho_{13}^2\right)} \\ 0 & \dfrac{2}{\left(1-\dfrac{\sin 2\psi}{2\psi}\right)} & 0 \\ \dfrac{-2\sin\psi}{\psi\left(1+\dfrac{\sin 2\psi}{2\psi}\right)\left(1-\rho_{13}^2\right)} & 0 & \dfrac{2}{\left(1+\dfrac{\sin 2\psi}{2\psi}\right)\left(1-\rho_{13}^2\right)} \end{bmatrix} \frac{\sigma_\rho^2}{N}$$

where

N = number of observations spaced equally through the pass

σ_ρ^2 = variance of the doppler data noise

$$\rho_{13} = \frac{-2^{1/2} \sin \psi}{\psi \left[1 + \left(\frac{\sin 2\psi}{2\psi}\right)\right]^{1/2}}, \text{ the correlation of } a \text{ and } c$$

ψ = half-width of the pass, rad

and

$$A^T = \left[\frac{\partial \Delta f_2}{\partial a} \quad \frac{\partial \Delta f_2}{\partial b} \quad \frac{\partial \Delta f_2}{\partial c}\right] = [1 \ \sin \omega t \ \cos \omega t]$$

Since the doppler calibration Δf_2 is in analytic form

$$\Delta f_2 = \sum_{j=0}^{n} P_j t^j$$

the dot product of A^T and Δf_2 can be written as

$$A^T \Delta f_2 = \frac{1}{2T} \begin{bmatrix} \int_{-T}^{T} \sum_{j=0}^{n} P_j t^j \, dt \\ \int_{-T}^{T} \sum_{j=0}^{n} P_j t^j \sin \omega t \, dt \\ \int_{-T}^{T} \sum_{j=0}^{n} P_j t^j \cos \omega t \, dt \end{bmatrix}$$

where

n = order of the Δf_2 power series

P_j = coefficients of the series

T = time of one-half the pass width

Performing the integration gives

$$A^T \Delta f_2 = \frac{1}{2T} \left[\sum_{j=0}^{n} \frac{P_j}{j+1} t^j \Bigg|_{-T}^{T} \right.$$

$$\sum_{j=0}^{n} P_j \left[-\frac{\cos \omega t}{\omega^{j+2}} \sum_{\nu=0}^{j/2} (-1)^{\nu+1} \frac{j!}{(j-\nu)!} (\omega t)^{j-\nu+1} + \frac{\sin \omega t}{\omega^{j+2}} \sum_{\nu=0}^{(j-1)/2} (-1)^{\nu} \frac{j!}{(j-\nu)!} (\omega t)^{j-\nu+1} \right]_{-T}^{T}$$

$$\left. \sum_{j=0}^{n} P_j \left[\frac{\sin \omega t}{\omega^{j+2}} \sum_{\nu=0}^{j/2} (-1)^{\nu} \frac{j!}{(j-\nu)!} (\omega t)^{j-\nu+1} + \frac{\cos \omega t}{\omega^{j+2}} \sum_{\nu=0}^{(j-1)/2} (-1)^{\nu} \frac{j!}{(j-\nu)!} (\omega t)^{j-\nu+1} \right]_{-T}^{T} \right]$$

The program HAMMEL evaluates the results of this integration and premultiplies by Λ, thus obtaining δa, δb, and δc. From these, δr_s and $\delta \Delta \theta$ are computed. The identical approach is used by the Tchebychev version of HAMMEL. The power series approach is shown here since it is more easily followed. The *Mariner IV* and *Mariner V* encounter tracking data have been calibrated for ionospheric effect for the Goldstone DSCC stations. The resulting change in station location for runs made by the Double Precision Orbit Determination Program (DPODP) and HAMMEL are shown in Table 2. The results are averages over the week of each encounter. The differences between DSS 12 and DSS 14 occur because these stations were not tracking on the same days.

The results are quite close when one considers that the DPODP is solving for other parameters in addition to station locations. Also, HAMMEL computes the effect of applying the calibration over the entire pass. In actual practice, the calibration can be applied only to the tracking data available, which is usually less than a full pass.

Table 2. Station location changes due to removing the charged-particle effect

Station	DPODP actual change, m	HAMMEL predicted change, m
Mariner IV encounter		
DSS 11		
Spin radius	0.65	0.398
Longitude	2.58	2.62
Mariner V encounter		
DSS 12		
Spin radius	5.5	5.75
Longitude	−5.3	−2.5
DSS 14		
Spin radius	6.0	6.1
Longitude	−4.8	−4.4

Typical electron content profiles together with the range and doppler effects for the *Mariner IV* and *V* encounters are shown in Fig. 13. The electron contents (Figs. 13a, b, c) are shown for a 90-deg elevation angle over Goldstone DSCC. The ionospheric data were obtained from Stanford Faraday rotation measurements of geostationary satellites and mapped to the Goldstone DSCC zenith. The range corrections (Figs. 13d, e, f) are different in shape from the electron content curves because of the variation in elevation and azimuth angles of the spacecraft through the pass, which result in changes in the path length through the ionosphere and differences in ionospheric conditions along the path. The doppler corrections (Figs. 13g, h, i) are obtained by differentiating the range corrections. The spans of tracking data used by the DPODP are shown in Figs. 13g, h, and i.

The doppler correction curves show why the ionosphere affected r_s more for *Mariner V* than for *Mariner IV*. All three doppler curves have the appearance of antisymmetric complex wave forms. The amplitude of the wave form determines the change in b and hence in r_s. For *Mariner IV*, the doppler correction on July 14, 1965 (Fig. 13g) has an amplitude of about 0.0023 Hz. This is typical for the entire week of the encounter. For *Mariner V*, the doppler corrections for October 17 and 18, 1967 (Figs. 13h, i) have amplitudes of about 0.065 and 0.06 Hz, respectively, and are also typical of the entire week. Consequently, the change in r_s is about an order of magnitude greater for *Mariner V* than for *Mariner IV*.

Admittedly, the doppler correction curves are not very symmetric; but if we imagine an axis of symmetry lying between the two peaks, we can see that for the *Mariner IV* doppler correction (Fig. 13g) the axis of symmetry occurs about 20 min before meridian crossing. For *Mariner V*, the axis of symmetry on both days (Figs. 13h, i) occurs about 20 min after meridian crossing. This accounts for the difference in sign of the change in longitude for the two encounter periods.

The original purpose for developing HAMMEL was to assess the effect on DPODP solutions of the charged-particle calibration. This purpose has been realized. HAMMEL has also been found useful for the following purposes:

(1) To detect erroneous calibrations before they are entered in the DPODP. HAMMEL's running time on the IBM 7094 computer is less than a second per case, which makes it an effective means to detect bad calibration data.

(2) To evaluate the accuracy of various calibration schemes. The present method of evaluation of the model of the ionosphere, which is being developed for in-flight calibration of tracking data when measurements cannot be obtained in real time, is to compare measured and modeled ionospheres throughout a diurnal cycle. HAMMEL can be used to compute the effects on DPODP solutions of calibrations based on measured and modeled ionospheres. This will directly determine the errors in the solution caused by deficiencies in the ionosphere model and provide better criteria for judging the model's performance than has been previously available.

(3) To evaluate the effect of other error sources. HAMMEL can be used in a similar manner to evaluate the error sources for effects other than charged particles (e.g., tropospheric) as long as the effect can be written as a power series or, for the new version of HAMMEL, in a Tchebychev or power series.

VII. Application of the Calibration

As shown in Fig. 14, three IBM 7094 computer programs were specifically involved with providing ionospheric calibrations to the DPODP:

(1) PREION—a preprocessor that reads in ionospheric data in various formats, converts the data to a

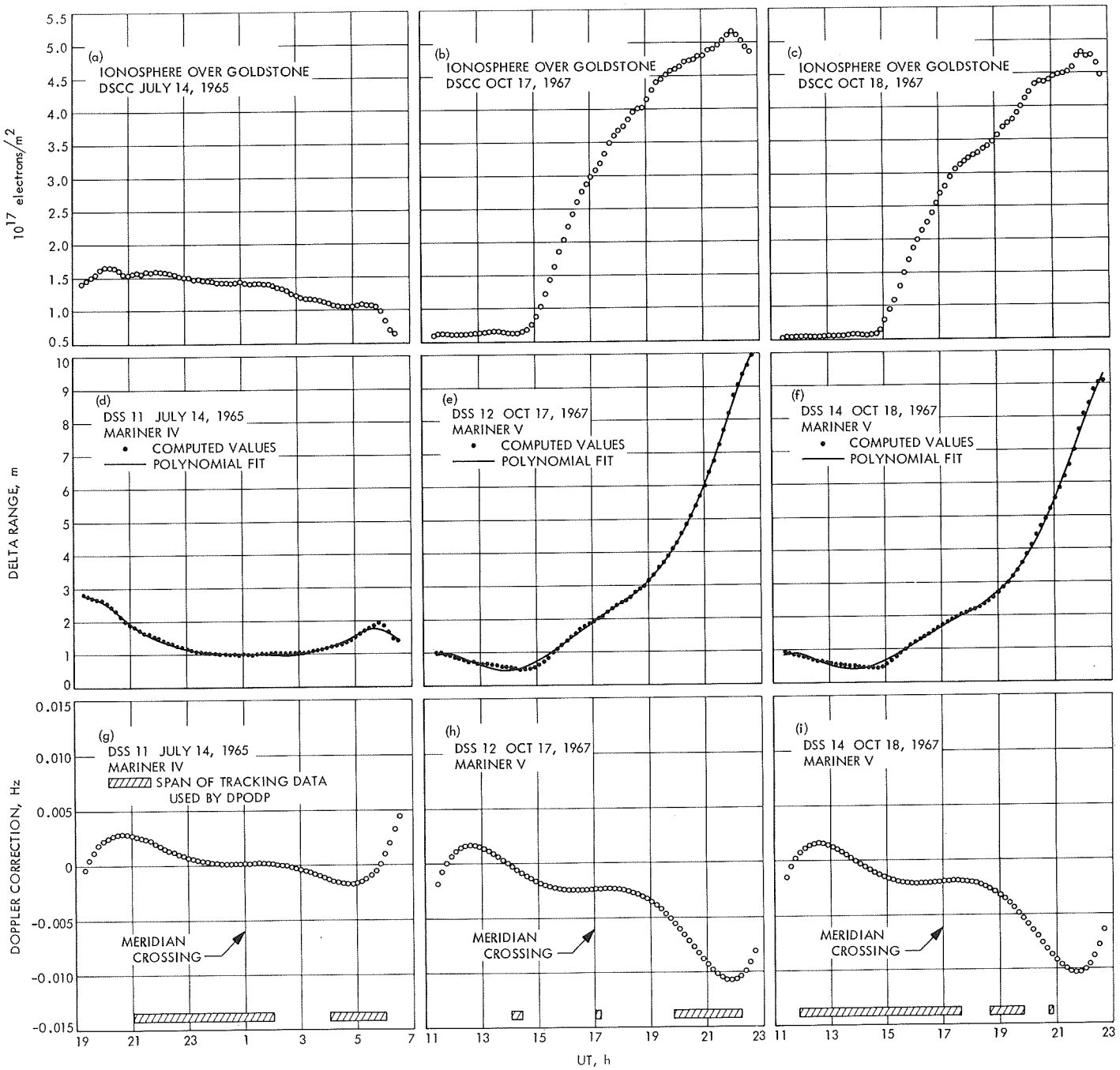

Fig. 13. Electron count profiles, range corrections, and doppler corrections for *Mariner IV* and *V* encounters

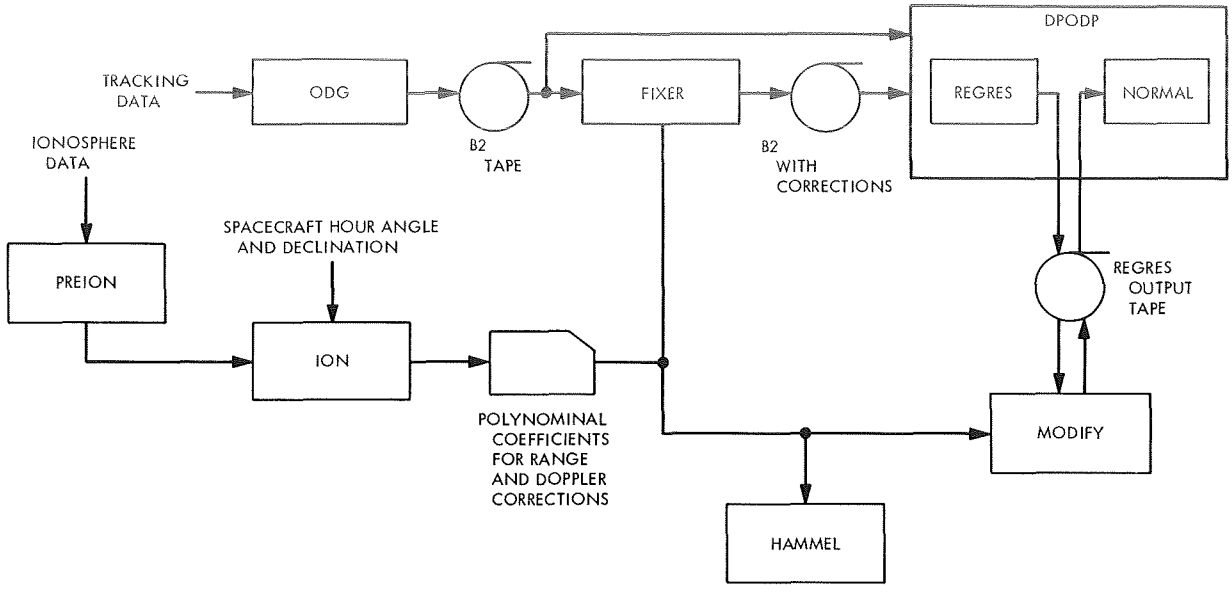

Fig. 14. Ionospheric data flow diagram

standard form, fits the data, and solves for the parameters of the temporal model of the ionospheres.

(2) ION—the program that calculates the actual calibrations to range and doppler.

(3) HAMMEL—a post-processor that predicts the effect of applying the calibration to assist in analysis of DPODP results and to detect erroneous calibrations.

A. PREION

Ionospheric measurements are received via teletype and punched on paper tape in the SFOF. These tapes in teletype Baudot code are read into the PDP-7 computer, which uses a program called CONPAT to translate from Baudot to BCD code and to write a magnetic tape record of the data. The magnetic tape is transferred to the IBM 7094 computer, where it is read in under control of the PREION program.

Data received from Goldstone are the unconditioned output of the receiver–polarimeter. This device measures Faraday rotations from 0 to 180 deg of the signal received from the ATS-1 satellite. This signal, transmitted at 137 MHz, undergoes approximately two to five rotations of increase and decrease during the day. Consequently, algorithms have been developed within PREION to resolve the ambiguities in the data and reconstruct the daily variation. PREION is not capable of detecting every retrace and some hand corrections are required to remove the remaining ambiguities.

The receiver–polarimeter determines rotations from 0 to 180 deg. The device then retraces from 180 back to 0 deg. Samples are digitized every second and averaged over 1 min. Because of noise, the values recorded near 0 or 180 deg contain samples from both sides of the retrace.

For example, the original record of a constantly increasing ionosphere appears to be a series of alternate increases (from 0 to 180 deg) and decreases (from 180 to 0 deg). The decreases are actually retraces. But experience is required before retraces in the original record can be distinguished from actual decreases in the measured value.

Figures 15–17 show original data records and reconstructed data, electron content in 10^{17} electrons/m^2. The nighttime reading of the ionosphere is fairly constant (Fig. 15). However, the original data may stay very near the retrace point for a long period of time (Fig. 16). Noise causes the original data to fluctuate wildly through the full range when the actual measurement remains nearly constant, within a few degrees of the 0 to 180 deg point.

Another difficult situation arises when the midday peak occurs at the retrace point. Multiple retraces will occur and appear as rapid changes (both increases and decreases) between 0 and 180 deg when the actual measurement remains almost constant. Figure 16 shows two double retraces, one at 18:00 (GMT) and a second at 19:15.

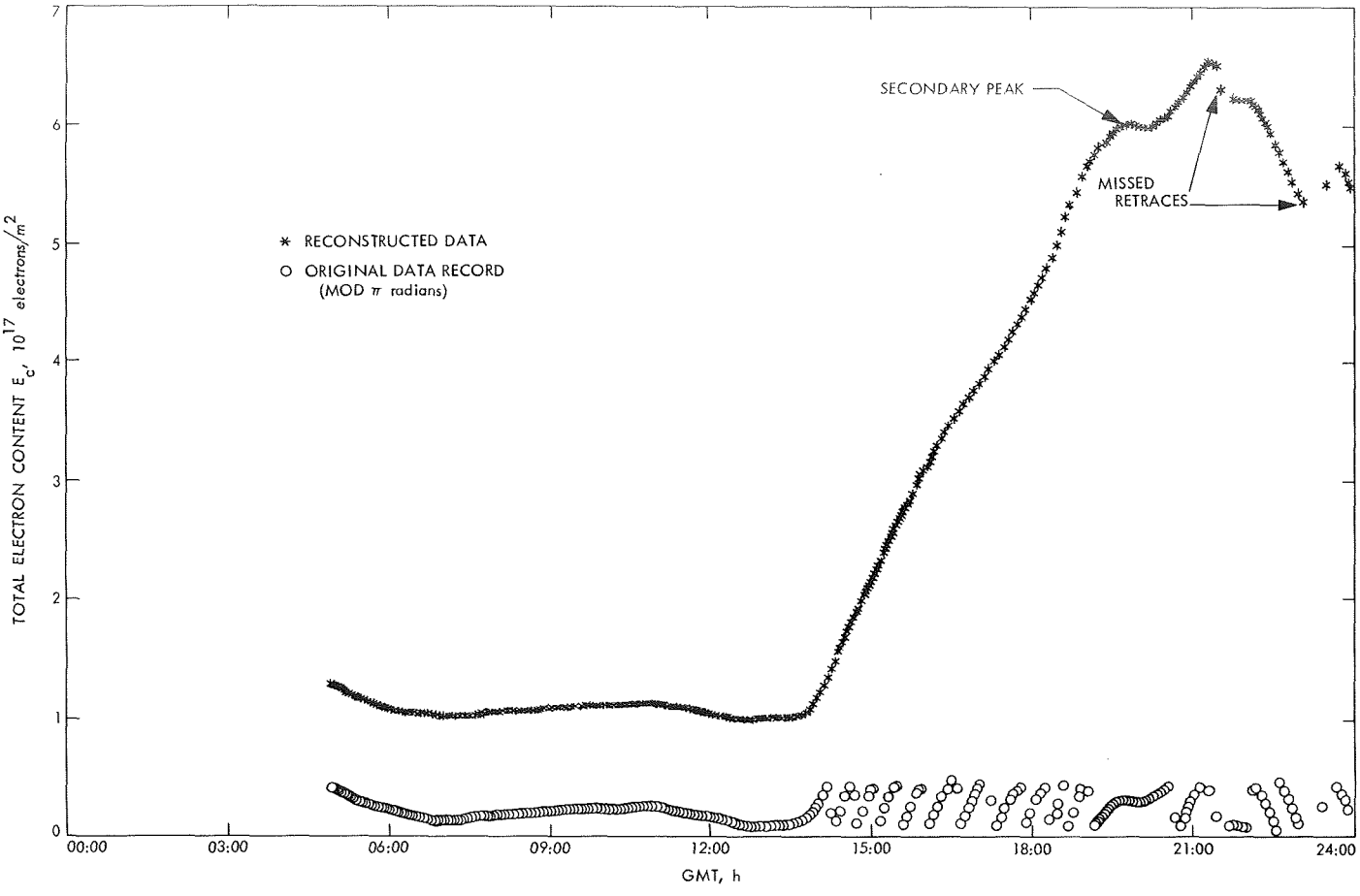

Fig. 15. Faraday rotation data: October 24, 1968

If a retrace is not detected, the electron content will be in error by 5×10^{16} electrons/m^2. This is a 20% error on a typical day.

No single retrace detection scheme is effective because of the varying characteristics of the ionosphere during the day. For example, the electron content remains very nearly constant throughout the night and increases in the morning, reaching a peak between noon and 3:00 p.m. (Figs. 15–17). After this, the content decreases as the free electrons and ions recombine into neutral atoms.

Consequently, the method used to detect retraces varies with the time of day. Four time areas have been defined, each with its own scheme. These areas are the night (I), the morning (II), the midday (III), and the afternoon (IV). Although different standards are set to distinguish between changes in content and retraces for each of these time areas, the basic logic of the program is the same throughout the day. All data are tested against the criteria for the time area in which they were recorded. Any data point out of tolerance initiates a retract test. This test is continued until three consecutive points are within tolerance. All the points out of tolerance—the points collected while the retrace test was in progress—are evaluated as a group. If the group fails to pass, it is rejected as a retrace, a quadratic polynomial is fitted through the resulting gap, and one-half rotation is added to or subtracted from subsequent data. If the group passes, it is all accepted as valid data and no adjustment of absolute level is made.

The strategy used in each of the time areas is as follows:

1. Time area I, 10 p.m. to 5 a.m. local time. During time area I the electron content is at the minimum and its rate of change quite slow. Points encountered here are tested for slope. If the absolute value of the slope exceeds 250 deg of rotation/h, the point is considered questionable and a retrace test initiated. If the excursion over the entire retrace test exceeds 90 deg of rotation, it is considered a retrace.

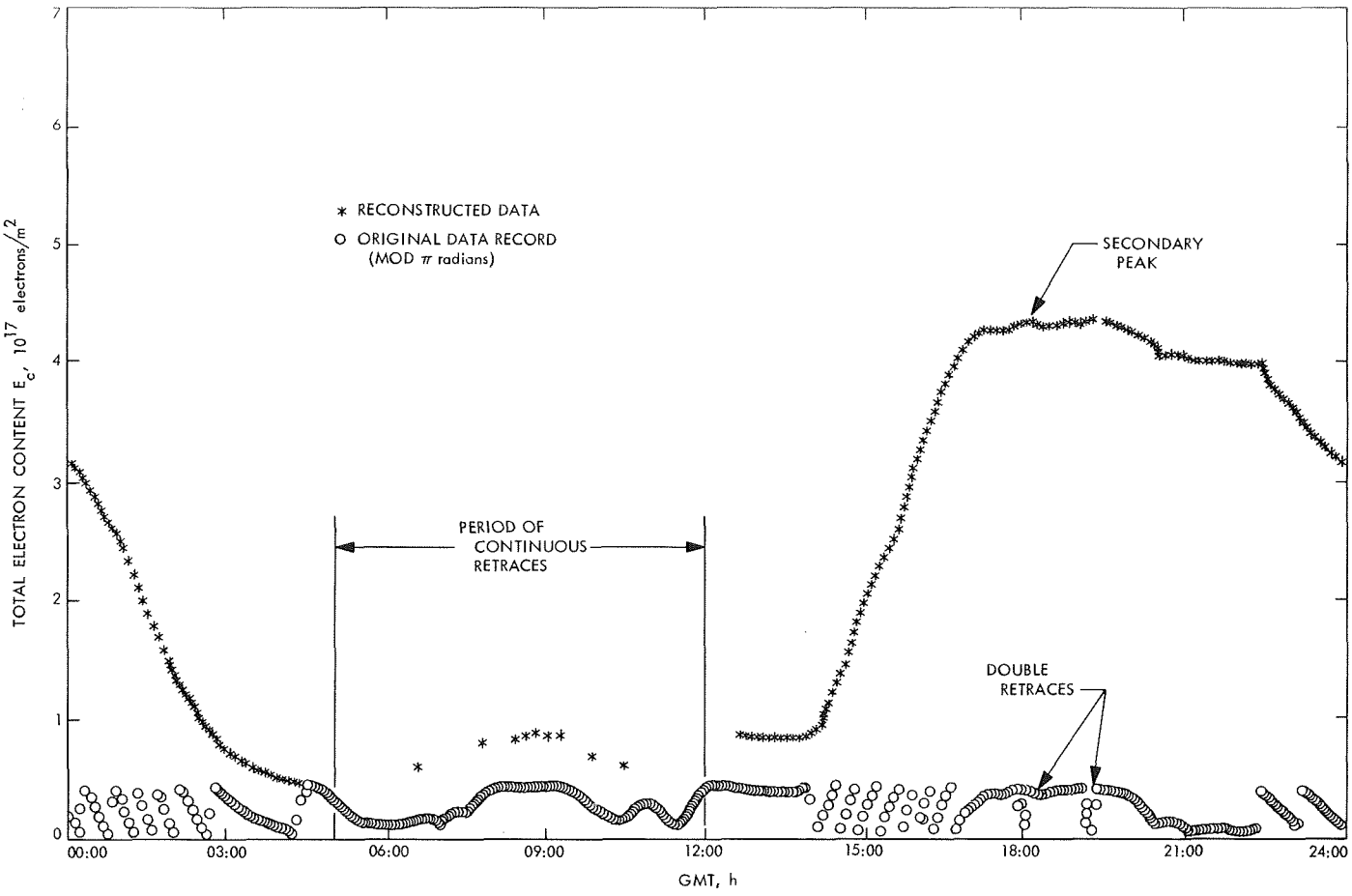

Fig. 16. Faraday rotation data: November 7, 1968

2. *Time area II, 5 a.m. to 8 a.m., and time area IV, 2 p.m. to 10 p.m. local time.* During time area II and time area IV the electron content is steadily increasing and steadily decreasing, respectively. Points encountered in these areas are tested on the sign of the current slope. If the sign is not in agreement with the predicted sign, the point is considered questionable. Each successive point is tested for a retrace. The excursion is computed and if it exceeds 90 deg of rotation a retrace is detected.

3. *Time area III, 8 a.m. to 2 p.m. local time.* During time area III the electron content reaches its maximum value. Frequently, secondary peaks occur (Figs. 16 and 17) and so a test of the sign of the slope is not adequate, since both increases and decreases may occur in any order. This time area is the most difficult in which to assign definite characteristics. For this reason the testing is more extensive and complex than in the other time areas.

Points in this area are tested initially on the absolute value of the current slope. It is assumed that any point giving an absolute value less than 667 deg of rotation/h is valid data. This is a larger maximum slope than is used in area I. A point not passing this test is held as questionable, along with successive points.

The routine for testing the successive data computes the excursion, and the time of excursion, for each point received. In this area if the excursion exceeds 90 deg and if the time of excursion is not greater than 10 min, the data group is considered a retrace. If both of these restrictions are not met, the group of data is considered valid.

As part of the initialization process, the program consults the ionosphere model, discussed in Section III-F, to determine the absolute electron content. This absolute level is used as the starting point. Retraces are then used to add or subtract levels as the day progresses. If a large data gap occurs, the program reinitializes processing and the model is used to determine the absolute level.

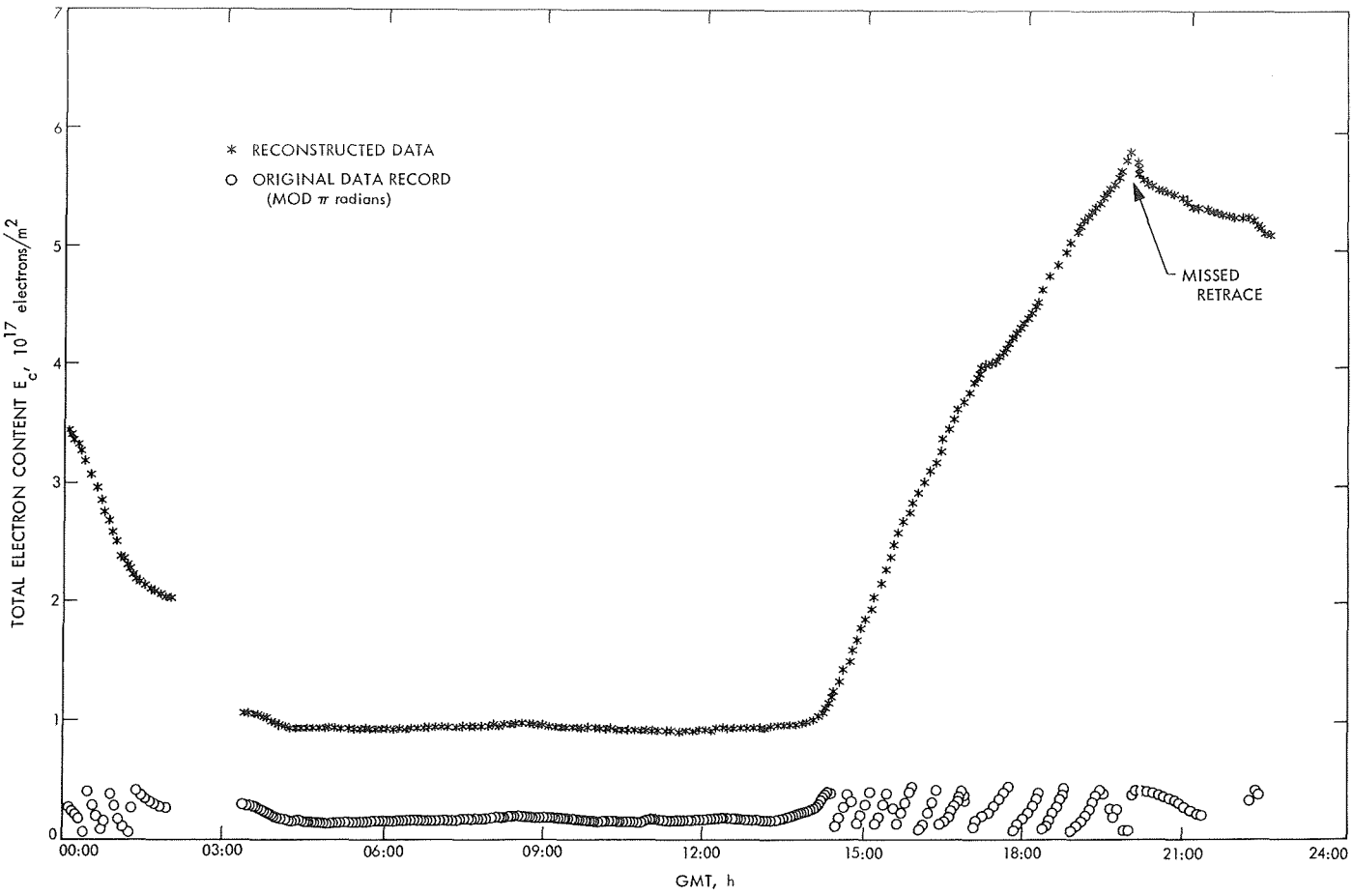

Fig. 17. Faraday rotation data: November 20, 1968

The program will accept data records starting at any time of day, take the predicted electron content provided by the model, and process data with this starting point. The program checks to be sure that, as retrace levels are subtracted, the absolute level never falls below a minimum specified value. If this minimum is reached, the program considers the starting level provided by the model in error, and reprocesses all previous data, adding in one retrace level to all the measurement.

An additional check is made to assure that the model has not predicted the ionosphere at too high a starting level. The ionosphere is least active early in the morning, about 2 a.m. local time; consequently, the model predicts the ionosphere most accurately at 2 a.m. As the data record reaches 2 a.m. local time, the program checks the absolute level against a new estimate provided by the model. This new estimate is used in preference to the original one. All previously processed data are adjusted by the number of half-rotation levels by which the two estimates were in disagreement.

Though PREION proved to be fairly successful, some shortcomings in the program should be noted. Figures 15 and 17 show retraces that were missed and had to be eliminated by additional post-processing. Though the percentage of retraces missed is probably well below 10% in spring, fall, and winter when the ionosphere model is most accurate, the performance of the program drops in the summer months when the ionosphere diurnal variation has the appearance of a plateau (Fig. 18) rather than the mountainous appearance (Figs. 15–17) typical of non-summer months. Consequently, PREION could probably be improved if the different characteristics of the summer ionosphere were incorporated in the logic of the program.

Another difficulty uncovered was that due to missed retraces. The pre-midnight measurement at the end of one day did not always agree with the post-midnight measurement at the beginning of the next day. If PREION is revised in an attempt to fully automate the

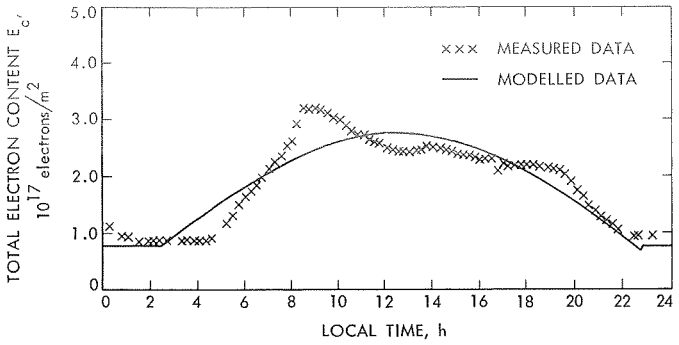

Fig. 18. Total electron content, Goldstone, Calif., July 14, 1969

program, the final value of the last day processed should be available to initialize processing of the following day.

B. ION

The program ION reads in the conditioned ionospheric data and information necessary to identify the pass of tracking data to be calibrated. This information consists of the DSN station, the date of the pass, the rise and set times for the spacecraft, the topocentric hour angle and declination for the spacecraft, the nominal frequency of the S-band signal received from the spacecraft, the time interval for which corrections are to be calculated, and the type of calibration to be produced, doppler or doppler and range.

ION begins computation at spacecraft rise and stops at spacecraft set to produce a calibration for the entire horizon-to-horizon pass. As described in Section IV, the point where the spacecraft ray path pierced the ionosphere is calculated. Adjustments are made for the different ionospheric conditions at this point and the point where the measurement of the ionosphere was made.

From the adjusted ionospheric data, a range correction is computed. This point-by-point correction is fitted with a polynomial. The range correction polynomial is differenced to obtain a doppler correction polynomial. The doppler polynomial's coefficients, together with information identifying the pass, are punched out.

C. HAMMEL

The program HAMMEL is described in detail in Section VI. The program fits the doppler polynomial produced by ION with a constant, a sine wave, and a cosine wave. The amplitude of the sine wave determines the apparent change in station spin radius r_s, while the cosine determines the change in longitude λ. If the values of r_s and λ are reasonable, the correction can be assumed to be valid.

VIII. Results of the *Mariner VI* and *VII* Ionospheric Calibration

As previously described, ionospheric measurements were obtained from the Faraday rotation polarimeters at the Venus DSS and at the University of New England, Armidale, Australia, and from ionosonde vertical sounding stations at Tortosa, Spain, Mount Stromlo, Australia, Woomera, Australia, and Johannesburg, South Africa. These measurements were converted to total electron content, mapped to the *Mariner* ray path, and range and doppler corrections were computed (the ionosphere constants used during the *Mariner* Mars 1969 encounter are listed in the Appendix) and applied to *Mariner VI* and *VII* radio tracking data. This resulted in the recommended changes shown in Table 3, in which $B \cdot T$ is the component of the B vector (a vector from the center of the planet to the aiming point) in the ecliptic plane and $B \cdot R$ is the component perpendicular to $B \cdot T$.

The recommended changes listed in Table 3 were determined by differencing the results of (1) the DPODP solutions from in-flight data that had not been calibrated for the ionosphere effect and station location based on post-flight solutions from uncalibrated data vs (2) DPODP solutions from ionospherically calibrated data and station location based on post-flight calibrated data. These differences are not necessarily the actual ionospheric effect on the orbit determination, since the error introduced by the ionosphere into the in-flight data might be masked in part by the uncalibrated station location.

For example, Fig. 1 shows that for *Mariner V*, the ionosphere caused an error that consistently increased the apparent station spin radius r_s. It is very likely that the ionosphere had a similar effect for *Mariner* Mars 1969. Consequently, station locations based on uncalibrated *Mariner V* data would compensate in part for the ionospheric error in *Mariner* Mars 1969 data.

The ionospheric effect was considerably lower than was anticipated. Although 1969 was a year of high ionospheric concentrations due to solar flare activity, in the period when the calibration was performed, July 1 to August 5, 1969, the ionosphere was relatively inactive. This low activity was particularly noticeable in the southern hemisphere, where the total columnar electron ionospheric content was typically less than half of the content in the northern hemisphere. Because of the southerly

Table 3. Recommended changes due to ionospheric effect, *Mariner* Mars 1969 mission

Data source	$B \cdot R$, km	$B \cdot T$, km
Mariner VI	−53	48
Mariner VII	−40	20

declination of the *Mariner* spacecraft, most of the radio tracking data were obtained from southern latitude stations. Consequently, the smaller effect of the southern latitude ionosphere outweighed the effect in the northern latitude ionosphere and reduced the magnitude of the calibration for the entire net.

IX. Conclusion and Recommendations

The lack of a method for measuring charged-particle effects directly from the spacecraft signal for all DSN stations is an extremely unfortunate circumstance of the *Mariner* Mars 1969 mission. The difficulty in obtaining measurements, the delays involved in receiving the data, and the error inherent in mapping measurements to the spacecraft ray path would all be eliminated if the *Mariner VI* and *VII* radio signals provided a charged-particle measurement.

The extensive development required to produce the programs and procedures described in this article, together with the effort expended in contacting and negotiating with ionospheric scientific groups in Spain, South Africa, and Australia could be avoided if one or more of the charged-particle measuring techniques—dual frequency, planetary ranging, and Faraday rotation—are incorporated in the design of the telecommunications flight and ground equipment in future missions.

References

1. Davies, Kenneth, *Ionospheric Radio Propagation*, Monograph 80. National Bureau of Standards, Washington, D. C., Apr. 1, 1965.
2. Hamilton, T. W., and Melbourne, W. G., "Information Content of a Single Pass of Doppler Data From a Distant Spacecraft," in *The Deep Space Network*, Space Programs Summary 37-39, Vol. III, pp. 18–23. Jet Propulsion Laboratory, Pasadena, Calif., May 31, 1966.
3. Lawrence, R. S., Little, C. G., and Chivers, H. J. A., "A Survey of Ionospheric Effects Upon Earth-Space Radio Propagation," in *Proc. IEEE*, Jan. 1964.
4. MacDoran, P. F., and Wimberly, R. N., "Charged-Particle Calibration From Differenced Range Versus Integrated Doppler—Preliminary Results From *Mariner* Mars 1969," in *The Deep Space Network*, Space Programs Summary 37-58, Vol. II, pp. 73–77. Jet Propulsion Laboratory, Pasadena, Calif., July 31, 1967.

Appendix

Ionosphere Constants

The ionosphere constants used during the *Mariner* Mars 1969 encounter in computing the range effect of the charged particles and mapping the effect to the desired ray path are listed in Table A-1.

Table A-1. Ionosphere constants

Data source	Station longitude, deg E	Station latitude, deg	Ionosphere reference point, longitude	Ionosphere reference point, latitude	Ray path length term	Magnetic latitude factor
Stanford Univ.						
ATS-1 Faraday rotation	237.84	37.4	234.38	34.2	1.53446	0.83863
SYMCOM III Faraday rotation	237.84	37.4	225.14	33.557	2.75796	0.87634
Dual frequency	237.84	37.4	Variable	Variable	Variable	Variable
Goldstone						
ATS-1 Faraday rotation	243.20523	35.066505	239.16	32.0964	1.58321	0.85732
ESSA						
Woomera	136.3	−30.8	136.3	−30.8	1.0	0.81738
Canberra	149.0	−35.3	149.0	−35.3	1.0	0.77417
Johannesburg	28.1	−26.07	28.1	−26.07	1.0	1.05821
Ebro, Tortosa, Spain	0.0	40.0	0.0	40.0	1.0	0.76381
Pt. Arguello, Calif.	239.4	33.8	239.4	33.8	1.0	0.83112

Note: Conversion of electron content E_c to range:

Range $= E_c K\ 1.6 \times 10^8/(2\pi \times \text{frequency})^2$

K = secant of zenith angle

($K = 1.51$ for Stanford ATS-1; $K = 2.8114414$ for Stanford SYMCOM III;

$K = 1$ for all others)

The Troposphere

V. J. Ondrasik

Before the *Mariner* Mars 1969 encounter, the Double Precision Orbit Determination Program was set up to try to eliminate the tropospheric range error by using the model described in the expression[1]

$$\Delta\rho_I = \frac{1.8958}{(\sin\gamma + 0.06483)^{1.4}} \frac{N_j}{340.0}, \text{ m} \qquad (1)$$

where γ is the elevation angle and N_j is a recommended value of surface refractivity for each station.

This equation was obtained by fitting a curve of the form

$$\Delta\rho = \frac{A}{(\sin\gamma + B)^c}$$

to the range errors of Fig. 1, which were obtained by ray tracing through the indicated refractivity profile. Figure 2 shows the difference between the ray tracing errors and the model of Eq. (1).

A few weeks before the *Mariner* Mars 1969 encounter, it was noted by Dan Cain[2] that at elevation angles above approximately 15°, where most of the data was taken, the model of Eq. (1) was not a particularly good fit to Fig. 1. He therefore recommended a new model, which is expressed as

$$\Delta\rho_{II} = \frac{2.6}{\sin\gamma + 0.015} \frac{N_j}{340.0}, \text{ m} \qquad (2)$$

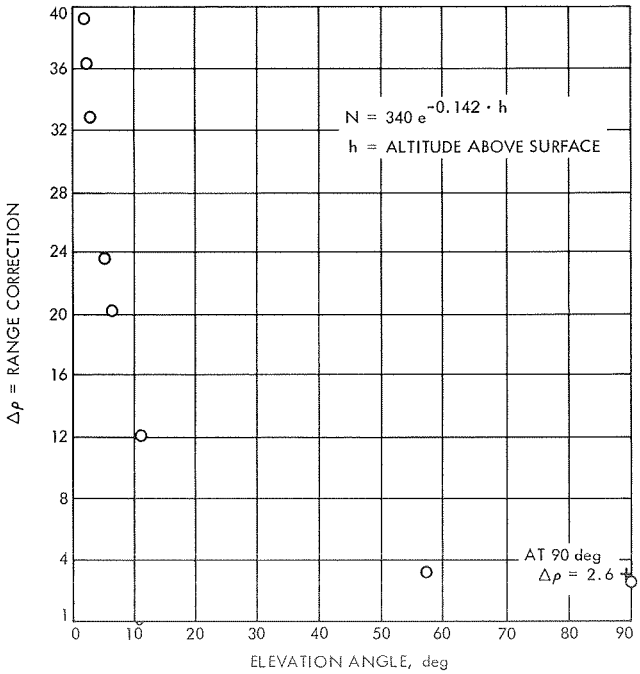

Fig. 1. Tropospheric range errors

[1]Liu, A., "Recent Changes to the Tropospheric Refraction Model Used in the Reduction of Radio Tracking Data From Deep Space Probes," in *The Deep Space Network*, Space Programs Summary 37-50, Vol. II, pp. 93–97, Mar. 31, 1969.

[2]Personal communication to D. Curkendall.

The difference in the range error between this model and the ray-trace results is shown in Fig. 2. Clearly, the model of Eq. (2) is far superior to the model of Eq. (1) for elevation angles of more than approximately 12 deg. For this reason it was decided to use the new model of Eq. (2) and delete all data obtained when the elevation angle was less than 15 deg. This new model decreased the tropospheric correction to the estimate of the distance of a station off the spin axis by about 0.6 m.

To allow even better models of the range errors to be employed in a postflight analysis, surface and radiosonde balloon weather measurements were obtained from sites as close to the station as possible from July 26 to August 12, 1969. This information should enable a better determination of the refractivity profile than the current model produces, with a correspondingly better estimate of the zenith range change and a mapping of this range error to other elevation angles.

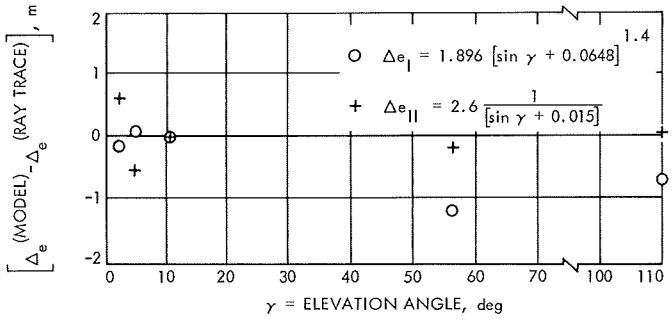

Fig. 2. Comparison of two tropospheric range correction models

NASA — JPL — Coml., L.A., Calif.

N71-16881

TECHNICAL REPORT STANDARD TITLE PAGE

1. Report No. 32-1499	2. Government Accession No.	3. Recipient's Catalog No.
4. Title and Subtitle TRACKING SYSTEM ANALYTIC CALIBRATION ACTIVITIES FOR THE MARINER MARS 1969 MISSION		5. Report Date November 15, 1970 6. Performing Organization Code
7. Author(s) B. D. Mulhall, et al.		8. Performing Organization Report No.
9. Performing Organization Name and Address JET PROPULSION LABORATORY California Institute of Technology 4800 Oak Grove Drive Pasadena, California 91103		10. Work Unit No. 11. Contract or Grant No. NAS 7-100 13. Type of Report and Period Covered Technical Report
12. Sponsoring Agency Name and Address NATIONAL AERONAUTICS AND SPACE ADMINISTRATION Washington, D.C. 20546		14. Sponsoring Agency Code

15. Supplementary Notes

16. Abstract

This report describes the functions of the Tracking System Analytical Calibration activity of the Deep Space Network in support of an entire mission and, in particular, the Mars encounter phase of the Mariner Mars 1969 mission. The support functions encompass calibration of tracking data by estimating physical parameters whose uncertainties represent limitations to navigational accuracy; validation of the calibration data and utilization of these data during a mission; and detailed postflight analysis of tracking data to uncover and resolve any anomalies. Separate articles treat tracking system improvements presently under consideration and error source reductions that may be realizable for future missions; solutions for Deep Space Stations locations; timing errors and polar motion; methods of correcting the tracking data for charged-particle effects (ionospheric corrections); and a model of tropospheric refraction.

17. Key Words (Selected by Author(s))	18. Distribution Statement
Atmospheric Physics Mariner Mars 1969 Project Trajectory Analysis/Orbit Determination Interplanetary Spacecraft Navigation	Unclassified -- Unlimited

19. Security Classif. (of this report)	20. Security Classif. (of this page)	21. No. of Pages	22. Price
Unclassified	Unclassified	70	